## PUBLISHER :

**Address of Publisher**
**& Editor's Office :**

GDAŃSK UNIVERSITY
OF TECHNOLOGY
Faculty
of Ocean Engineering
& Ship Technology

ul. Narutowicza 11/12
80-952 Gdańsk, POLAND
tel.: +48 58 347 13 66
fax : +48 58 341 13 66
e-mail : office.pmr@pg.gda.pl

**Account number :**
**BANK ZACHODNI WBK S.A.**
I Oddział w Gdańsku
41 1090 1098 0000 0000 0901 5569

**Editorial Staff :**
**Tadeusz Borzęcki** Editor in Chief
e-mail : tadbor@pg.gda.pl
**Przemysław Wierzchowski** Scientific Editor
e-mail : e.wierzchowski@chello.pl
**Jan Michalski** Editor for review matters
e-mail : janmi@pg.gda.pl
**Aleksander Kniat** Editor for international relations
e-mail : olek@pg.gda.pl
**Kazimierz Kempa** Technical Editor
e-mail : kkempa@pg.gda.pl
**Piotr Bzura** Managing Editor
e-mail : pbzura@pg.gda.pl
**Cezary Spigarski** Computer Design
e-mail : biuro@oficynamorska.pl

**Domestic price :**
single issue : 20 zł

**Prices for abroad :**
single issue :
- in Europe EURO 15
- overseas US$ 20

**ISSN 1233-2585**


POLISH MARITIME RESEARCH

*in internet*

***www.bg.pg.gda.pl/pmr/pmr.php***


# POLISH MARITIME RESEARCH

No 3(75) 2012 Vol 19


## CONTENTS

# Editorial

POLISH MARITIME RESEARCH is a scientific journal of worldwide circulation. The journal appears as a quarterly four times a year. The first issue of it was published in September 1994. Its main aim is to present original, innovative scientific ideas and Research & Development achievements in the field of :

**Engineering**, **Computing & Technology**, **Mechanical Engineering**,

which could find applications in the broad domain of maritime economy. Hence there are published papers which concern methods of the designing, manufacturing and operating processes of such technical objects and devices as : ships, port equipment, ocean engineering units, underwater vehicles and equipment as well as harbour facilities, with accounting for marine environment protection.
The Editors of POLISH MARITIME RESEARCH make also efforts to present problems dealing with education of engineers and scientific and teaching personnel. As a rule, the basic papers are supplemented by information on conferences , important scientific events as well as cooperation in carrying out international scientific research projects.

# Scientific Board

**POLISH MARITIME RESEARCH** 3(75) 2012 Vol 19; pp. 3-15
10.2478/v10012-012-0026-2

# Numerical prediction of steady and unsteady tip vortex cavitation on hydrofoils

**Paweł Flaszyński**, Ph.D.
**Jan A. Szantyr**, Prof.
**Krzysztof Tesch**, Ph.D.
Gdansk University of Technology, Poland

ABSTRACT

*The article presents the numerical method for prediction of tip vortex cavitation generated on hydrofoils. This method has been developed in the course of numerical and experimental research described in earlier publications. The objective of the research was to design the optimum discrete grid structure for this specific computational task and to select the best turbulence model for such an application The article includes a short description of the method and a computational example demonstrating its performance. In this example the results of numerical prediction of the cavitating tip vortex obtained from two commercial CFD codes are compared with experimental photographs taken in the cavitation tunnel in the corresponding flow conditions. Altogether nine different flow conditions are tested and analyzed, but only selected results are included. The accuracy of the numerical predictions is discussed and the reasons for minor existing discrepancies are identified. The unsteady tip vortex calculations are also presented, showing the fluctuations of the transverse velocity components predicted for three cross-sections of the cavitating vortex kernel.*

**Key words:** rotary hydraulic machinery; vortex cavitation; numerical methods

## INTRODUCTION

The computational method used in this article has been developed in the course of detailed experimental and numerical research described in [2, 3, 4]. This research was at first devoted to numerical prediction of the tip vortices generated behind the tips of hydrofoils without cavitation. At that stage the objective was to reproduce as accurately as possible the complicated velocity field generated by the non-cavitating tip vortices. This velocity field is dominated by the strong secondary flow induced by the vortex and depending on its intensity. The intensity of the tip vortex results from the hydrodynamic loading of the hydrofoil and on the complicated processes of vorticity concentration and dissipation. The results of own LDV measurements of the velocity field in the vicinity of tip vortices behind hydrofoils were used as the reference for the computations. As the result the computational grid structures and turbulence models best suited for prediction of flows dominated by the concentrated vorticity were selected. In the next stage the research was focused on prediction of the detailed geometry of the cavitating tip vortices. In this stage two commercial codes were used in parallel, namely Ansys/Fluent and Ansys/CFX. Analogically to the previous stage, different grid structures and different turbulence models were tested. The PIV measurements of the velocity field around the cavitating tip vortex kernel were used as a support of the numerical calculations. The final recommendations included the optimum grid structure for the specific task of predicting tip vortex cavitation and the turbulence model best suited for this task – k-ε RNG. These recommendations constitute in fact the method for numerical prediction of tip vortex cavitation.

This method is now tested in confrontation with the experimental observations of the tip vortex cavitation behind the hydrofoil. The photograph of the hydrofoil model installed in the measuring section of the cavitation tunnel is shown in Fig. 1, together with the corresponding sketch of the computational domain used in numerical calculations.

Altogether nine different flow conditions were tested. They resulted from combination of three mean flow velocity values of 5.9, 5.2 and 4.3 [m/s] and three angles of attack of 4, 8 and 12 degrees. For the lowest angle of attack only at the highest flow velocity some cavitation phenomena were observed, consequently only seven conditions are presented in detail in the following parts of the article.

## NUMERICAL MODEL DESCRIPTION – ANSYS/ FLUENT

Calculations by Ansys/Fluent were performed using the unstructured grid constructed of hexahedral elements, generated using Hexpress Numeca. This grid consists of ~4.7 million

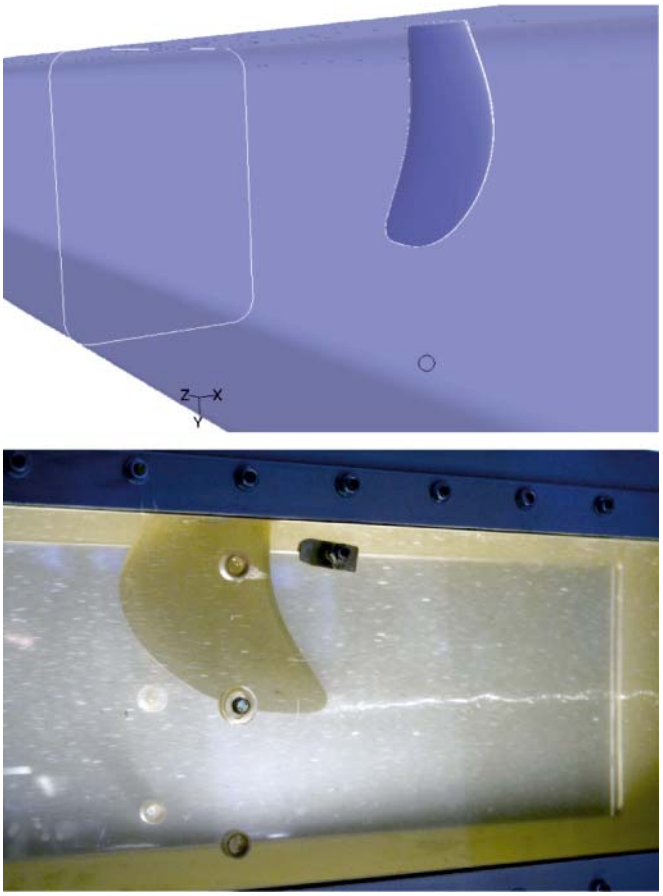

*Fig. 1. Scheme of the computational domain and photograph of the hydrofoil in the cavitation tunnel*

*Fig. 2. Computational grid used in Fluent in the tip region of the hydrofoil*

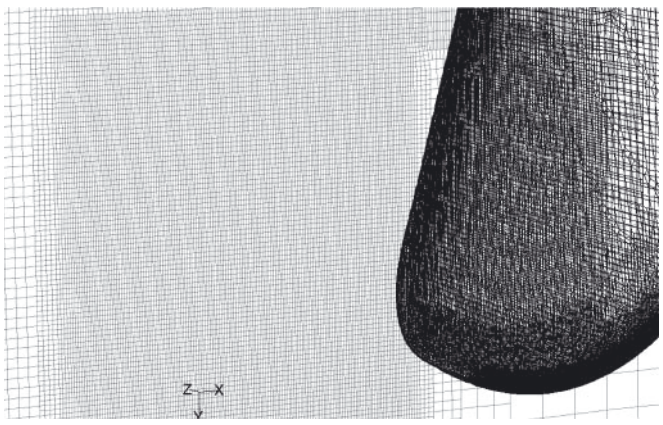

*Fig. 3. Computational grid used in Fluent behind the tip region of the hydrofoil*

cells and it is refined close to the wall, so the condition $y^+ \sim 1$ is fulfilled. The details of the grid in the most important tip region of the hydrofoil are shown in Figs 2 and 3.

It may be seen that the density of the grid is markedly increased near the leading edge of the hydrofoil and in the region behind the hydrofoil tip, i.e. in the areas playing an important role in the formation of the tip vortex. The computations were performed using the Ansys/Fluent V12 and employing the MUSCL (Monotone Upstream-Centered Scheme for Conservation Laws) scheme for convection terms in the transport equations. The k-ε RNG turbulence model was used, described by the following equations:

$$\frac{\partial}{\partial t}(\rho k)+\frac{\partial}{\partial x_i}(\rho k u_i)= \tag{1}$$
$$=\frac{\partial}{\partial x_j}\left(\alpha_k \mu_{eff}\frac{\partial k}{\partial x_j}\right)+G_k+G_b-\rho\varepsilon-Y_v+S_k$$

$$\frac{\partial}{\partial t}(\rho\varepsilon)+\frac{\partial}{\partial x_i}(\rho\varepsilon u_i)=\frac{\partial}{\partial x_j}\left(\alpha_\varepsilon \mu_{eff}\frac{\partial \varepsilon}{\partial x_j}\right) \tag{2}$$
$$+C_{1\varepsilon}\frac{\varepsilon}{k}(G_k+C_{3\varepsilon}G_b)-C_{2\varepsilon}\rho\frac{\varepsilon^2}{k}-R_\varepsilon+S_\varepsilon$$

Detailed description of the turbulence model and model constants employed in Equations (1) and (2) may be found in [1, 6]. The calculations were performed for a two-phase flow using the mixture model. Cavitation was modeled using the Rayleigh-Plesset equation in Zwart-Gerber-Belamri formulation [7]. The gaseous phase was treated as a compressible medium using the perfect gas equation.

The boundary conditions were set as follows:

**Inlet**:
- Mass flow according to the mean velocity (4.3, 5.2 or 5.9 [m/s])
- Absolute temperature 283 [K]
- Degree of turbulence 1%
- Ratio of turbulent viscosity to laminar viscosity 10

**Outlet**:
- Static pressure 15 [kPa] (this corresponds to total pressure in the cavitation tunnel measuring section approximately 30 [kPa])

## NUMERICAL MODEL DESCRIPTION – ANSYS/ CFX

Calculations by Ansys/CFX were performed using the unstructured grid which consisted of approximately 9 million elements, including about 8.2 million tetrahedral elements and 0.8 million prismatic elements in the boundary layer. The grid was generated using CFX Mesh. The calculations were performed using Ansys/CFX 12, making use of HRS (High Resolution Scheme) for the convection terms of the transport equations. The details of the grid in the tip region of the hydrofoil are shown in Figs. 4 and 5, with increased density in the regions of expected cavitation.

The calculations by Ansys/CFX were performed for the same flow parameters and boundary conditions as by Ansys/ Fluent. In the case of CFX the gaseous phase was treated as incompressible.

*Fig. 4. Computational used in CFX in the tip region of the hydrofoil*

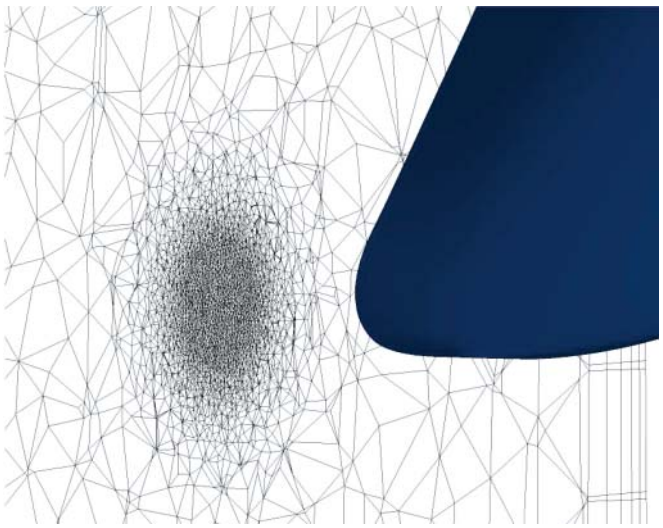

*Fig. 5. Computational grid used in CFX behind the tip region of the hydrofoil*

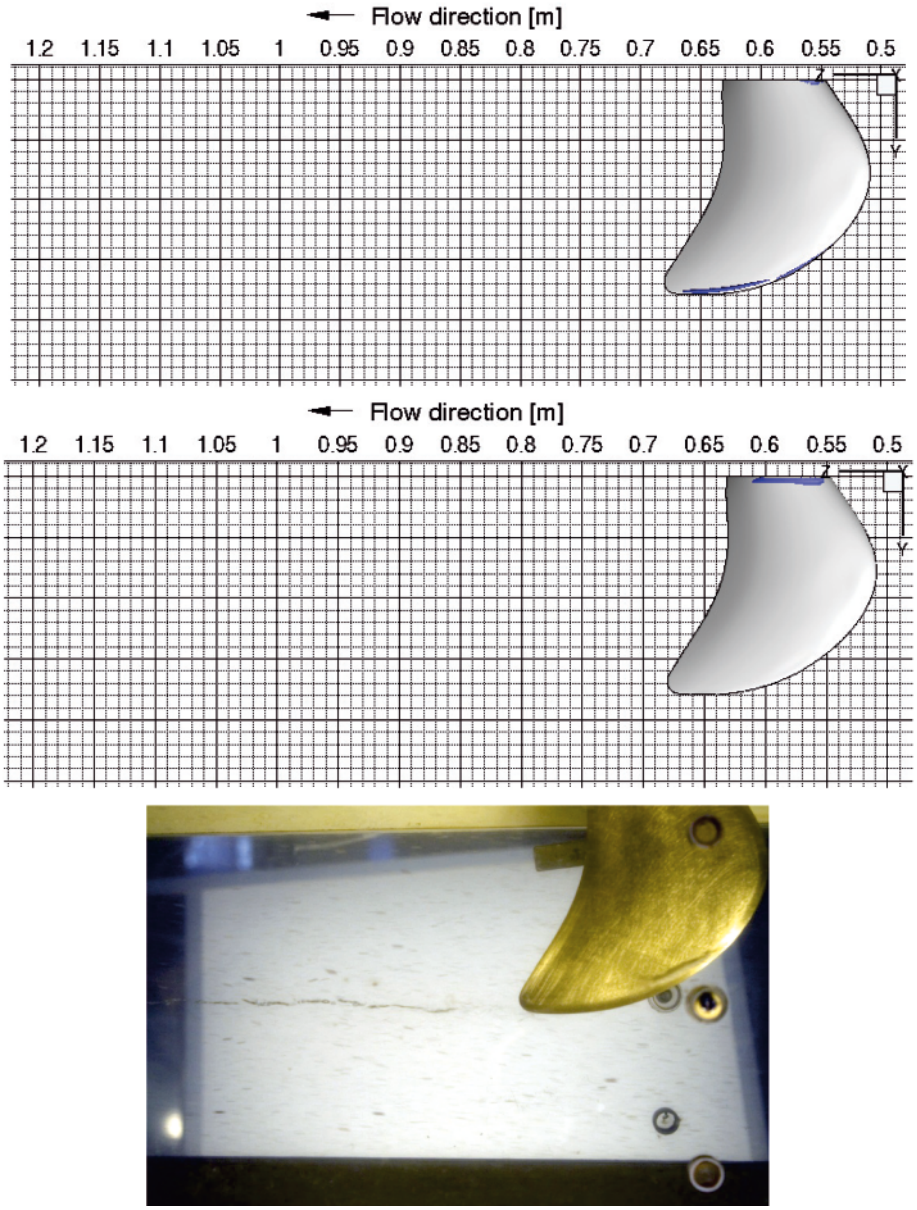


*Fig. 6. Comparison of calculations by Fluent (top), CFX (middle) and experimental photograph (bottom) for angle of attack 4 [deg] and mean flow velocity of 5.9 [m/s]*

## COMPARISON OF NUMERICAL AND EXPERIMENTAL RESULTS

In this section the comparison of numerical and experimental results is shown in Figs. 6 – 12 for seven flow conditions, for which cavitation phenomena were observed. In each Figure the results from Fluent and CFX calculations are shown together with the photograph taken in the cavitation tunnel in the corresponding flow condition.

In Fig. 6 the prediction by Fluent of small region of cavitation area at the tip of the hydrofoil agrees reasonably well with experiment, while both CFX and Fluent do not detect the weak and detached cavitating tip vortex visible in the photograph. Calculation by CFX does not detect any cavitation in tip region of the hydrofoil. A minor root cavitation predicted by both programs is not confirmed by experiment. The reason of such difference is probably a small gap between the hydrofoil and the tunnel upper wall, which influences the flow structure locally. This root gap is not taken into account in the numerical model.

In Fig 7 the calculation by Fluent agrees quite well with the experiment, both the small region of cavitation on the hydrofoil and the presence of the tip vortex are correctly predicted. However, the length of the cavitating tip vortex is seriously underestimated. The calculation by CFX underpredicts both hydrofoil and tip vortex cavitation. The small region of root cavitation indicated by CFX is again not confirmed by experiment.

In Fig. 8, both numerical simulations predict quite long cavitating tip vortices, but they are still shorter than the one observed experimentally. The diameter of the cavitating tip vortex kernel close to the hydrofoil tip is quite well calculated. The prediction of the vortex by CFX is a little further from the experimental one than the prediction by Fluent. On the other hand, the prediction of hydrofoil cavitation by CFX seems to be closer to the observed experimentally, than it is predicted by Fluent. Both programs again calculate small regions of root cavitation, which are not confirmed by experiment.

In Fig. 9 both programs produce practically equivalent predictions, which are quite close to the experimental

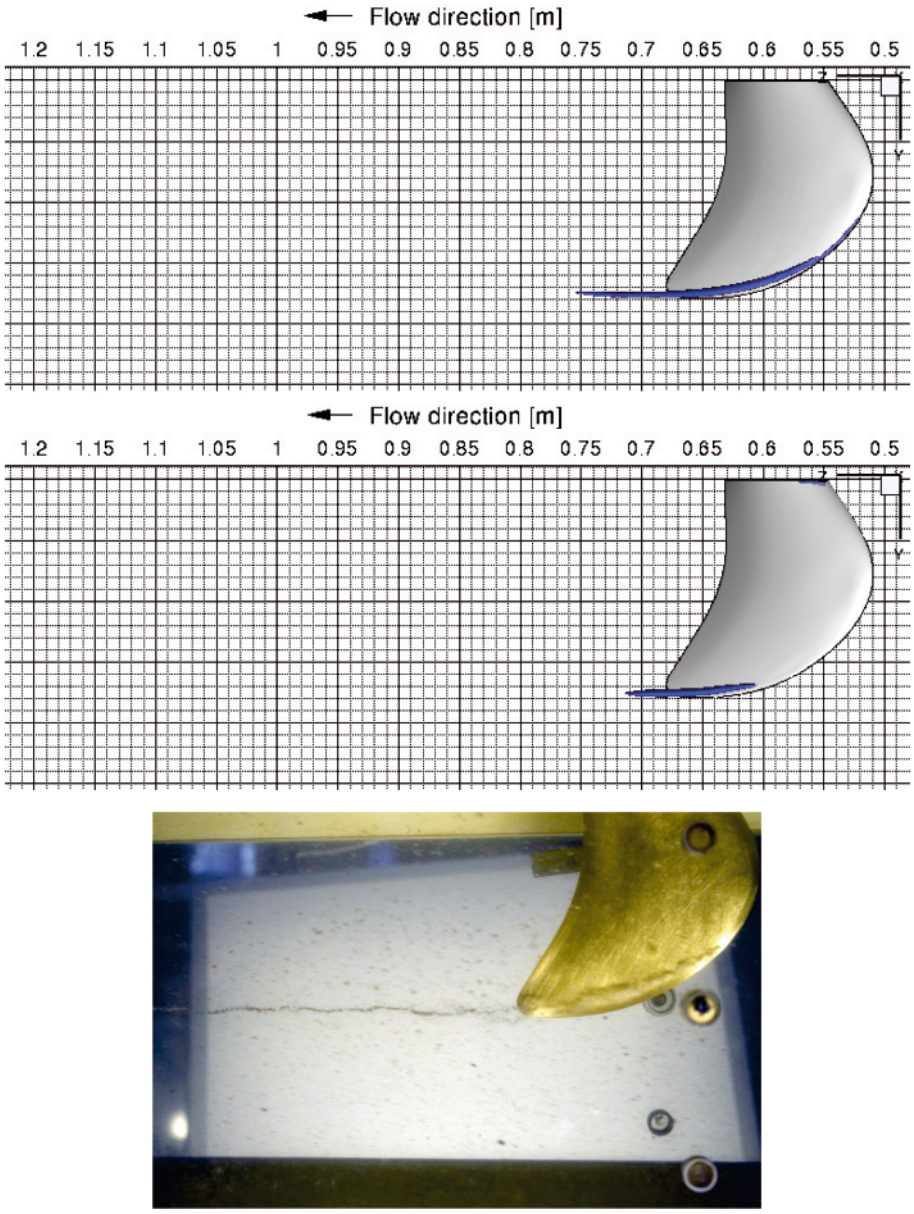


***Fig. 7.*** *Comparison of calculations by Fluent (top), CFX (middle) and experimental photograph (bottom) for angle of attack 8 [deg] and mean flow velocity of 4.3 [m/s]*

observation, both in terms of hydrofoil and tip vortex cavitation. Similarly as before the length of the cavitating tip vortex is underpredicted in calculations. The diameter of the cavitating vortex kernel near the hydrofoil tip is quite well calculated. The abrupt termination of the cavitating vortex kernel as calculated by Fluent looks unnatural. This unnatural vortex termination is due to the ending of the increased density region of the computational grid. In case of Fluent, in order to obtain the converged solution within defined convergence criteria, the tuning of under-relaxation factors was required. The reason for this is the flow separation on the suction side of the hydrofoil and instability caused by the obtained flow structure. The problem is discussed further in the paper.

As previously, the both programs indicate root cavitation, which cannot be seen in the photograph.

At the highest angle of attack (12 deg), differences between CFD results and experimental visualization are the most significant. In Fig. 10, the length of the cavitating tip vortex by both solvers is seriously underpredicted, while its thickness in the region close to the hydrofoil tip is calculated correctly. The abrupt terminations of a thick cavitating vortex in CFX as well as in Fluent look unnatural. This is again caused by the ending of the increased density zone of the computational grid and could be easily corrected if necessary. The radial extent of cavitation on the hydrofoil (along the leading eadge) is reasonable well predicted by both programs. In both cases, the chordwise extent of the cavitation zone is underpredicted.

At the higher velocity (5.2 m/s) and angle of attack equal to 12 deg, the cavitation on the hydrofoil and within the tip vortex is highly overestimated. The radial extent of cavitation on the hydrofoil is well predicted by both programs, but this time they both overestimate the chordwise extent of cavitation. On the other hand, the photographed cavitating tip vortex seems to be visibly thinner than the prediction by both programs. Comparing experimental visualization done for the main flow velocity 4.3 m/s (Fig. 10) and 5.2 m/s (Fig. 11), one can notice that in the second case cavitating vortex seems to be thinner, but less concentrated that at the lower velocity. It arises from the unsteady behaviour of the flow and cavitation conditions

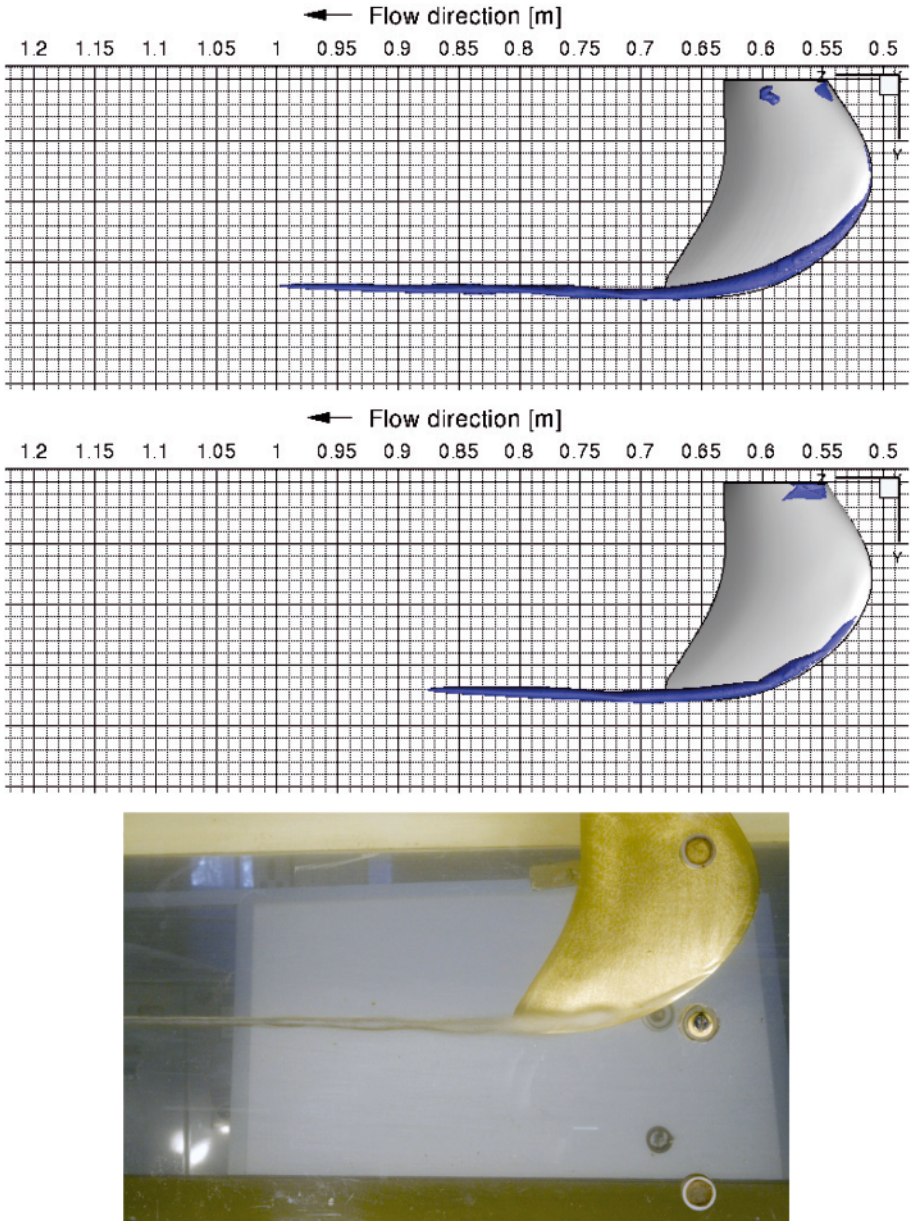


***Fig. 8.*** *Comparison of calculations by Fluent (top), CFX (middle) and experimental photograph (bottom) for angle of attack 8 [deg] and mean flow velocity of 5.2 [m/s]*

high sensitivity and dependence on the local flow structure and water aeration.

The results for the maximum investigated hydrofoil loading (angle of attack 12 [deg], flow velocity 5.9 [m/s]) are not presented, because of lack of Fluent solver convergence caused by the unsteady flow separation on the suction side.

## CALCULATIONS OF UNSTEADY TIP VORTEX CAVITATION

It is a well-known fact that cavitation phenomena are inherently unstable. This is particularly true for tip vortex cavitation. Although it was not possible to register the unsteady phenomena in the experiments, an unsteady CFD calculations using Fluent and CFX have been performed in order to compare the steady and unsteady results. The simulations have been performed using the previously selected k - ε RNG turbulence model for the case of inflow velocity 5.2 [m/s] and angle of attack of 12 degrees. In case of both solvers the second order time accurate scheme was applied. The presented below results are obtained for time step 0.01s.

The flow structure based on the time averaged flow field is shown in Fig. 12. The region of calculated flow separation near the root of the hydrofoil and the streamlines starting near the leading edge creating the tip vortex can be observed. Downstream of the hydrofoil, the velocity magnitude at the cross-section is presented. One can notice the increase of the flow velocity close to the tip vortex due to the secondary flow and the decrease of the velocity in the vortex core, as a consequence of the dissipation effects. The lower velocity areas are also shown in the wake and downstream of the suction side separation near the upper wall. The existence of separation is the reason of the convergence problem at the higher hydrofoil loading in Fluent simulations. The effect is weaker in CFX case, because the mesh is much coarser in the area far from the tip vortex, so the vortex structure downstream of the separation dissipates quickly and does not influence on the unsteady behaviour in this flow area.

Anyway, it is interesting that in spite of the lack of the unsteady effect of the separated flow, CFX results indicate higher unsteadiness in the vortex area than it was obtained by

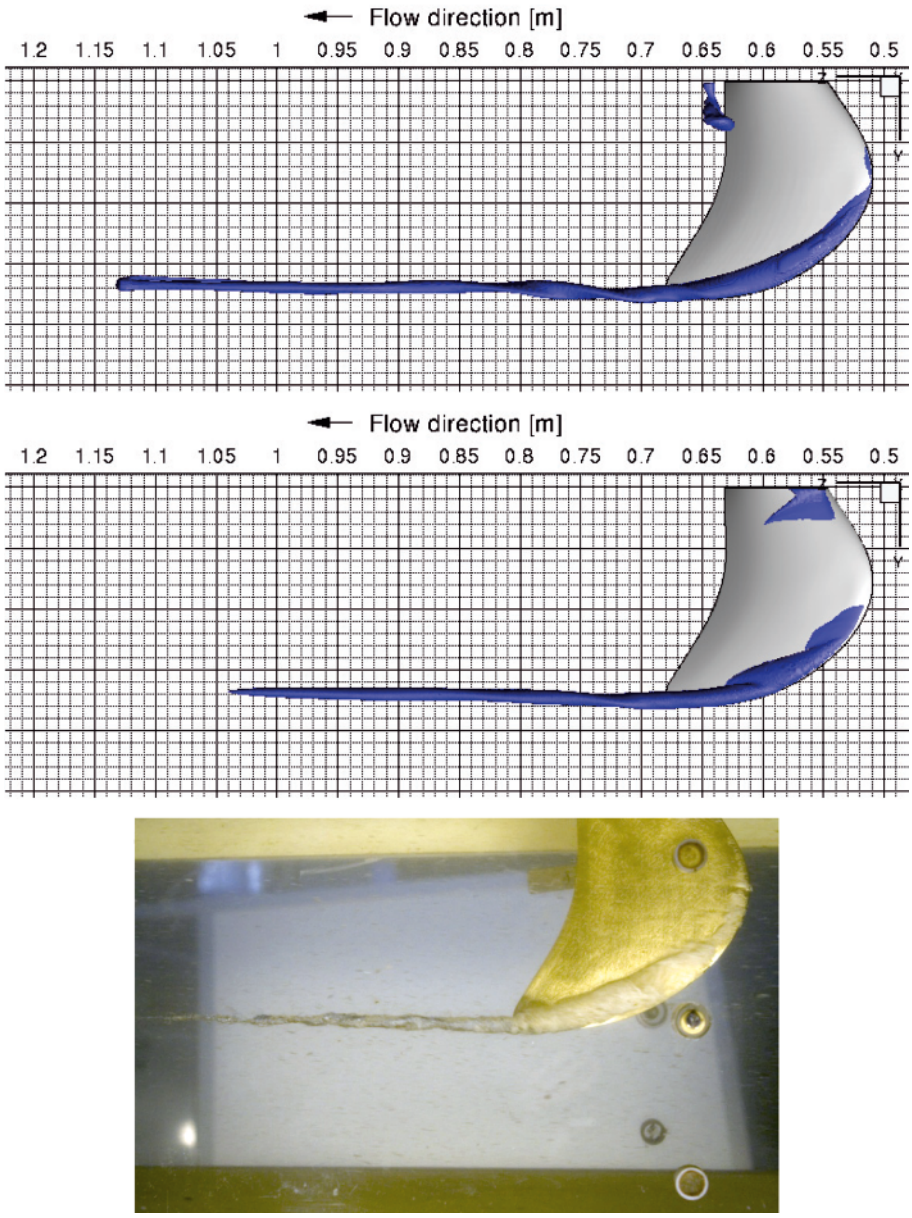


***Fig. 9.*** *Comparison of calculations by Fluent (top), CFX (middle) and experimental photograph (bottom) for angle of attack 8 [deg] and mean flow velocity of 5.9 [m/s]*

Fluent. The fluctuations of the velocity X and Y components at the sections 50 mm, 200 mm and 300 mm downstream of the hydrofoil are shown in Figs. 13 and 14. Both velocity components are located in the secondary flow plane, so they indicate of the fluctuations in the tip vortex area. One can notice, that fluctuations obtained with Fluent simulations are an order of magnitude lower than in CFX case. The simulation time in CFX was 2 seconds and the fluctuations of the tip vortex with 5 Hz frequency are noticed. Fluent simulations were done for much longer time ~20 seconds and no high frequency fluctuations are obtained in the vortex area. The unsteady effects are obtained close to the hydrofoil root only.

In Figs. 13 and 14, the black line marks the area of the time averaged cavitating zone, i.e. the existence of the gaseous phase. In case of Fluent, the flow parameters distribution at the section (50 mm) close to the hydrofoil show the highly three dimensional shape of the cavitating vortex, far from the regular cylindrical shape. Further downstream from the hydrofoil it becomes "more" cylindrical. In case of CFX, such an effect is much weaker.

The next difference is the maximum fluctuations location within the cavitating zone. In the Fluent case, the highest values are spread along the surface dividing the two phases. CFX results indicate the maximum fluctuations at the vortex centre. The experimental assessment of the numerical results accuracy can be done only by the high resolution flow velocity measurements within the range of cavitating vortex. Such measurements were not possible in the research project.

The gaseous phase fluctuations are shown in Fig. 15. As regards the fluctuations distribution, the results are similar. The maximum values are close to the time averaged inter phase border surface in case of both solvers, but CFX values are 7 times higher than obtained in Fluent.

The time averaged secondary flow velocity is shown in Fig. 16. The velocity in plane normal to the main flow indicates the vortex intensity at the consecutive sections downstream of the hydrofoil. It shown that in the gaseous phase zone (or in fact two-phase zone) the velocity is rising from the vortex centre to the location where the gaseous phase disappears, then the velocity decreases in the water

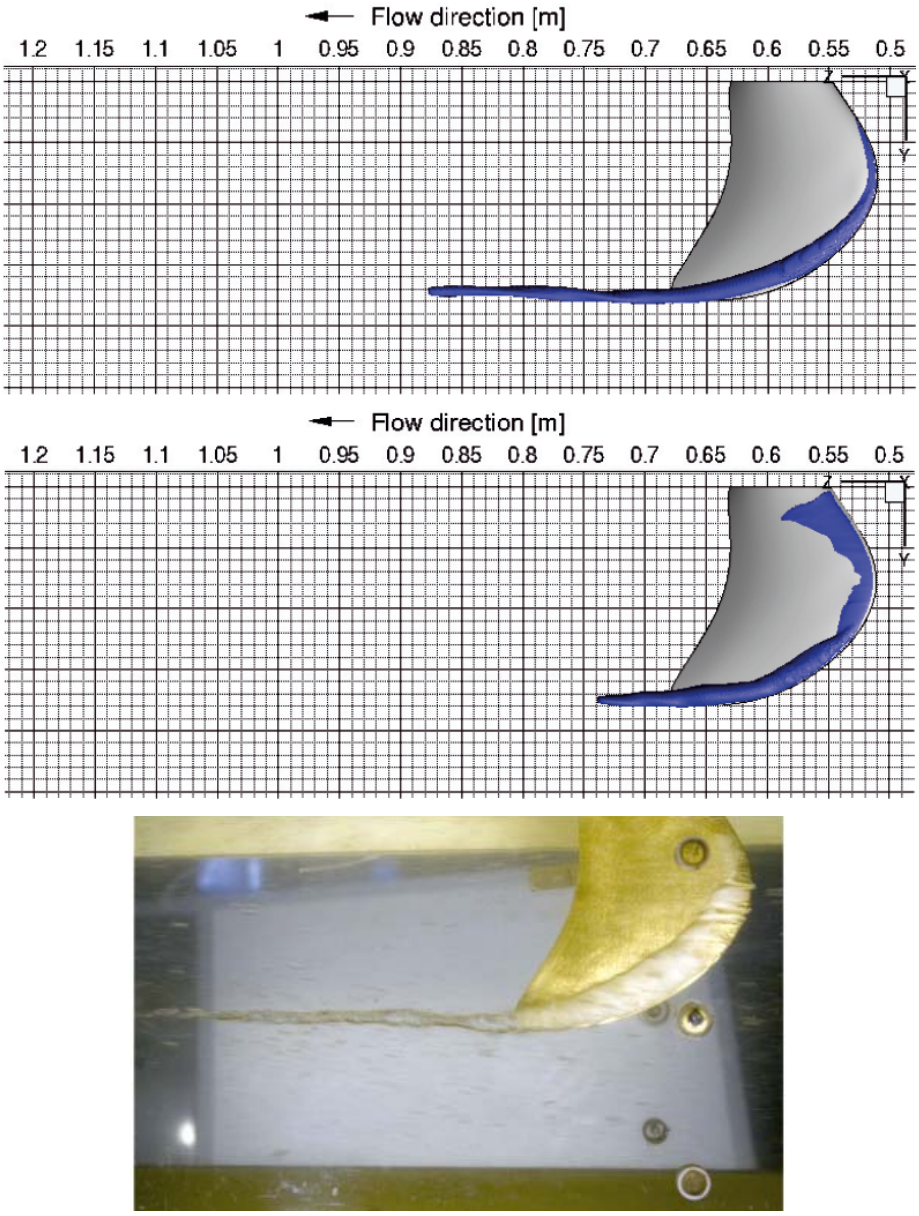


***Fig. 10.*** *Comparison of calculations by Fluent (top), CFX (middle) and experimental photograph (bottom) for angle of attack 12 [deg] and mean flow velocity of 4.3 [m/s]*

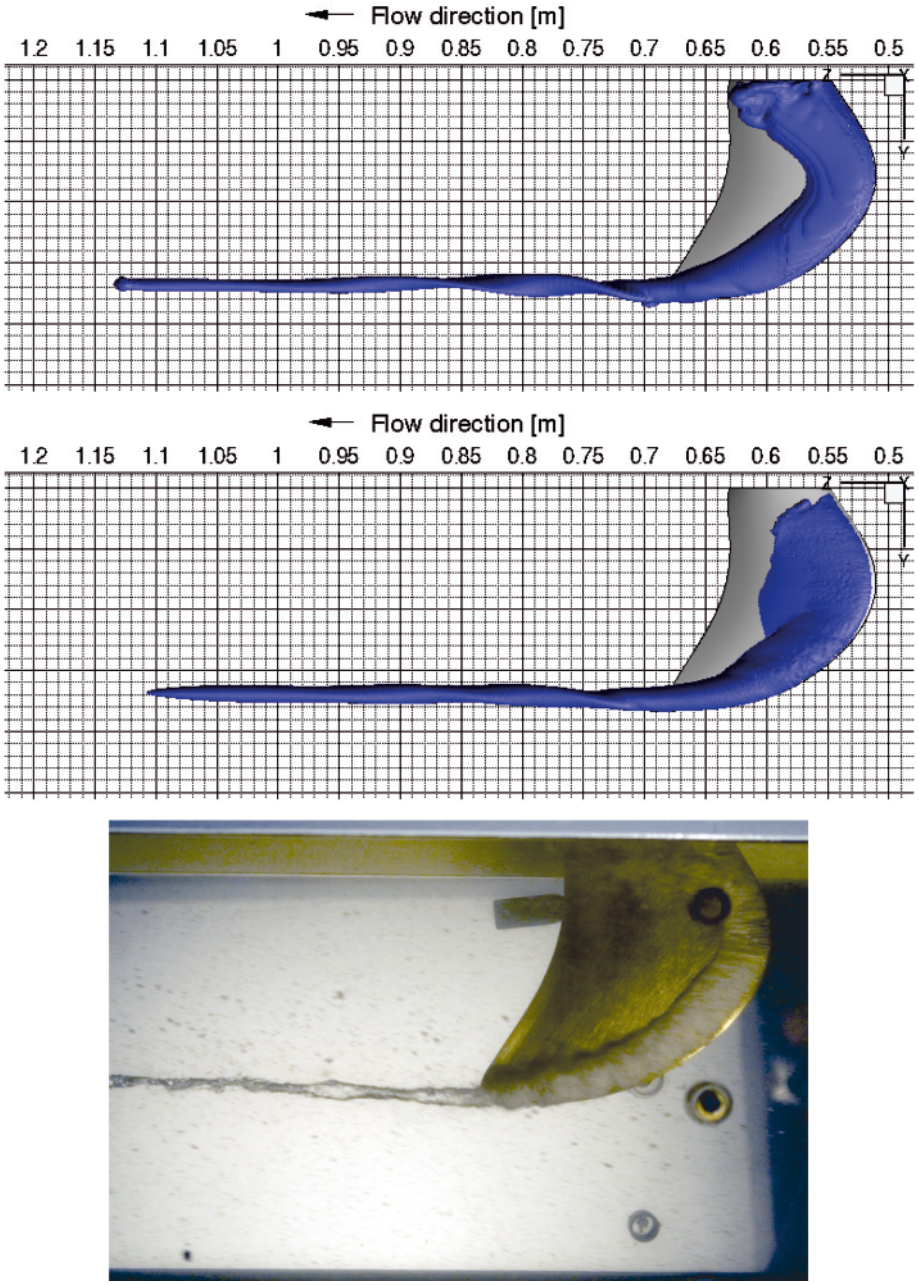


***Fig. 11.*** *Comparison of calculations by Fluent (top), CFX (middle) and experimental photograph (bottom) for angle of attack 12 [deg] and flow velocity of 5.2 [m/s]*

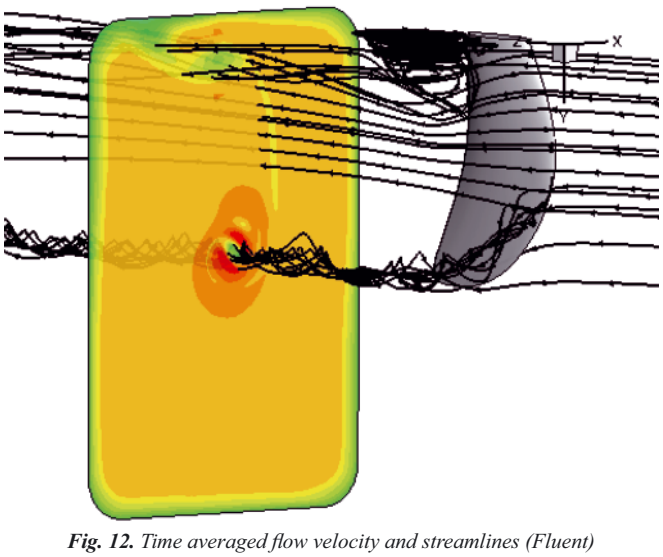

***Fig. 12.*** *Time averaged flow velocity and streamlines (Fluent)*

area. The maximum values obtained in Fluent are higher than in CFX. It means that the vortex intensity predicted by Fluent is higher, what is reflected by the cavitating zone extension. In Fig. 17, the iso-surface of gaseous phase for time averaged results is shown. It can be compared with Fig. 11, where the steady results are presented. In case of CFX, the steady and unsteady results are similar. The unsteady simulations results indicate a bit lower range of cavitation on the hydrofoil and longer cavitating zone in the tip vortex. In case of Fluent results, the difference is much higher. In spite of low fluctuations in the tip vortex area, one can see much smaller extension of the cavitating zone on the hydrofoil. It is now much more closer to the experimental visualization than it was obtained by steady simulations. The higher secondary flow intensity influences the longer tip vortex and the length of cavitation zone. One has to emphasize that three dimensional structure of the vortex and its skewness is also much higher than in steady simulations and both (steady and unsteady) CFX results.

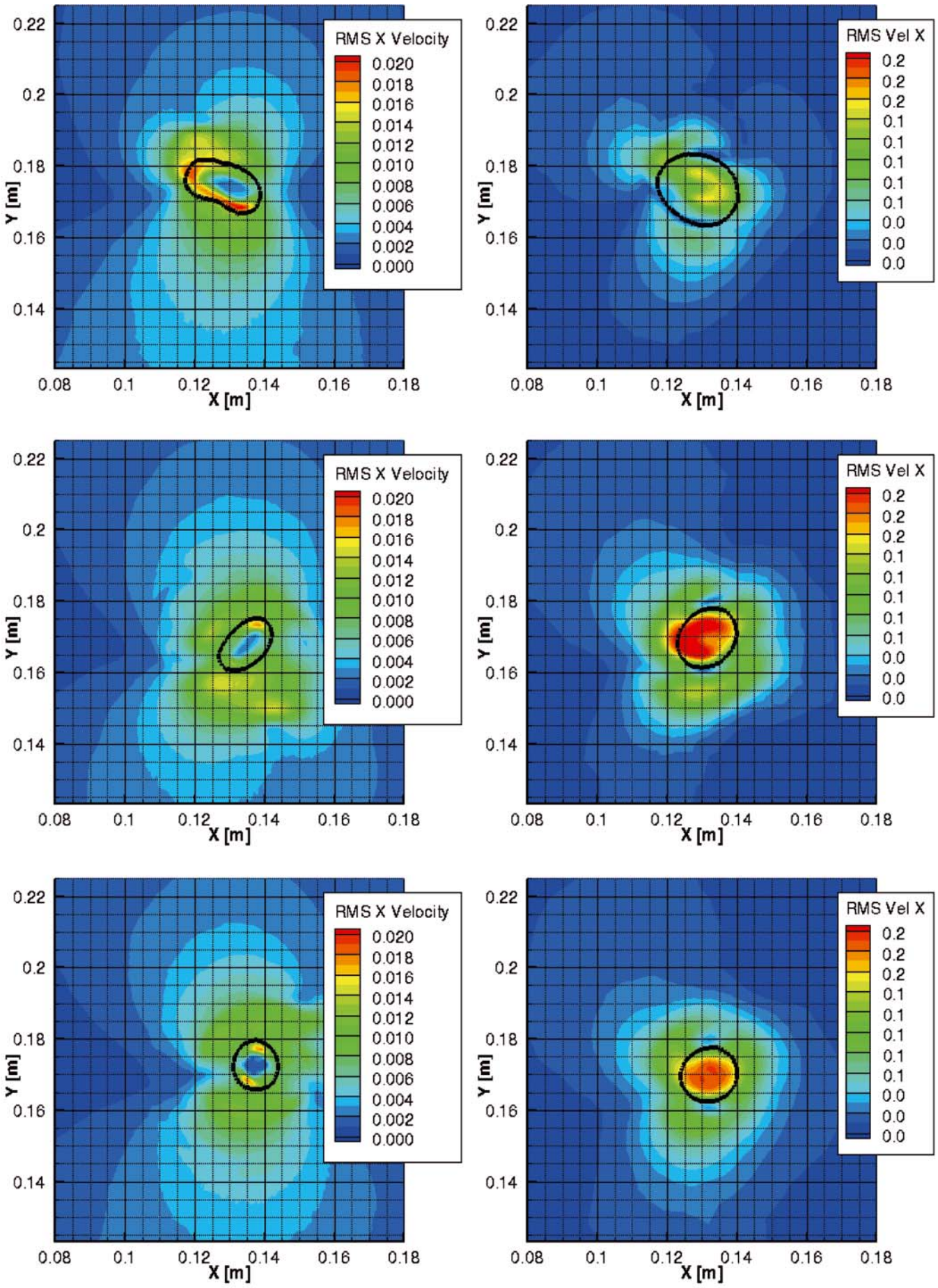


***Fig. 13.*** *The time-dependent fluctuations of the X velocity component (Fluent – left, CFX -right) at the cross-sections (from top) 50 mm, 200 mm and 300 mm behind the hydrofoil (black line indicates the time averaged cavitating zone)*

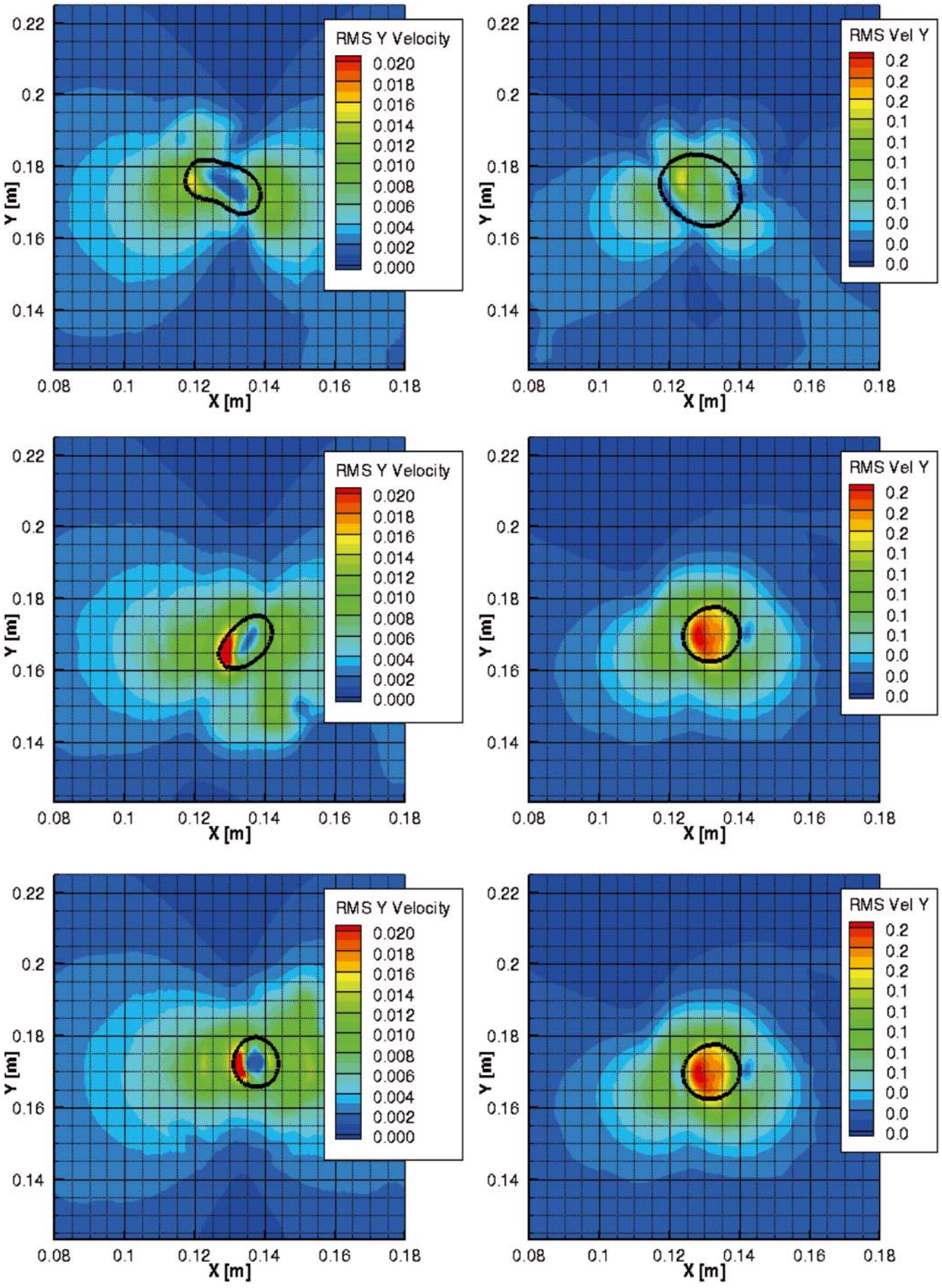


*Fig. 14. The time-dependent fluctuations of the Y velocity component (Fluent – left, CFX -right) at the cross-sections (from top) 50 mm, 200 mm and 300 mm behind the hydrofoil (black line indicates the time averaged cavitating zone)*

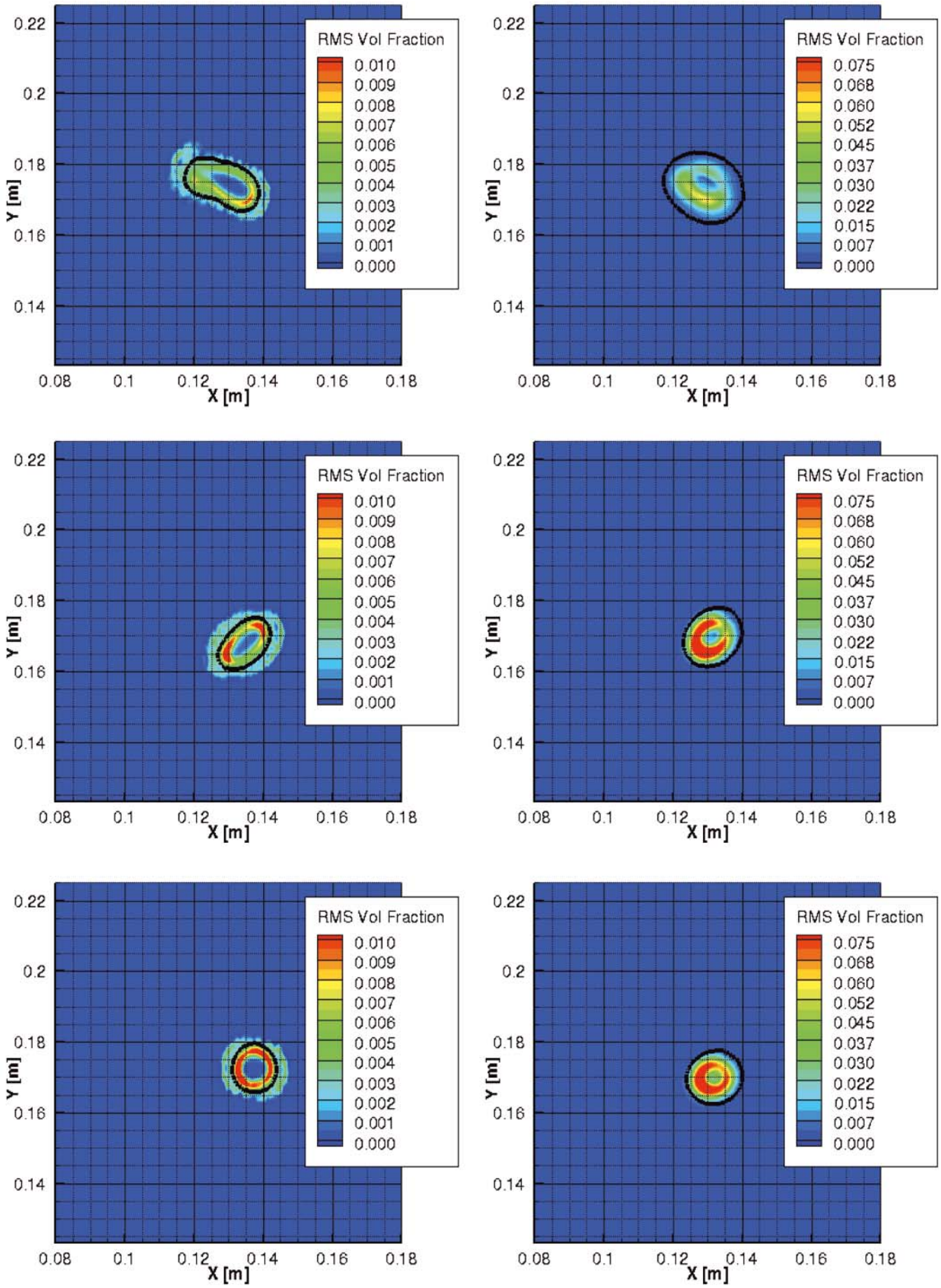


***Fig. 15.*** *The time-dependent fluctuations of the gaseous phase (Fluent – left, CFX -right) at the cross-sections (from top) 50 mm, 200 mm and 300 mm behind the hydrofoil (black line indicates the time averaged cavitating zone)*

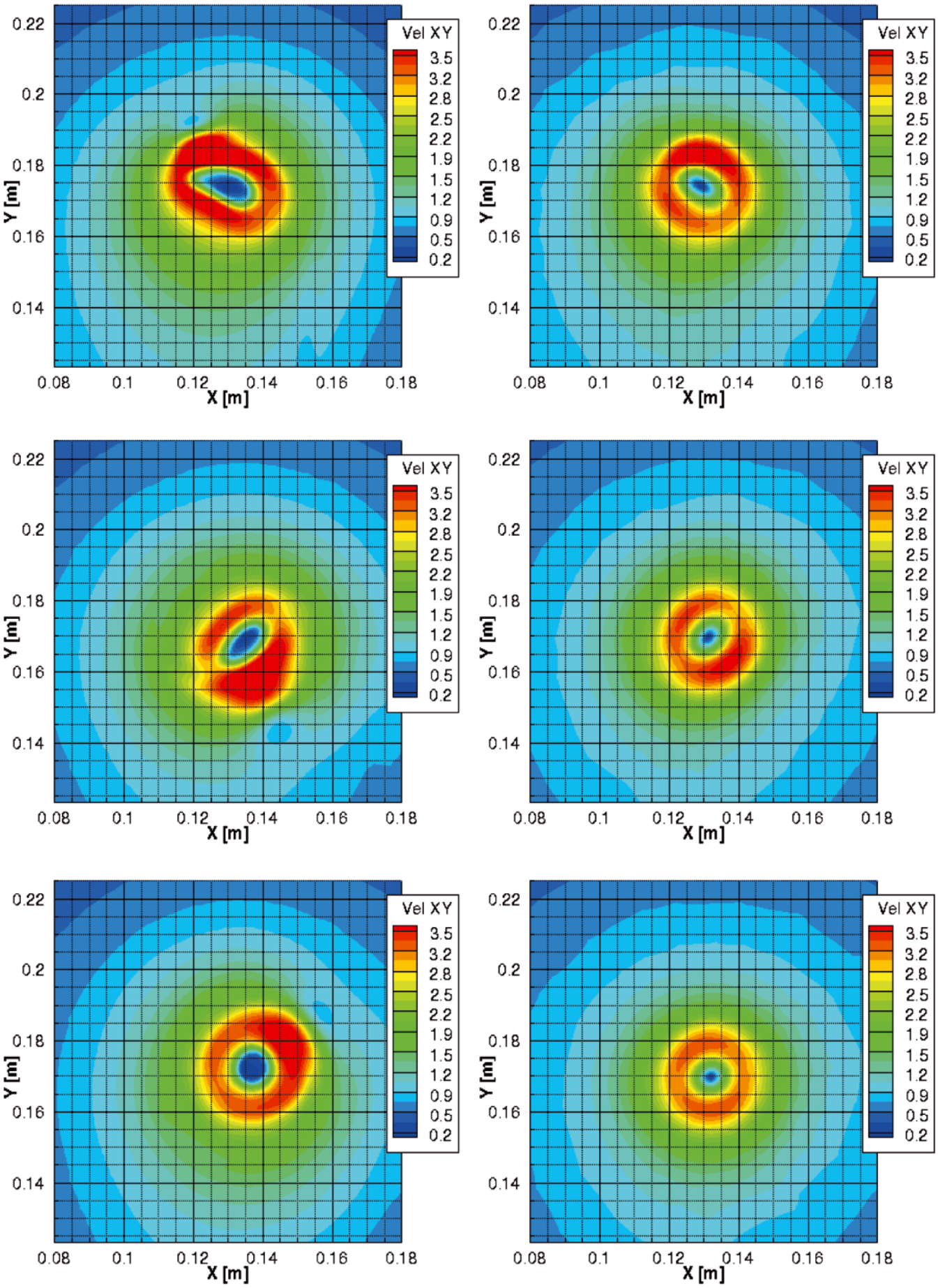


*Fig. 16. The time-averaged velocity of flow in the X-Y plane as calculated by Fluent (left) and CFX (right) in the cross-sections (from top) 50 mm, 200 mm and 300 mm behind the hydrofoil*

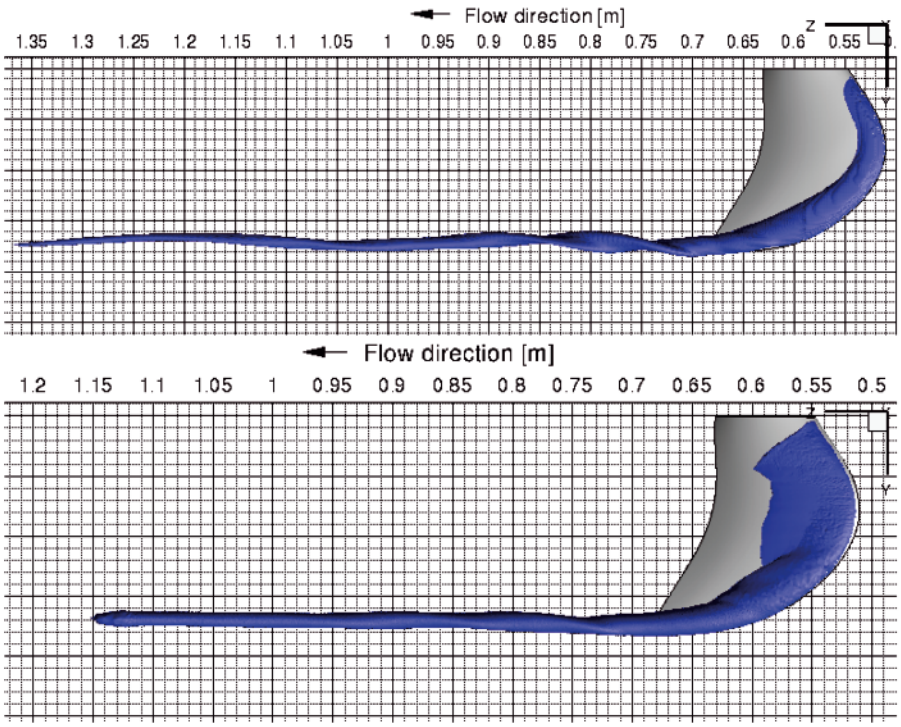


***Fig. 17.*** *Gaseous phase iso-surface (time-averaged) - Fluent (top), CFX (bottom) - angle of attack 12 [deg] and flow velocity of 5.2 [m/s]*

## CONCLUSIONS

- The numerical investigations of the cavitating tip vortex generated on the hydrofoil are presented. It is demonstrated that both solvers CFX and Fluent predict the tip vortex and the cavitating zone qualitatively well. In both cases, the trend of dependence of cavitation extent and intensity on the inflow conditions was reflected properly. At high inflow velocity and high angle of attack the separation on the suction side of the hydrofoil was obtained, which is the reason of the instability and the lack of converged solution in Fluent case. The reason of the higher sensitivity to the flow structure dependence in Fluent case is the mesh resolution in the wake along the whole span. In CFX case, the mesh is refined close to the wall and in the tip vortex area, only.
- The simulations for higher loading (high inflow velocity and angle of attack) indicate necessity of the unsteady effects to be taken into account if the highly three dimensional effects are detected in steady simulations. It leads to better agreement with the experimental visualization.
- Since cavitation is highly sensitive and dependent on the local flow structure and water aeration, the quantitative comparison requires detailed information of the fluid quality in order to set an adequate boundary conditions for two phase flow.
- It is difficult to assess the flow velocity distribution in the vortex as well as velocity fluctuations and gas volume fraction, until the high resolution in space and time flow field measurements are not performed.

### *Acknowledgement*

The research described in this article has been conducted with the support of the Research Grant No. N N504 088738 of the Polish National Centre for Research and Development (NCBR).

### BIBLIOGRAPHY

1. Ansys/Fluent Release 12.0 Users Manual, 2009
2. Flaszyński P., Szantyr J., Dymarski P., Kraskowski M.: *Numerical Prediction of Vortex Generated by Hydrofoil,* Proc. Intern. Symposium on Marine Propellers, Trondheim, Norway, June 22-24, 2009
3. Flaszyński P., Szantyr J., Biernacki R., Dymarski P., Kraskowski M.: *A Method for the Accurate Numerical Prediction of the Tip Vortices Shed from Hydrofoils*, Polish Maritime Research No. 2(65), Vol. 17, 2010, pp. 10-17
4. Szantyr J.A., Flaszyński P.,Tesch K., Suchecki W., Alabrudziński S.: *An Experimental and Numerical Study of Tip Vortex Cavitation*, Polish Maritime Research No. 4(71), Vol. 18, 2011, pp. 14-22
5. Szantyr J.A., Biernacki R., Flaszyński P., Dymarski P., Kraskowski M.: *An Experimental and Numerical Study of the Vortices Generated by Hydrofoils*, Polish Maritime Research No. 3(61), Vol. 16, 2009, pp. 11-17]
6. Yakhot V., Orszag S.A., Renormalization Group of Turbulence: I. Basic Theory, Journal of Scientific Computing, 1(1):1-51, 1986
7. Zwart P.J., Gerber A.G., Belamri T., *A Two-Phase Flow Model for Predicting Cavitation Dynamics,* Fifth International Conference on Multiphase Flow, Yokohama, Japan, 2004

### CONTACT WITH THE AUTHORS

Jan A. Szantyr, Prof., e-mail: jas@pg.gda.pl
Paweł Flaszyński, Ph.D., e-mail: pflaszyn@pg.gda.pl
Krzysztof Tesch, Ph.D., e-mail: krzyte@pg.gda.pl

Faculty of Mechanical Engineering
Gdansk University of Technology
Narutowicza 11/12
80-233 Gdansk, POLAND

**POLISH MARITIME RESEARCH** 3(75) 2012 Vol 19; pp. 16-25
10.2478/v10012-012-0027-1

# Research on a method of hull form design based on wave-making resistance optimization

**Jianglong Sun**[a], Ph.D., Assoc. Prof.
**Xujian Lv**[a], Ph.D.
**Weibin Liu**[a], Ph.D., Assoc. Prof.
**Hanwen Ning**[b], Ph.D.
**Xianwen Chen**[a], Master Graduate Student
[a] Huazhong University of Science & Technology, Wuhan, P.R. China
[b] Zhongnan University of Economics and Law, Wuhan, P.R. China

ABSTRACT

*In this paper, we consider an optimization of the hull shape in order to minimize the total resistance of a ship. The total resistance is assumed to be the sum of the wave resistance computed on the basis of the thin-ship theory and the frictional resistance. Smoothness of hull lines is proved with mathematical procedure, in which differentials of the hull lines functions are analyzed. The wave-making resistance optimization, involving a genetic algorithm, uses Michell integral to calculate wave resistance. A certain hull form is generated by the method using cross section information of a modified DTMB model ship 5415 and a comparative experiment is carried out. Experimental and calculation result show that the method is of good adaptability for designing certain types of ships with excellent resistance performance.*

**Key words**: hull lines design; wave-making resistance; optimization

## INTRODUCTION

Resistance performance has a significant effect on the operating cost of civil ships and the survivability of military ship. In the optimization design of the hull, it is the total resistance that people care about most [4, 19], which is generally the sum of the viscous resistance and the wave-making resistance. In a sense, once the principal dimensions of a hull are determined, there is no significant wetted surface change and the optimization design of hull form is to obtain a hull form with the minimum wave-making resistance [1]. Further more, for high-speed ship, it is reasonable to take the wave-making resistance as a major objective in the optimization design because of its high proportion in the total resistance [22].

Wave-making resistance can be greatly reduced by employing excellent hull form or optimization of some existing hull offsets. Shape optimization is a growing field of interest in many areas of research, such as marine design and manufacturing. Wilson, Hendrix, and Gorski [20] develop a computational tool set and process framework help designers to decide the hull shape, which had great effect on its hydrodynamic characteristics.

In order to obtain a hull with the minimum wave-making resistance, designers often try to make improvement of parent hull. This requires lots of ship design experience, without mentioning the uncertain improvement [21]. Chen and Guang [2] optimized the shape of the after hull based on the desired wake distribution, using B-spline surface method to generate the surface geometry of ship. Peri, Rossetti, and Campana [16] carried out numerical shape optimization of a tanker ship with the aid of CFD techniques and experimentally verified. The hull form optimization often concerns one of the most important applications of wave-making resistance theories. Grigoropoulos and Chalkias [7] developed a formal methodology for the hull form optimization, using parametric hull form modeling to generate the variant hull forms, in which Rankine-source panel method and strip theories were both involved.

Development of a three-dimensional hull fairing form is one of the main requirements in the design of a marine vehicle. The final hull form must satisfy both the desired shape and performance characteristics, such as resistance performance [17]. Ghassemi and Ghiasi [6] developed a numerical program to determine the total resistance of planing crafts, and four different hull forms of Series 62 model 4666 planning craft were presented as calculation examples. A parametric approach to design of hull form was studied by Zhang, Zhu, and Leng [23], which provided the means for quick generation and variation of hull form for the hydrodynamic optimization of hull form. Pérez, Clemente, Suárez, and González [14] used explicit spline curves to make a wire model of the ship stations. An inverse design algorithm in determining the optimal shape of the bulbous bow was developed by Chen, Huang, and Fang [3], with the Levenberg-Marquardt method and B-spline surface control technique utilized.

Genetic algorithm has been used widely in hull design since it appeared several yeast ago. A Multidisciplinary design

optimization method was used to optimize the DTMB model ship 5415 by Peri and Campana [15], while Gammon [5] conducted optimization to fishing vessels applying a Multi-Objective Genetic Algorithm. Li [10] proposed a hybrid approach for multi-objective optimization of ship's principal parameters in conceptual design, employing a multiple objective genetic algorithm. Lu, Lin, and Ji [11] calculated the free trim hydrostatic ship characteristics applying the genetic algorithm, and some necessary improvement was made in practice to speed up the evolution. Kim and Yang [9] utilized A multi-objective genetic algorithm to develop a hull surface modification technique for the CFD-based hull form optimization.

Mathematical ship enjoys popularity among ship designers due to its good adaptability and excellent processing performance [12].The paper is going to develop a method for mathematical hull lines design, including the optimization calculation of the ship resistance. A kind of quadratic curve is used to generate a certain hull of the minimum wetted surface, and smoothness of the designed lines is discussed. A genetic algorithm is used to modify cross section of the hull and Michell integral is applied to solve the wave-making resistance in the optimization procedure. Numerical calculations and comparative experiments are conducted to assess the availability of the method.

## HULL LINES DESIGN

### *Cross section constructed by quadratic curve*

Quadratic curve is applied to construct cross section of the hull; the main process is discussed in the following parts. There are some conditions must be meet first:

**Condition 1**: The ship has only one symmetric plane called the centerplane. The shape of underbody of the ship is shown in Fig. 1.

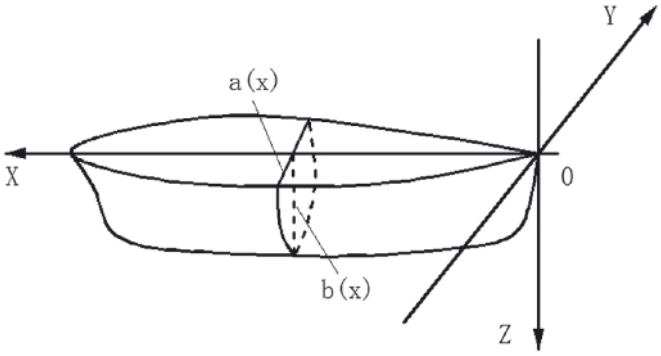


***Fig. 1.*** *Underbody of the hull*

**Condition 2**: Half of the cross section presents with certain types of shape as Fig. 2 shows.

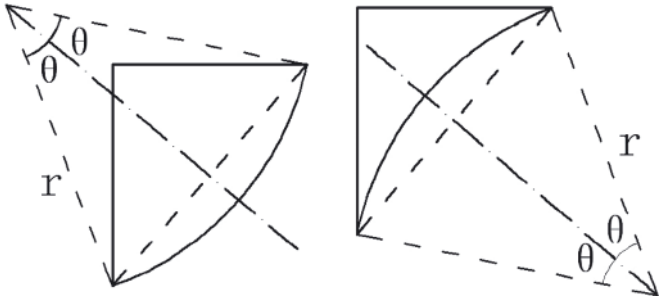


***Fig. 2.*** *Certain types of cross section constructed with arc curve*

**Condition 3**: Both the middle buttock line and designed waterline are fairing.

A Cartesian coordinate system, as shown in Fig. 1, is defined with the x-axis coincident with heading direction of the ship, and positive distance measured upstream. Let L be hull length, so the value of X ranges in [0, L]. Middle line $L_1$ is indicated with function b(x), designed waterline $L_2$ with function a(x), and half of cross section area with function S(x). Within the scope of [0, L], a(x), b(x) and S(x) are all bounded and smooth functions, and their first derivatives are continuous. As the hull has a symmetry plane called the middle sheer plane, only hull lines and section areas of the starboard side ($y \geq 0$) are discussed. The paper is to discuss the underbody of hull, and lines above the designed waterline will not be involved.

The shape of the underbody, which can be expressed by a bunch of body lines, is indicated with a mathematical equation as follows:

$$\frac{z^2}{b(x)^2}+\frac{y^2}{a(x)^2}+czy=1 \tag{1}$$

Where $c = c(x)$ is an undetermined parameter used to modify the cross section. A new parameter $\beta$ is introduced:

$$\beta(x) = 2S(x)/a(x)b(x) \tag{2}$$

Assuming that cross section area of the hull reaches the maximum when $x = L/2$, that is to say, there exists $x_0 \in [0, L/2]$ making $\beta(x_0) = 1$.

### *Mathematical analysis of the approximate minimum wetted surface area*

To gain a hull of good resistance performance, mathematical process is taken to analysis character the quadratic curve that constructs the cross section. As we know, arc length is the shortest to that of any curve with the same area. A comparison of the length between the curves mentioned above is taken in this section.

As it is shown in Fig. 2, the circular arc is defined with radius r and central angle 2θ. We have:

$$\begin{cases} r\sin\theta=\frac{1}{2}\sqrt{a(x)^2+b(x)^2} \\ r^2\theta=\frac{1}{2}\sqrt{a(x)^2+b(x)^2}\,r\cos\theta+S(x)-\frac{1}{2}a(x)b(x) \end{cases} \tag{3}$$

Let $l_{circle}$ be length of the circular arc, then:

$$l_{circle} = 2r\theta \tag{4}$$

The quadratic curve can be expressed as:

$$y(z)=-\frac{1}{2}a(x)^2cz+a(x)\sqrt{1-\left(\frac{1}{b(x)^2}-\frac{1}{4}a(x)^2c^2\right)z^2} \tag{5}$$

Let $l_{conic}$ be length of the quadratic curve, then:

$$l_{conic}=\int_0^{b(x)}\sqrt{1+[y'(z)]^2}\,dz \tag{6}$$

Area of cross sections:

$$S(x)=\int_0^{b(x)}\left(-\frac{1}{2}a(x)^2cz+a(x)\sqrt{1-(\frac{1}{b(x)^2}-\frac{1}{4}a(x)^2c^2)z^2}\right)dz \tag{7}$$

The discussion of Eq. (1) for $x < x_0$, $x = x_0$ and $x > x_0$ is detailed in appendix A and Length of the two kinds of curve mentioned above are calculated. Solutions of the Eq. (1) are discussed as well and the conclusion becomes:

- when $0 \le x < x_0$, namely $\beta(x) = 2S(x)/a(x)b(x) < 1$, and $c > 2/a(x)b(x)$ Eq. (1) has at least one nontrivial solution;
- when $x = x_0$, namely: $\beta(x) = 2S(x)/a(x)b(x) = 1$, and $c = 2/a(x)b(x)$ Eq. (1) has at least one nontrivial solution;
- when $x < x_0 \le L/2$, namely: $\beta(x) = 2S(x)/a(x)b(x) > 1$, and $c < 2/a(x)b(x)$ Eq. (1) has at least one nontrivial solution.

With a set of cross sections, of which breadths, draughts and areas are limited in a certain range, one can calculate the length of the designed quadratic curve and the circular arc. Most of the relatively error is less than 0.05% by comparing the designed quadratic curves with circular arcs, as illustrated in Fig. 3, and the maximum error is only 0.11%.

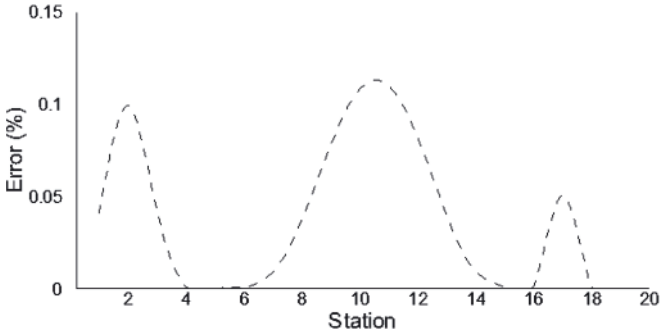


***Fig. 3.*** *Length error of the designed curve to circular arc at every station*

It is not difficult to get a conclusion that hulls consisted of the designed cross section curves can be approximately seen as hulls of the minimum wetted area.

## *Simple mathematical discussion of rationality of the designed hull lines*

In the following part, whether the designed lines are accordant with the practical situation is discussed, that is:
- whether the first derivatives with respect to x of any waterline and buttock line are smooth.
- whether changes of signs of the second derivative with respect to x of any waterline and buttock line are in accordance with general law of hull lines.

A theorem for implicit differentiation is introduced firstly. Suppose that F(y, z) meets the following conditions:
- in the domains $|z - z_0| \le \delta$ and $|y - y_0| \le \lambda$, both $F_z$ and $F_y$ are continuous.
- $F(y_0, z_0) = 0$
- $F_y(y_0, z_0) \ne 0$

These lead to some conclusions:
- in a certain neighborhood of point $(y_0, z_0)$, $F(y, z) = 0$ uniquely determines a function $y = f(z)$; and $y_0 = f(z_0)$. In other words, $y = f(z)$ is defined within a certain neighborhood $O(z_0, \eta)$ of $z_0$, meeting $F(z, f(z)) \equiv 0$ and $y_0 = f(z_0)$;
- $y = f(z)$ is continuous in the domain $O(z_0, \eta)$;

The first derivative of $y = f(z)$ is continuous in the domain $O(z_0, \eta)$, and at any point where $F_y \ne 0$, $y' = -F_z(y, z)/F_y(y, z)$.

On the basis of the theorem mentioned above, the implicit function that $c = c(x)$ meets is analyzed as follows:
- when $0 \le x < x_0$, namely $\beta(x) < 1$, Eq. (A5) can be expressed as:

$$F(x,c) = \exp\left(\beta\sqrt{\frac{a(x)^2b(x)^2c^2}{4}-1}\right) + \\ -\sqrt{\frac{a(x)^2b(x)^2c^2}{4}-1}-\frac{1}{2}a(x)b(x)c = 0 \tag{8}$$

- when $x < x_0 \le L/2$, namely $\beta(x) > 1$, Eq. (A13) can be expressed as:

$$F(x, c) = \sin\left(\beta\cdot\sqrt{1-\frac{a(x)^2b(x)^2c^2}{4}}\right) + \\ -\sqrt{1-\frac{a(x)^2b(x)^2c^2}{4}} = 0 \tag{9}$$

For arbitrary $x \in [0, x_0)$ or $x \in (x_0, L/2)$, it is easy to validate that $F(x, 2/a(x)b(x)) = 0$, $F_c(x, 2/a(x)b(x)) \ne 0$, where $F_c$ and $F_x$ are continuous in a small enough neighborhood of x.

In that case, it can be concluded that $c = c(x)$ is continuously differentiable function in domain $[0, x_0)$ and $(x_0, L/2]$. Since both equations have the solution $c(x_0) = 2/a(x_0)b(x_0)$, $c = c(x)$ is continuous in the domain $[0, L/2]$. A complete process is detailed in appendix B.

The first and second derivative of y can be written as:

$$y'(x) = -a'ah-\frac{1}{2}a^2c'h+a'\sqrt{1-\left(\frac{1}{b^2}-\frac{1}{4}a^2c^2\right)h^2} \\ +\frac{ah^2\left(\frac{b'}{b^3}+\frac{1}{4}aa'c^2+\frac{1}{4}a^2cc'\right)}{\sqrt{1-\left(\frac{1}{b^2}-\frac{1}{4}a^2c^2\right)h^2}},\ x\in[0, L/2] \tag{10}$$

— — — — — — — — — —

$$y''(x) = -a'^2cz-2aa'c'z-aca''z+ \\ -\frac{1}{2}a^2c''z+a''\sqrt{1-\left(\frac{1}{b^2}-\frac{1}{4}a^2c^2\right)z^2}+ \\ -\frac{a'\left(-\frac{2b'}{b^3}-\frac{1}{2}ac^2a'-\frac{1}{2}a^2cc'\right)z^2}{\sqrt{1-\left(\frac{1}{b^2}-\frac{1}{4}a^2c^2\right)z^2}}+ \\ -\frac{1}{4}\frac{a\left(-\frac{2b'}{b^3}-\frac{1}{2}ac^2a'-\frac{1}{2}a^2cc'\right)^2z^4}{\left(1-\left(\frac{1}{b^2}-\frac{1}{4}a^2c^2\right)z^2\right)^{3/2}}+ \\ -\frac{1}{2}\frac{1}{\sqrt{1-\left(\frac{1}{b^2}-\frac{1}{4}a^2c^2\right)z^2}}\left[a\left(\frac{6b'^2}{b^4}-\frac{2b''}{b^3}-\frac{1}{2}a'^2c-2aca'c'+\right.\right. \\ \left.\left.-\frac{1}{2}ac^2a''-\frac{1}{2}a^2c'^2-\frac{1}{2}a^2cc''\right)z^2\right],\ x\in[0, L/2] \tag{11}$$

It is clear that the waterlines of the hull are feasible from the discussion above. Since y and z are interchangeable in Eq. (1), a similar conclusion about the buttock lines can be got as well.

## Wave-making resistance optimization and sample designs

### *Wave-making resistance calculation*

Since [13] published one of his scientific papers in 1898, the famous Michell integral has made great achievements in ship wave-making resistance and hull optimization. The basic formulas of Michell integral are written as follows [18]:

$$R_w = \frac{4\rho g^2}{\pi U^2}\int_1^{\infty}(I^2+J^2)\frac{\lambda^2}{\sqrt{\lambda^2-1}}d\lambda \tag{12}$$

$$I = \iint_H \eta_x(x,z)e^{\lambda^2 gz/U^2}\cos(\lambda g x/U^2)dxdz \tag{13}$$

$$J = \iint_H \eta_x(x,z)e^{\lambda^2 gz/U^2}\sin(\lambda g x/U^2)dxdz \tag{14}$$

Where $\eta(x, z)$ defines the geometry of the hull, g is acceleration of gravity and U indicates the moving velocity of hull. As have been defined above, x-axis is coincident with heading direction of the ship, and z-axis is coincident with draught direction the ship.

In the research, a numerical program is conducted applying Michell integral to calculate wave-making resistance of hulls. Before the calculation, the Wigley N43 hull is used to check the accuracy of the numerical procedure. Line function of the hull can be written as [8]:

$$y = \frac{B}{2}\times\left[\left(1-(\frac{2x}{L})^2\right)\left(1-(\frac{z}{T})^2\right)\left(1+0.2(\frac{2x}{L})^2\right)+ +\left(\frac{z}{T}\right)^2\left(1-(\frac{z}{T})^8\right)\left(1-(\frac{2x}{L})^2\right)^4\right] \tag{15}$$

Wave-making resistance coefficient $C_w$ is defined as:

$$C_w = \frac{R_w}{\frac{1}{2}\rho D^{2/3}V^2} \tag{16}$$

where $R_w$ is wave-making resistance of the hull in N, D is the hull displacement in kg, and V is the heading velocity of the ship in m/s. Curves of $C_w$ versus Froude Number are presented in Fig. 4 to compare the result calculated in the program with that Wigley got from the calculations and experiments, with the ordinate representing the coefficient of wave-making resistance, and the abscissa the Froude number.

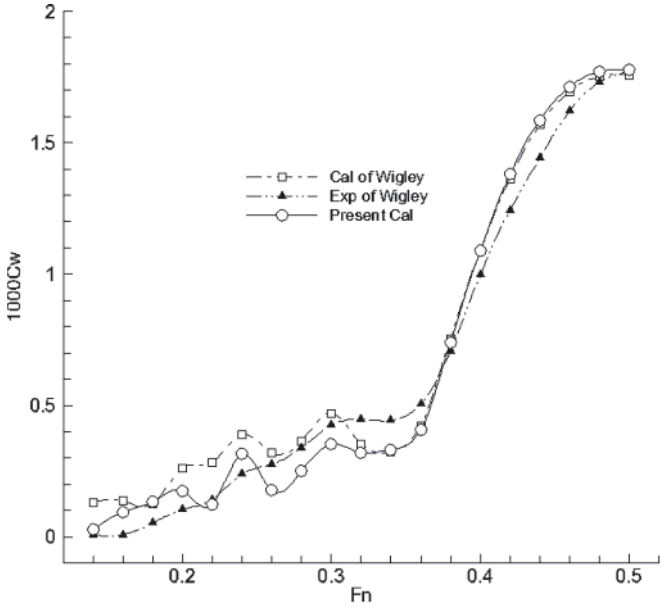


***Fig. 4.*** *Wave-making resistance comparison of present calculation with that of Wigley's and the experimental result for Wigley N43 model*

As it is illustrated in Fig. 4, though the agreement of the calculation at low Froude Number is not so perfect, the result show in this paper shows good agreement with that Wigley got at high Froude Number (Fr > 0.32).

## *Genetic algorithm*

A genetic algorithm optimization model is applied and the numerical procedure is shown as follows:

The hull is divided into 21 stations in the direction of length. Since the section area of the No.0 station and No.20 station are zero, section areas of No.1 station to No.19 station are defined as designed variables:

$$\overline{X} = \{xi\},\ i - 1, 2, ..., 19 \tag{17}$$

Michell integration is used as the target function, that is, the adaptive function of genetic algorithm, and the volume of displacement of the ship as the constraint condition. 5 percentages more of section area of parent hull is taken as the upper limit of the optimum region ($X_U$) while 5 percentages less of that as the lower limit of the optimum region ($X_L$).Then, the optimum model can be expressed as:

$$\begin{aligned} &\text{Target funktion Min} && R_w = R_w(X, U)\\ &\text{Subject to} && g_1: x_i > X_L\\ & && g_1: x_i < X_U\\ & && g_1: (\Delta - \Delta_0)/\Delta < 5‰ \end{aligned} \tag{18}$$

Where Rw is wave-making resistance, U is the moving velocity of hull and $\Delta$ indicates the volume displacement of the hull. Since the volume of displacement constraint condition is nonlinear, we use the punishment coefficient method to simplify the computational process, and the punishment function can be written as

$$Rw(X, U, \Delta) = Rw + M\left(\frac{\Delta-\Delta_0}{\Delta}\right)^N \tag{19}$$

Where M and N are coefficient that need to be determined. Since it is difficult for genetic algorithm to deal with both M and N, we can make N constant and M a kind of descending series.

## *Design sample and analysis*

Lines designing example of a hull is shown in the following, with the modified DTMB model ship 5415 used as the parent hull, of which the bulbous bow is removed. The main principles are listed in Table 1.

***Tab. 1.*** *Main parameters of the parent ship*

| Parameter | Value |
|---|---|
| Displacement [t] | 12129 |
| Length overall [m] | 172.5 |
| Beam [m] | 23.09 |
| Depth [m] | 12.34 |
| Volume of displacement [m$^3$] | 11785.6 |
| Amid ship section coefficient $C_m$ | 0.817 |
| Length on the waterline [m] | 160.0 |
| Waterline breadth [m] | 21.46 |
| Draught [m] | 6.927 |
| Prismatic coefficient $C_p$ | 0.607 |
| Block coefficient $C_h$ | 0.496 |

Since the hull lines of new ship generated is similar to the parent hull as it is shown in Fig. 5, resistance test of 1/30 scale models of the two ships are performed in the towing tank of Huazhong University of Science & Technology respectively for further comparison and analysis. The experimental temperature is about 18.0°C, and the models are kept afloat on an even keel during the test. Some useful parameters are shown in Table 2.

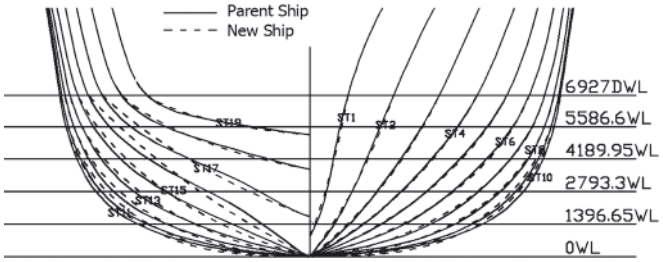


***Fig. 5.*** *Lines of the parent ship and the designed one*

***Tab. 2.*** *Some useful information for the experiment*

| Parameter | Parent ship model | New ship model |
|---|---|---|
| Wetted surface area [m²] | 3.893 | 3.905 |
| Displacement [kg] | 438.5 | 436.0 |
| Average draught [m] | 0.2309 | 0.2309 |

The resistance of the models tested in the experiment is converted to that of the full-scale ships, and the total resistance coefficient and residual resistance coefficient of the hulls are shown in Fig. 6. Experimental result indicates that the resistance of the new ship is similar to that of the parent hull. With the velocity of full-scale ship ranging from 22 to 36 knots, the total resistance of designed hull is 1% averagely more than that of the parent ship. Taking the average accuracy of model experiment into account, a conclusion can be drawn that resistance of the designed ship has no obvious change compared with that of the parent hull (Fig. 6). Obviously, the wetted surface area of the new ship declines slightly. These is probably because: firstly, the wetted surface area coefficient of the parent ship model is too small to bear too much change; secondly, on the condition that the displacement and the principal dimensions are almost the same, when the character of the body lines changed a little, it leads to no big difference in decreasing the wetted surface area.

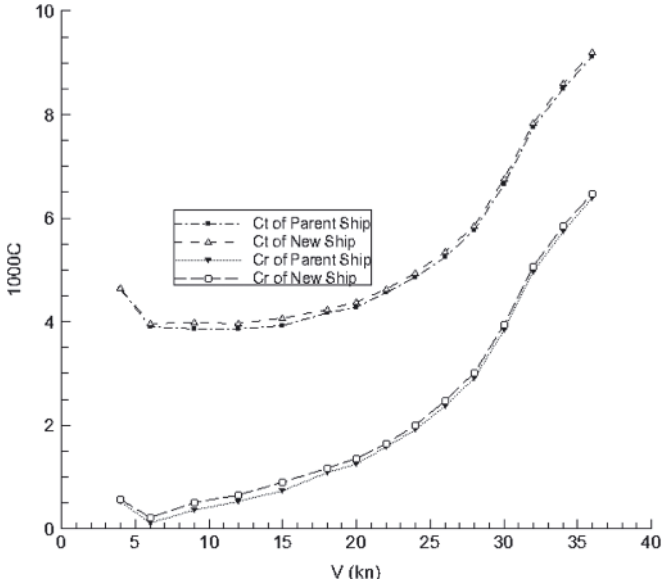


***Fig. 6.*** *Comparison of resistance coefficient of the new hull with that of the parent one*

Optimization of designed ship of full-scale is conducted, using Michell integral and the genetic algorithm mentioned above. Some different velocities such as 26kn (Fr = 0.338), 28kn (Fr = 0.364), 30kn (Fr = 0.390), 32kn (Fr = 0.416) are taken into account. As have been stated, the wave-making resistance is taken as the target function. New section area curves of different resistance performance are obtained. The cross section area curves of different velocities are shown in Fig. 7, compared with that of parent ship.

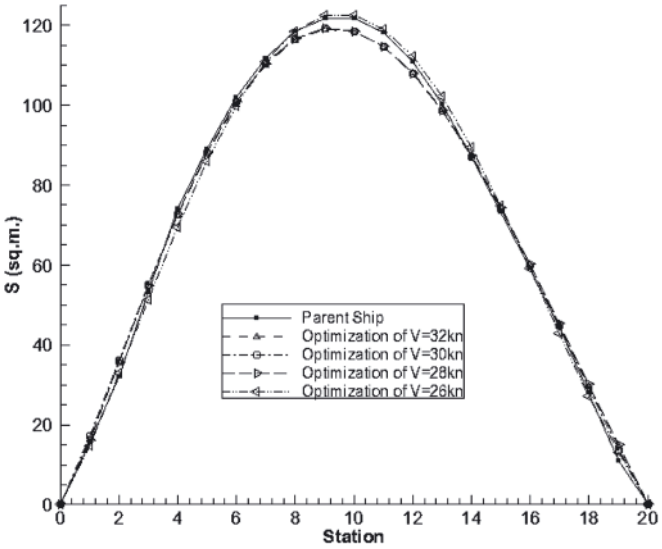


***Fig. 7.*** *Transverse-section area curves of different velocities optimization compared with that of parent ship*

Comparison wave-making resistance coefficient is shown in Fig. 8. The calculation result of 26kn shows good resistance performance at low velocity, while the wave-making resistance at high speed has no obvious improvement. Calculation result of 28kn and 30kn show just a little change at low speed in wave-making resistance, but the improvement at high speed is noticeable. Based on an overall consideration of different velocities, optimization result of 28kn is chosen for hull lines optimization.

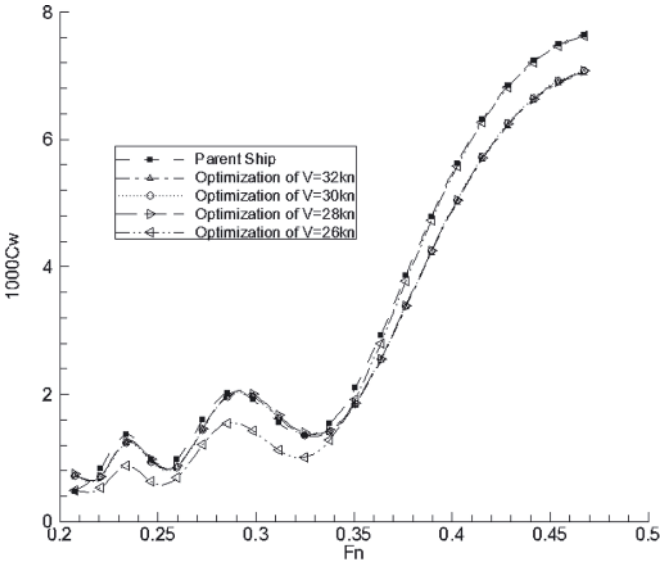


***Fig. 8.*** *Coefficient of wave-making resistance of different velocities optimization compared with that of parent ship*

Wave-making resistance coefficients of parent hull and the optimized one at 28 knots, compared with experimental result, are shown in Fig. 9. Lines of the designed hull and the optimized one are shown in Fig. 10. Since cross section areas of the hull vary in a small range, lines of hull dose not have

much change. That is to say, with just a little change of hull lines, the hull can get some noticeable improvement in wave making resistance performance.

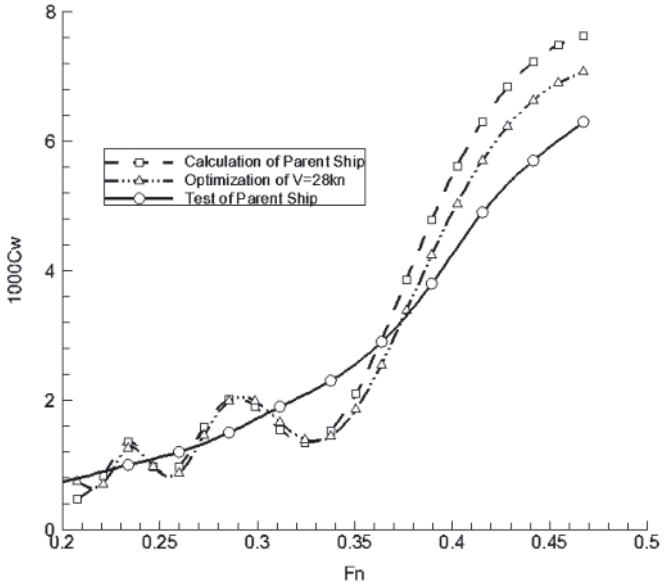


***Fig. 9.*** *Comparison of calculation result with experimental result*

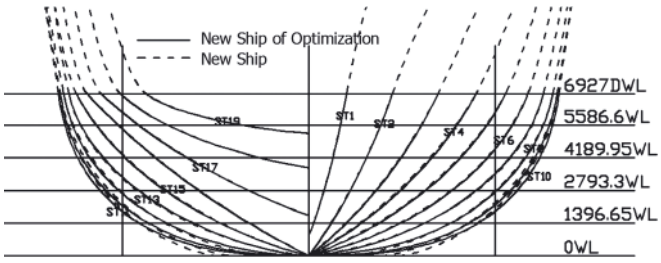


***Fig. 10.*** *Lines of the designed hull and the optimized one*

In general, the wave-making resistance performance of the new hull is close to that of the parent hull. At low Froude number, the wave-making resistance coefficient of optimized hull is a little smaller. However, when the Froude number is higher, the coefficient of optimized hull is apparently smaller than that of parent one. That is to say the wave-making resistance performance of optimized hull has been obviously improved though the result coincides well with experimental result at low Froude number but not very well at high Froude number.

## CONCLUSION

A hull lines design method, which involved wetted surface analysis and wave-making optimization, is applied with the intent of designing hulls of good resistance performance using a given set of constraints. A certain kind of quadratic curve is used to generate hull lines, of which the feasibility is proved in a brief theoretical analysis; approximate minimum wetted surface of the hull is calculated as well. Hull lines are proved smooth through mathematical procedure, in which both the first and second differentials of the line functions are derived. A program is compiled to calculate wave-making resistance of hulls using Michell integral and the Wigley hull model is taken as an example of validation. A DTMB model ship 5415 is used as an example of hull form optimization designing, applying a genetic algorithm. The particular genetic algorithm developed during this study uses the wave-making resistance as the objective function and allows automatic modification of cross section curve. Experiment result of new hull and the parent hull indicate that the hull optimization designing method is practical. With respect to the calculation result, the wave-making optimized hull is of good resistance performance.

### Appendix A

Discussion of Eq. (1) for $x < x_0$, $x = x_0$ and $x > x_0$ is shown as follows:

1) When $x < x_0$, namely $\beta(x) = 2S(x)/a(x)b(x) < 1$:

- when $c < 2/a(x)b(x)$ namely $1/b(x)^2 - a(x)^2c^2/4 > 0$:

$$S(x)=\frac{a(x)}{2\sqrt{1/b(x)^2-a(x)^2c^2/4}}\cdot\arcsin\sqrt{\frac{1-a(x)^2b(x)^2c^2}{4}} \tag{A1}$$

then:

$$\sin\left(\beta\cdot\sqrt{1-\frac{a(x)^2b(x)^2c^2}{4}}\right)=\sqrt{1-\frac{a(x)^2b(x)^2c^2}{4}} \tag{A2}$$

Since there exists a unique zero solution of equation $z = \sin\beta z$, then $1/b(x)^2 - a(x)^2c^2/4 = 0$ i.e. $c = 2/a(x)b(x)$, which contradicts the previous assumptions. Thus, Eq. (1) has no nontrivial solution.

- when $c = 2/a(x)b(x)$ namely $1/b(x)^2 - a(x)^2c^2/4 = 0$:

$$S(x) = a(x)b(x)/2 \tag{A3}$$

then $\beta(x) = 1$ and it contradicts the previous assumptions. Eq. (1) has no nontrivial solution.

- when $c > 2/a(x)b(x)$, namely $1/b(x)^2 - a(x)^2c^2/4 < 0$:

$$S(x)=\frac{a(x)b(x)}{2\sqrt{\frac{a(x)^2b(x)^2c^2}{4}-1}}\ln\left(\sqrt{\frac{a(x)^2b(x)^2c^2}{4}-1}+\frac{1}{2}a(x)b(x)c\right) \tag{A4}$$

then:

$$\exp(\beta\sqrt{\frac{a(x)^2b(x)^2c^2}{4}-1})=\sqrt{\frac{a(x)^2b(x)^2c^2}{4}-1}+\frac{1}{2}a(x)b(x)c \tag{A5}$$

By using Taylor expansion, an approximate solution of c can be got:

$$c(x)=\frac{2\sqrt{\left(\frac{3-3\beta(x)^2-\sqrt{-15\beta(x)^4+24\beta(x)^3-18\beta(x)^2+9}}{2(\beta)x^2}\right)^2+1}}{a(x)b(x)} \tag{A6}$$

Since the equation $e^{\beta z}=z+\sqrt{z^2+1}$ has nontrivial solutions when $\beta < 1$, the conclusion comes out that Eq. (1) has solutions. $l_{conic}$ can be solute by considering Eq. (6) and (A6).

2) When $x = x_0$, namely $\beta(x) = 2S(x)/a(x)b(x) = 1$:
- when $c < 2/a(x)b(x)$, namely $1/b(x)^2 - a(x)^2c^2/4 > 0$

$$S(x)=\frac{a(x)}{2\sqrt{1/b(x)^2-a(x)^2c^2/4}}\cdot\arcsin\sqrt{\frac{1-a(x)^2b(x)^2c^2}{4}} \tag{A7}$$

then:

$$\sin\sqrt{1-\frac{a(x)^2b(x)^2c^2}{4}}=\sqrt{1-\frac{a(x)^2b(x)^2c^2}{4}} \tag{A8}$$

Since there exists a unique zero solution of equation $z = \sin z$, then $1/b(x)^2 - a(x)^2c^2/4 = 0$ i.e. $c = 2/a(x)b(x)$, which contradicts the previous assumptions. Eq. (1) has no nontrivial solution.

- when $c = 2/a(x)b(x)$, namely $1/b(x)^2 - a(x)^2c^2/4 = 0$. It is easy to verify that Eq. (1) has at least one nontrivial solution. Substituting the equation above into Eq. (1):

$$\frac{z^2}{b(x_0)^2}+\frac{y^2}{a(x_0)^2}+\frac{2}{a(x_0)b(x_0)}yz=1 \tag{A9}$$

namely:

$$\left(\frac{z}{b(x_0)}+\frac{y}{a(x_0)}\right)^2=1 \tag{A10}$$

The designed curve and circular arc are both turned to lines of the same expression $z/b(x_0) + y/a(x_0) = 1$, and the curve length $l_{conic}=l_{circle}=\sqrt{a^2+b^2}$.

- when $c > 2/a(x)b(x)$, namely $1/b(x)^2 - a(x)^2c^2/4 < 0$:

$$S(x)=\frac{a(x)b(x)}{2\sqrt{\frac{a(x)^2b(x)^2c^2}{4}-1}}\cdot\ln\left(\sqrt{\frac{a(x)^2b(x)^2c^2}{4}-1}+\frac{1}{2}a(x)b(x)c\right) \tag{A11}$$

then:

$$\exp(\beta\sqrt{\frac{a(x)^2b(x)^2c^2}{4}-1})=\sqrt{\frac{a(x)^2b(x)^2c^2}{4}-1}+\frac{1}{2}a(x)b(x)c \tag{A12}$$

Since there exists a unique zero solution of equation $e^z = z+\sqrt{z^2+1}$, then $1/b(x)^2 - a(x)^2c^2/4 = 0$ i.e. $c = 2/a(x)b(x)$, which contradicts the previous assumptions. Thus, Eq. (1) has no nontrivial solution.

3) When $x_0 < x$, namely $\beta(x) = 2S(x)/a(x)b(x) > 1$
- when $c < 2/a(x)b(x)$, namely $1/b(x)^2 - a(x)^2c^2/4 > 0$:

$$S(x)=\frac{a(x)}{2\sqrt{\frac{1/b(x)^2-a(x)^2c^2}{4}}}\cdot\arcsin\sqrt{\frac{1-a(x)^2b(x)^2c^2}{4}} \tag{A13}$$

then:

$$\sin\left(\beta\cdot\sqrt{1-\frac{a(x)^2b(x)^2c^2}{4}}\right)=\sqrt{1-\frac{a(x)^2b(x)^2c^2}{4}} \tag{A14}$$

By using Taylor expansion, an approximate solution of c can be got:

$$c(x)=\frac{2\sqrt{1-\dfrac{10\beta(x)-\sqrt{120\beta(x)-20\beta(x)^2}}{\beta(x)^3}}}{a(x)b(x)} \tag{A15}$$

Since the equation $z = \sin z$ has nontrivial solutions when $\beta > 1$, Eq. (1) has at least a nontrivial solution. Curve length $l_{conic}$ can be calculated by solving Eq. (6) and (A15).

- when $c = 2/a(x)b(x)$, namely $1/b(x)^2 - a(x)^2c^2/4 = 0$:

$$S(x) = a(x)b(x)/2 \tag{A16}$$

That is $\beta(x) = 1$, which contradicts the previous assumption $\beta(x) > 1$. Thus, Eq. (1) has no nontrivial solution.

- when $c > 2/a(x)b(x)$, namely $1/b(x)^2 - a(x)^2c^2/4 < 0$:

$$S(x)=\frac{a(x)b(x)}{2\sqrt{\dfrac{a(x)^2\,b(x)^2\,c^2}{4}-1}}\ln\left(\sqrt{\frac{a(x)^2b(x)^2\,c^2}{4}-1}+\frac{1}{2}a(x)b(x)c\right) \tag{A17}$$

then:

$$\exp\left(\beta\sqrt{\frac{a(x)^2\,b(x)^2\,c^2}{4}-1}\right)=\sqrt{\frac{a(x)^2\,b(x)^2\,c^2}{4}-1}+\frac{1}{2}a(x)b(x)c \tag{A18}$$

Since the equation $e^{\beta z} = z+\sqrt{z^2+1}$ has no solutions when $\beta > 1$, Eq. (1) has no solutions yet.

## Appendix B

Discussion of the continuity of waterlines function is shown as follows:
The first derivative of c with respect to z is calculated as follows:
1) When $x \in [0, x_0)$, $c = c(x)$ is defined by Eq. (8). Let:

$$O(x)=\sqrt{\frac{1}{4}a(x)^2b(x)^2c(x)^2-1} \tag{B1}$$

Eq. (8) can be written as:

$$\beta(x)O(x)=\ln(O(x)+\sqrt{O(x)^2+1})$$

Differentiate both sides of the equation with respect to x, and then we have:

$$O(x)O'(x)=\frac{\beta'(x)O(x)^2\sqrt{O(x)^2+1}}{1-\beta(x)\sqrt{O(x)^2+1}} \tag{B2}$$

Let $\lim\limits_{x\to x_0^+}O(x)O'(x) = I$. A simple form of Eq. (B2) can be got by using L'Hôpital's Rule:

$$I=\lim_{x\to x_0^+}O(x)O'(x)=\beta'(x_0)\frac{2I}{-\beta'(x_0)-I} \tag{B3}$$

namely:

$$\lim_{x\to x_0^+}O(x)O'(x)=I=-3\beta'(x_0) \tag{B4}$$

then:

$$O'(x)=-\frac{a'(x)a(x)b(x)^2c(x)^2+a(x)^2b(x)b'(x)c(x)^2+a(x)^2b(x)^2c(x)c'(x)}{4\sqrt{1-\dfrac{1}{4}a(x)^2b(x)^2c(x)^2}} \tag{B5}$$

Solve Eq. (B1) and (B5), then:

$$c'(x)=\frac{4O(x)O'(x)-a'(x)a(x)b(x)^2c(x)^2-a(x)^2b(x)b'(x)c(x)^2}{a(x)^2b(x)^2c(x)} \tag{B6}$$

Simplify the equation, and we can get the left-hand limit of c'(x) at $x_0$:

$$\lim_{x\to x_0^+}c'(x)=-\frac{6\beta'(x_0)+a'(x_0)b(x_0)c(x_0)+a(x_0)b'(x_0)c(x_0)}{a(x_0)b(x_0)} \tag{B7}$$

2) When $x \in (x_0, L/2]$, $c = c(x)$ is defined by Eq. (9). Let:

$$O(x)=4\sqrt{1-\frac{1}{4}a(x)^2b(x)^2c(x)^2} \tag{B8}$$

Eq. (9) can be written as:

$$\sin(\beta(x)O(x)) = O(x) \tag{B9}$$

Differentiate both sides of the equation with respect to z, and then we have:

$$O(x)O'(x) = \frac{\beta'(x)O(x)^2\cos(\beta(x)O(x))}{1-\beta(x)\cos(\beta(x)O(x))} \tag{B10}$$

Let $\lim_{x\to x_0^+} O(x)O'(x) = I$. A simple form of Eq. (B9) can be got by using L'Hôpital's Rule:

$$I = \lim_{x\to x_0^+} O(x)O'(x) = \beta'(x_0)\frac{2I}{I-\beta'(x_0)} \tag{B11}$$

namely:

$$\lim_{x\to x_0^+} O(x)O'(x) = I = 3\beta'(x_0) \tag{B12}$$

then:

$$O'(x) = -\frac{a'(x)a(x)b(x)^2c(x)^2 + a(x)^2b(x)b'(x)c(x)^2 + a(x)^2b(x)^2c(x)c'(x)}{4\sqrt{1-\frac{1}{4}a(x)^2b(x)^2c(x)^2}} \tag{B13}$$

Solve Eq. (B8) and (B13):

$$c'(x) = -\frac{4O(x)O'(x) + a'(x)a(x)b(x)^2c(x)^2 + a(x)^2b(x)b'(x)c(x)^2}{a(x)^2b(x)^2c(x)}$$

Simplify the equation, and we can get the right-hand limit of c'(x) at $x_0$:

$$\lim_{x\to x_0^+} c'(x) = -\frac{6\beta'(x_0) + a'(x_0)b(x_0)c(x_0) + a(x_0)b'(x_0)c(x_0)}{a(x_0)b(x_0)} \tag{B14}$$

From Eq. (B7) and (B14), we have $\lim_{x\to x_0^-} c'(x) = \lim_{x\to x_0^+} c'(x)$, namely the left-hand and right-hand limits are equal as $x \to x_0$, that is to say c'(x) is continuous in domain $[x_0, L/2]$.

When z = h, the waterline defined by Eq. (1) can be expressed as:

$$y(x) = \frac{-a(x)^2c(x)h}{2} + a(x)\sqrt{1-\left(\frac{1}{b(x)^2}-\frac{a(x)^2c(x)^2}{4}\right)h^2}\ ,\ x \in [0, L/2] \tag{B15}$$

Since a(x), b(x), c(x) and their first derivatives are all continuous, and it is not difficult to prove that the second derivatives of a(x), b(x), c(x) is continuous, the first and second derivative of y can be written as:

$$y'(x) = -a'ah - \frac{1}{2}a^2c'h + a'\sqrt{1-\left(\frac{1}{b^2}-\frac{1}{4}a^2c^2\right)h^2} + \frac{ah^2\left(\frac{b'}{b^3}+\frac{1}{4}aa'c^2+\frac{1}{4}a^2cc'\right)}{\sqrt{1-\left(\frac{1}{b^2}-\frac{1}{4}a^2c^2\right)h^2}}\ ,\ x \in [0, L/2] \tag{B16}$$

$$\begin{aligned} y''(x) = {} & -a'^2cz - 2aa'c'z - aca''z - \frac{1}{2}a^2c''z + a''\sqrt{1-\left(\frac{1}{b^2}-\frac{1}{4}a^2c^2\right)z^2} \\ & - \frac{a'\left(-\frac{2b'}{b^3}-\frac{1}{2}ac^2a'-\frac{1}{2}a^2cc'\right)z^2}{\sqrt{1-\left(\frac{1}{b^2}-\frac{1}{4}a^2c^2\right)z^2}} - \frac{1}{4}\frac{a\left(-\frac{2b'}{b^3}-\frac{1}{2}ac^2a'-\frac{1}{2}a^2cc'\right)^2z^4}{\left(1-\left(\frac{1}{b^2}-\frac{1}{4}a^2c^2\right)z^2\right)^{3/2}} + \\ & -\frac{1}{2}\frac{1}{\sqrt{1-\left(\frac{1}{b^2}-\frac{1}{4}a^2c^2\right)z^2}}\left[a\left(\frac{6b'^2}{b^4}-\frac{2b''}{b^3}-\frac{1}{2}a'^2c^2 - 2aca'c' - \frac{1}{2}ac^2a''-\frac{1}{2}a^2c'^2-\frac{1}{2}a^2cc''\right)z^2\right]\ ,\ x \in [0, L/2] \end{aligned} \tag{B17}$$

Both Eq. (B16) and (B17) are smooth and continuous.

**BIBLIOGRAPHY**


1. Abramowski T., Żelazny K. and Szelangiewicz T.: *Numerical Analysis of Influence of Ship Hull Form Modification On Ship Resistance and Propulsion Characteristics*, Polish Maritime Research, 17(1): 10-13, 2010.
2. Chen P. and Huang C.: *An Inverse Hull Design Problem in Optimizing the Desired Wake of Ship*, Journal of Ship Research, 46(2): 138-147, 2002.
3. Chen P., Huang C. and Fang M.: *An Inverse Design Approach in Determining the Optimal Shape of Bulbous Bow with Experimental Verification*, Journal of Ship Research, 50(1): 1-14, 2006.

4. Doctors L. J., Day A. H. and Clelland D.: *Resistance of a Ship Undergoing Oscillatory Motion*, Journal of Ship Research, 54(13): 120-12, 2010.
5. Gammon M. A.: *Optimization of Fishing Vessels Using a Multi-Objective Genetic Algorithm*, Ocean Engineering, 38(10): 1054-1064, 2011.
6. Ghassemi H. and Ghiasi M. A.: *Combined Method for the Hydrodynamic Characteristics of Planing Crafts*, Ocean Engineering, 35(3-4): 310-322, 2008.
7. Grigoropoulos G. J. and Chalkias D. S.: *Hull-Form Optimization in Calm and Rough Water*, Computer-Aided Design, 42(11): 977-984, 2010.
8. Havelock T. H.: *Wave Resistance Theory and its Application to Ship Problems*, Society of Naval Architects and Marine Engineers, 1951.
9. Kim H. and Yang C.: *A New Surface Modification Approach for Cfd-Based Hull Form Optimization*, Journal of Hydrodynamics, Ser. B, 22 (5, Supplement 1): 520-525, 2010.
10. Li X.: *Multiobjective Optimization and Multiattribute Decision Making Study of Ship's Principal Parameters in Conceptual Design*, Journal of Ship Research, 53(2): 83-92, 2009.
11. Lu C., Lin Y. and Ji Z.: *Free Trim Calculation Using Genetic Algorithm Based On Nurbs Shipform*, International Shipbuilding Progress, 54(1): 45-62, 2007.
12. Lu C., Lin Y., Ji Z. and Chen M.: *Ship Hull Representation with a Single Nurbs Surface*, Proceedings of the International Offshore and Polar Engineering Conference, Seoul, Korea, 2005.
13. Michell J. H.: *The Wave Resistance of a Ship*, Philosophy Magazine, 5(45): 106-123, 1898.
14. Pérez F. L., Clemente J. A., Suárez J. A. and González J. M.: *Parametric Generation, Modeling, and Fairing of Simple Hull Lines with the Use of Nonuniform Rational B-Spline Surfaces*, Journal of Ship Research, 52(1): 1-15, 2008.
15. Peri D. and Campana E. F.: *Multidisciplinary Design Optimization of a Naval Surface Combatant*, Journal of Ship Research, 47(1): 1-12, 2003.
16. Peri D., Rossetti M. and Campana E. F.: *Design Optimization of Ship Hulls Via Cfd Techniques*, Journal of Ship Research, 45(2): 140-149, 2001.
17. Sarioz E.: *An Optimization Approach for Fairing of Ship Hull Forms*, Ocean Engineering, 33(16): 2105-2118, 2006.
18. TUCK E. O.: *The Wave Resistance Formula of J.H. Michell (1898) and its Significance to Recent Research in Ship Hydrodynamics*, The Journal of the Australian Mathematical Society. Series B. Applied Mathematics, 30(4): 365-377, 1989.
19. Tzabiras G. D.: *A Method for Predicting the Influence of an Additive Bulb On Ship Resistance*, 8th International conference on hydrodynamics, Athens, Greece, 2008.
20. Wilson W., Hendrix D. and Gorski J.: *Hull Form Optimization for Early Stage Ship Design*, Naval Engineers Journal, 122(2): 53-65, 2010.
21. Yoo J.: *Design of Ship's Bow Form by Potential-Based Panel Method*, Ocean Engineering, 34(8-9): 1089-1095, 2007.
22. Zhang B., Ma K. and Ji Z.: *The Optimization of the Hull Form with the Minimum Wave Making Resistance Based On Rankine Source Method*, Journal of Hydrodynamics, 21(2): 277-284, 2009.
23. Zhang P., Zhu D. and Leng W.: *Parametric Approach to Design of Hull Forms*, Journal of Hydrodynamics, Ser. B, 20(6): 804-810, 2008.

**CONTACT WITH THE AUTHORS**

Jianglong Sun[a)], Ph.D., Assoc. Prof.
Xujian Lv[a), 1)], Ph.D.
Weibin Liu[a)], Ph.D., Assoc. Prof.
Hanwen Ning[b)], Ph.D.
Xianwen Chen[a)], Master Graduate Student
[a)] Department of Naval Architecture & Ocean Engineering,
Huazhong University of Science & Technology,
Wuhan 430074, P.R. China
[b)] School of Statistics and Mathematics,
Zhongnan University of Economics and Law,
Wuhan 430074, P.R. China
[1)] Corresponding author. e-mail: lv.xujian@gmail.com

**POLISH MARITIME RESEARCH** 3(75) 2012 Vol 19; pp. 26-35
10.2478/v10012-012-0028-0

# A new method for a preliminary definition of a high–performance rudder for tuna purse seiners

**Alba Martínez–López**, Ph.D. Marine Engineering
**Alicia Munín–Doce**, Marine Engineering
Department of Naval Engineering, University of a Coruńa, Spain

ABSTRACT

*The aim of this paper is to provide a simple method for the definition of a rudder for tuna purse seiners. The model achieved by the application of this method ensures the manoeuvrability of initial turning, course keeping and yaw checking. For this, the results obtained by other authors, through rudder tests and manoeuvrability tests of fishing vessels have been integrated with the recommendations of the International Normative. Finally, in the paper the method is applied to the case of a tuna vessel, providing a rudder model which could be optimised with CFD (Computer Fluid Dynamics) in further tests. The method proposed can be applied to other vessels whose main dimensions are met.*

**Key words:** rudder optimisation; vessel manoeuvrability; tuna vessel design

## INTRODUCTION

Limited manoeuvrability is one of the most significant weak points in the operation of the fishing vessels when compared to other vessels. This is mainly due to the activity of fishing, which means shipping with nets. This characteristic not only leads to inefficient operation and therefore to high fuel consumption, but also to a higher risk of accidents.

Above all, these threats stand out in the case of tuna purse seiners because of their particular manoeuvrability needs throughout their entire voyage; during navigation (the rapid pursuit of fish shoals), during manoeuvres (the releasing of nets at high speed) and whilst tacking (the stability of the vessel during collection of catch).

In order to minimise these weak areas, the current construction tendency in these types of vessel is based on wider dimensions, optimised hydrodynamic behaviour, usage of controllable propellers and high–performance rudders. The objective of these improvements is to reduce running costs and to increase safety during operation.

The main purpose of this paper is to contribute to the definition of high–performance rudders for tuna fishing vessels. For that, a simple definition method will be shown of an optimised rudder model for this type of boat, which serves as a starter point for further trials with CFDs.

The method not only takes into account the manoeuvrability recommendations provided by the International Rules (IMO, SOLAS, and DNV), but also the results achieved in previous experimental manoeuvrability test studies with fishing vessels and rudders.

As a result of the application of this method, the first step obtains the minimum forces necessary of the rudder to meet certain existing manoeuvrability requirements. Then, the data from previous studies will be taken into account in order to relate these forces with the rudder geometric characteristics and its relative position in the vessel.

The rudder model obtained ensures meeting certain manoeuvrability demands and the Classification Societies' (CS) requirements. However, other requirements are not ensured by the model, for this reason some requirements must be checked through testing with CFDs.

This paper shows the base application method for a tuna fishing vessel, thus obtaining the definition of a rudder model.

The method presented can easily be repeated to define rudders for tuna fishing vessels, guaranteeing their compliance to certain operational characteristics.

## METHODS

The manoeuvrability requirements considered have been determined by SOLAS Part C [7], IMO MSC/Circ.1053 and MSC.137 (76) [5, 6] and the Regulations of the Classification Society Det Norske Veritas [4] (Part 3, Chapter 3, Section 2). In addition to the previous compulsory regulations and recommendations, the results achieved during manoeuvrability tests in fishing vessels carried out in the "El Pardo" model basin [2, 3] have been considered, together with the conclusions extracted from other rudder tests [8, 9].

As a consequence of the integrated recommendations provided by these sources, a series of useful expressions will be obtained. These expressions will allow the definition of the rudder geometry, and its relative position in the vessel ensures the realization of certain manoeuvrability requirements such as:

Turning ability. It is a critical issue for tuna purse seiners due to their operational activity. Adhering to the Gertler acceptability criteria, the following expression can be used [2]:

$$D < (-5C_b + 7.2) \cdot L_{pp} \tag{1}$$

The turning circle diameter value can be calculated through the expression [3]:

$$\frac{D}{L_{pp}} = \frac{0.048 L_{pp}}{sen(2\alpha)B} \cdot \frac{\frac{1}{C_b^2}\left(1 + \frac{25(T_{pp} - T_{pr})}{L_{pp}}\right)}{\left(\frac{dF_n}{d\alpha}\right) L_{pp}} MV^2 \tag{2}$$

The initial capacity for manoeuvrability is regulated by the IMO [7]. In accordance with this, the advance ($A_v$) must not exceed 4.5 times the length of the vessel, and the tactical diameter ($D_t$) must be less than 5 times the turning circle length.

Therefore, as a result of model trials and sea testing, the following expression is found:

$$D_t = 1.65D\ C_b + 0.08 \tag{3}$$

After analysis of turn manoeuvre tests with models [2] for boats with block coefficients of less than 0.6 (which is the case of tuna fishing vessels), the following relations can be concluded:

$$D_t = D_v + 0.55D \tag{4}$$

$$D_v = 0.5A_v \tag{5}$$

This way one can define the advance as a function of the turning diameter (D). Taking into consideration the limitations of the D/Lpp ratio and the advance value limit in relation to vessel length, the maximum value turning circle diameter value can now be expressed, as well as the normal minimum force per angle unit.

Course keeping. This can be defined as the ability to maintain a selected straight line course. By varying the rudder degree angle (spiral test) the progression can be observed in relation to the changes. It is desirable that the evolution is stable, positive and that hysteresis does not occur. The degree of leeway for this quality can be determined via the evaluation of the hysteresis loop width (a).

$$a = 18.12 - \frac{46.43}{T'} \tag{6}$$

Where:

$$T' = f\left(\frac{1}{\frac{C_{ft}}{\alpha}}\right) \tag{7}$$

and:

$$\frac{C_{ft}}{\alpha} = \frac{\frac{F_t}{\alpha}}{\frac{1}{2}\rho \cdot A_r \cdot V_r^2} \tag{8}$$

In order to minimise this value it is necessary to maximise (Ft/α).

The yaw checking ability. This ability is verified by the zigzag manoeuvre test, in which moderate changes of course within time and space are measured. The initial zigzag manoeuvre can be evaluated by measuring the number P of Norrbin, which defines the angle of course turned per unit of rudder angle used, once a determined length is navigated [3]:

$$P = K'(1 - T' + T'e^{-1/T'}) > 0.275 \tag{9}$$

The number P is also accepted by IMO [6] to evaluate the initial progression capacity for manoeuvrability.

Through the Nomoto equation, the following expression is obtained [3]:

$$\frac{K'}{T'} = 0.325 \cdot \frac{F_t}{\alpha} \cdot \frac{L_{pp}}{MV^2} \cdot \frac{1}{K_i^2 + K_j^2} \tag{10}$$

This defines the minimum value for the lift force on the rudder by angle unit (Ft/α)

In order to ensure these forces per angle unit of the operation of the rudder (see Fig. 1) it is necessary to relate the said forces to design parameters that are controllable: the relative position of the rudder in the vessel, and the dimensional geometric characteristics of the rudder.

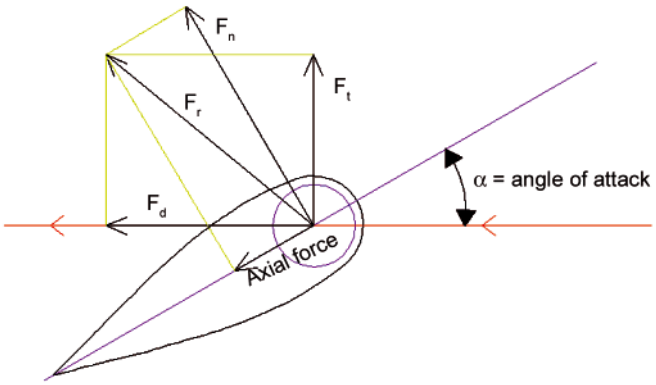


***Fig. 1.*** *Notation of forces on the rudder*

Rudder behaviour is determined to a great extent by the conditions in which it operates, and these are defined greatly by the relative position of the rudder in the vessel, the propeller and the hull [2, 9, 11].

The principle objectives aimed for in the definition of a high performance rudder are the following: the increase of lift force and the decrease of drag force. This resistance is greatly conditioned by the boundary layer of water which is created around the rudder surface. If there is turbulent water flow (high Re), the profile velocity increases and the pressure falls (Bernoulli), which is clearly unfavourable as the drag force increases and lift force decreases.

$$Re = c.Vr/\nu \tag{11}$$

Another motive for avoiding turbulent water flow is the appearance of cavitation. This phenomenon is determined by the profile pressures of the rudder. Profile pressure varies with the rudder section, and in addition to this cavitation can be found in the propeller wake caused by water accelerating from the root to the extremes of the blades. For this we encounter the lowest flow pressures at the extremes of the propeller, and therefore the highest risk of cavitation. Sections of the rudder that coincide with the extremes of the propeller will be critical from the point of view of cavitation.

The influence of rudder angles in cavitation is noticeable, with the risk of cavitation increasing the greater the rudder angle. Rudder angles have an important bearing on tuna purse seiners and the risk of cavitation should be avoided.

$$\sigma \leq -C_p \tag{12}$$

$$\sigma = \frac{P_{at} + \rho \cdot g \cdot hg - P_v}{0.5\rho V_r^2} = \frac{P_0 - P_v}{0.5\rho V_r^2} \quad (13)$$

$$C_p = \frac{P_l - P_0}{(0.5\rho V_r^2)} \quad (14)$$

The relation between pressure and lift coefficients can be expressed in the function of distance ($\hat{y}$) from the origin to the profile surface by:

$$C_{cf} = -\hat{y} \int \left(\frac{C_p}{c}\right) dl \quad (15)$$

Furthermore, the effect of the propeller on rudder behaviour is significant. The propeller creates axial thrust to the water, so the effect is that the water arriving at the rudder has higher velocity. Using Bernoulli and the Gutsche correction, we arrive at the following expression [9]:

$$V_r = V(1 - 0.8C_b + 0.26)\cdot$$
$$\cdot\left(1 + 0.5 + \frac{0.5}{1 + \frac{0.15}{\frac{X}{d}}}\left(\left(1 + 8 \cdot \frac{K_t}{\pi J^2}\right)^{0.5} - 1\right)\right) \quad (16)$$

$$J = \frac{V(1 - 0.8Cb + 0.26)}{N\,d} \quad (17)$$

In order to try to minimise the effects of turbulent flows, it is necessary to achieve a low $V_r$ value. For this a low x/d is recommendable, taking into account the minimum values given by CS which must be fulfilled to avoid problems of vibration.

Tuna vessels however achieve high J values (0.35 to 0.94). For these ranges of J, experimental rudder tests [8, 9] have demonstrated that the value of $C_{ft}/\alpha$ versus the relation X/d increases proportionally ($C_{fd}/\alpha$ decreasing) to X/d = 0.4 (for low values of J the trend is reversed).

Considering tuna vessel characteristics (Table 1), and the previous points, the initial value selected is X/d = 0.22, which complies with the minimum requirements of CS, and would avoid reaching high Re without the penalising lift force.

The flow straightening effect also has to be taken into account [10], influenced greatly by the stern of the vessel, which causes a reduction in water flow speed when reaching the propeller (see Fig. 2). The usual consequence of the straightening effect is to increase the rudder attack angle ($\alpha_e$). Its effect can be measured by using the flow straightening factor ($\gamma$), which relates the ship drift angle, $\beta_R$, with the flow attack angle to the ship axis for zero lift ($\alpha_0$).

$$\gamma = \alpha_0 / \beta_R \quad (18)$$

$$\alpha_e = \alpha - \gamma.\beta_R \quad (19)$$

As can be seen, the value of ($\gamma$) should be as small as possible to widen $\alpha_e$.

The $\gamma$ values obtained during trials, carried out with rudders that protrude vertically [10] in the superior extreme of the propeller diameter, have been high. This leads to the election of the Z/d value that indicates the relative position between the rudder and propeller. According to the trial results, it would be advisable to place the rudder so that it does not protrude beyond the highest blade tip of the propeller (Z/d > 1) to obtain a low flow straightening factor. However, it is recommended that the ratio Z/d < 1 is used in order to guarantee the coverage of the rudder span. As a consequence to the previous points, the ratio Z/d = 1 can also be recommended when considering bending movements and rudder blade height. Finally, the ratio Y/d = 0 obtained from rudder tests [10] has achieved the highest values of $C_{ft}/\alpha$, and the minimum values for $\alpha_0$, and therefore also the minimum values of $\gamma$.

In order to determine value limits for forces on the rudder, it will be necessary to act on its geometry and to understand the consequences of this. For this, a real tuna purse seiner will be used an example (Table 1).

***Tab. 1.*** *Characteristics of the tuna purse seiner "Draco" (Source: Infomarine, May 2006)*

| | |
|---|---|
| L (m) | 95.70 |
| $L_{pp}$ (m) | 82.70 |
| B (m) | 15.20 |
| T (m) | 6.70 |
| M (Tn) | 4 642 |
| V (m/s) | 9 |
| $C_b$ | 0.54 |
| $X_b$ (m) | –2.55 |
| Main engine Power | 6000 kW (750 rpm) |
| Propeller | Controllable 152 rpm (4 blades) |
| Propeller Diameter (m) | 4.3 |

The taper ratio (TR) is the relation between the lower and higher chords. If the value of this coefficient increases, both the lift force and the separation angle of water flow also rise.

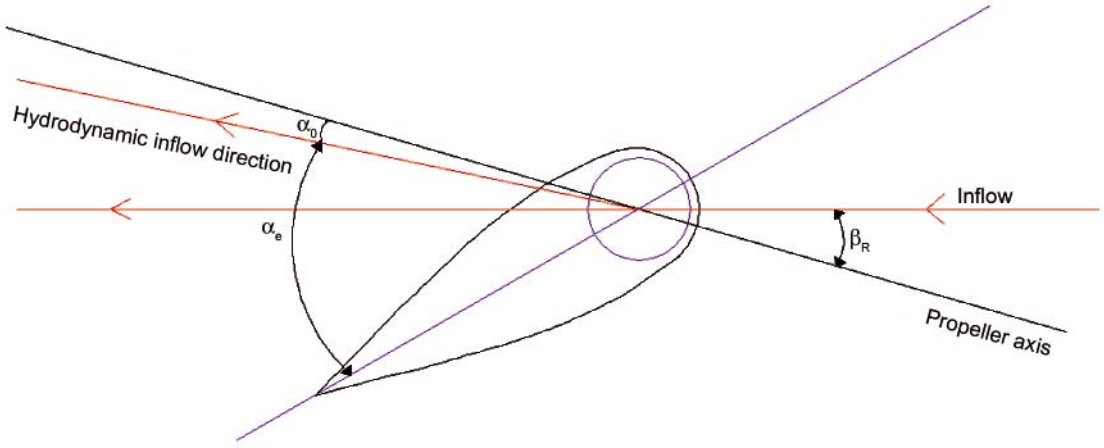


***Fig. 2.*** *Angles of the flow straightening effect*

This also leads to an increase in the bending moment, and the majority of the rudder is adversely affected by the propeller wake. Due to these reasons the ratio TR = 1 has been taken for the calculations.

Another characteristic to be defined is the leading edges of the rudder. a square leading edge shape has been used for high rudder angles, necessary for the operation of tuna vessels; the drag force is less than for rudders with rounded edges.

Finally, a rudder with a flap has been selected due to the quick turning speed and rapid evolution, which makes it ideal for the high manoeuvrability needed by tuna purse seiners. Furthermore, the rudder is going to support minimum vertical forces and bending moments.

### *Calculation of the minimum normal force per rudder angle unit*

This force is calculated bearing in mind the turning circle abilities applicable to the acceptability criteria of Gertler, Eq. (1), to the vessel base (Table 1).

$$D/L < -5C_b + 7.2 = 4.5 \text{ m}$$

Therefore, $D_{max} = 372.15$ m is obtained. With this value, for a turn angle of 35° (0.61 rad), Eq. (2) must be applied. For this, using the vessel base, a minimum normal force value is obtained of:

$$dF_n/d\alpha = 1545.31 \text{ kN/rad}$$

Alternatively, to verify this maximum diameter obtained complies with the IMO requirements regarding turning ability:

$$A_v < 4.5L = 372.15 \text{ m}$$

Now considering expressions (3) – (5) and substituting the values, the result is:

$$D_{max} = 372.15 < 601.76 \text{ m}$$

Therefore, for the minimum value of $F_n/\alpha$ would lead to the turning ability requirements of the IMO being met.

To calculate the minimum lift per angle unit for the correct operation of the vessel, firstly the number P through Eqs. (9) and (10) is analysed. Nevertheless, in order to find the minimum value of lift force by turn angle, it is necessary to define the relations between K' & T' with $F_t/\alpha$. To obtain these relations, expressions (16) and (17) are integrated into the following formulae:

$$T' = \frac{K_i^2 + K_j^2}{0.27 + 0.258(F + 0.38)^{0.39} - 0.5 + \frac{X_b}{L_{pp}}} \cdot \frac{1}{G+1} \quad (20)$$

$$G = 0.0193 \frac{L_{pp}}{B} \frac{1}{C_b^2} \left(1 + \frac{25(T_{pp} + T_{pr})}{L_{pp}}\right) \quad (21)$$

$$F = \frac{\frac{F_t}{\alpha}}{\frac{1}{2} \cdot \rho \cdot V_r^2} \cdot \frac{(1.26 - 0.8C_b)^2}{T} \cdot \cdot \left(\frac{1}{B}\right)\left(\frac{1}{C_b{}^2}\right)\left(1 + \frac{25(T_{pp} - T_{pr})}{L_{pp}}\right) \quad (22)$$

The previous expressions have been empirically obtained from reference [3].

Considering also the values of the vessel base (Table 1) the relations are finally obtained:

$$T' = \frac{0.065}{0.258\left(7.19 \cdot 10^{-6} \frac{F_t}{\alpha} + 0.38\right)^{0.39} - 0.26} \quad (23)$$

$$K' = 3.788 \cdot 10^{-7} \cdot \cdot \frac{\frac{F_t}{\alpha}}{0.258\left(7.19 \cdot 10^{-6} \frac{F_t}{\alpha} + 0.38\right)^{0.39} - 0.22} \quad (24)$$

The P number can be expressed as a function of $F_t/\alpha$. In order to evaluate the lower limit of this value, the functions which make up expression (9) will be analysed:

$$P = (1 - T' + T'e^{-1/T})K' = f_1 \cdot f_2 > 0.275$$

Where:

$$f_1 = 1 - T' + T'e^{-1/T} \quad (25)$$

and:

$$f_2 = K' \quad (26)$$

Function $f_1$ (Fig. 3) is not continuous on T' = 0 and its limits tend infinitely towards 0 and 1.

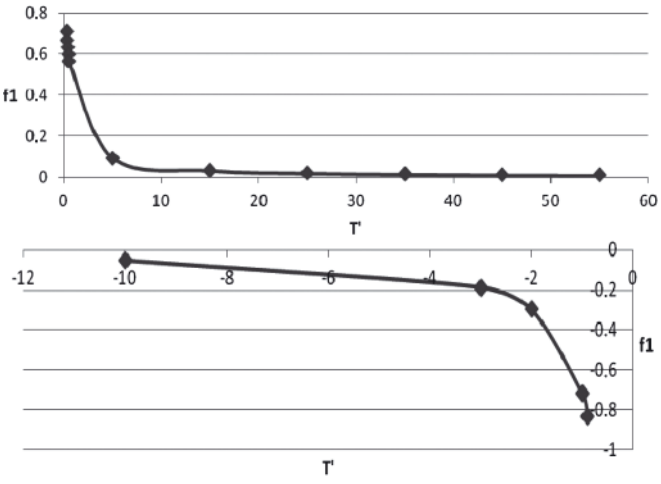


***Fig. 3.*** *Tendency of function $f_1$ of the number P of Norrbin against T'*

If function $f_2$ (Fig. 4) is analysed, which depends on $F_t/\alpha$, it can be seen that a discontinuity in $f_2 = K' = 0$ also exists. The maximum of function $f_2$ is obtained by $F_t/\alpha = 441$ kN/rad.

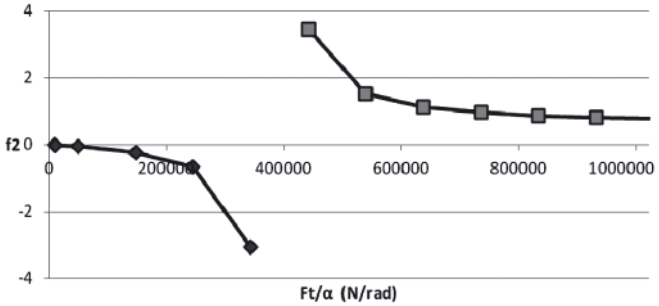


***Fig. 4.*** *Tendency of function $f_2$ of the number P of Norrbin as a function of $F_t/\alpha$*

This value of $F_t/\alpha$ signifies that T' < 0 and, therefore $f_1$ takes negative values. To ensure T' > 0 it will be necessary to use $F_t/\alpha > 838.3$ kN/rad, even though this value does not comply with the requisite given in Eq. (9). For this it is necessary to use expression $F_t/\alpha > 2009$ kN/rad (Fig. 5), which will correspond to the minimum lift force required per unit angle.

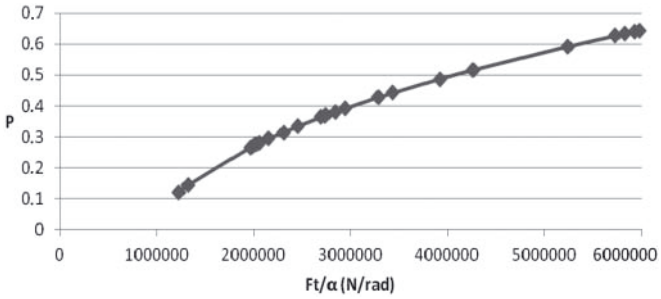


***Fig. 5.*** *Tendency of number P of Norrbin against Ft/α (N/rad)*

Although the increase in the $F_t/\alpha$ value is favourable for complying with expression (9), this increase penalizes the ability to keep course (6). In addition, these high values of $F_t/\alpha$ implicate an enlargement of the servomotor and rudder.

The leeway for the course keeping ability is measured by the width of the hysteresis loop, which only has meaning for positive values. Despite the fact that expression (6) is zero for T' = 2.56 (Fig. 4), for this value expression (9) (P = 0.128, $f_1 = 0.174$ y $f_2 = 0.737$) is not carried out.

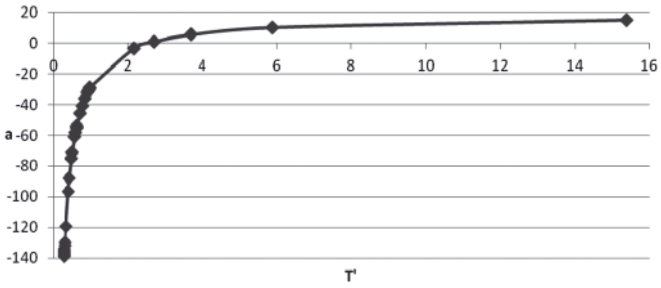


***Fig. 6.*** *Width tendency of the hysteresis loop against T'*

Following the previous results, the minimum lift force per angle turn was assumed by:

$$(F_t/\alpha)_{min} = 2744 \text{ kN/rad}$$

This allows the value to comply with expression (9) without excessive risk to the course keeping ability (6).

### *Calculation of main characteristics*

The fundamental geometric characteristics that identify a rudder are: span (h) defined in the normal flow direction, chord (c) which is the measurement of the rudder blade, thickness (t), perpendicular to the longitudinal axis of the vessel (see Fig. 7). Other parameters are: the profile type (t/c), area of the rudder ($A_r$), defined as the product span by the chord:

$$A_r = h.c \tag{27}$$

and the aspect ratio (λ), which is the relation between the rudder span and the average chord measurement (elongation):

$$\lambda = h/c \tag{28}$$

Firstly, in order to select the rudder characteristics it is necessary to take into account the following points:

- The stern post characteristics (for a relation ratio Z/d ≈ 1) limit the span of the rudder (h) to 6 m.
- In accordance with CS, the minimum area of the rudder blade [5] is limited to $A_r = 8.26$ m² for the vessel base according to:

$$A_r = \frac{TL_{pp}}{100}\left(1 + 50C_b^2\left(\frac{B}{L_{pp}}\right)^2\right) \tag{29}$$

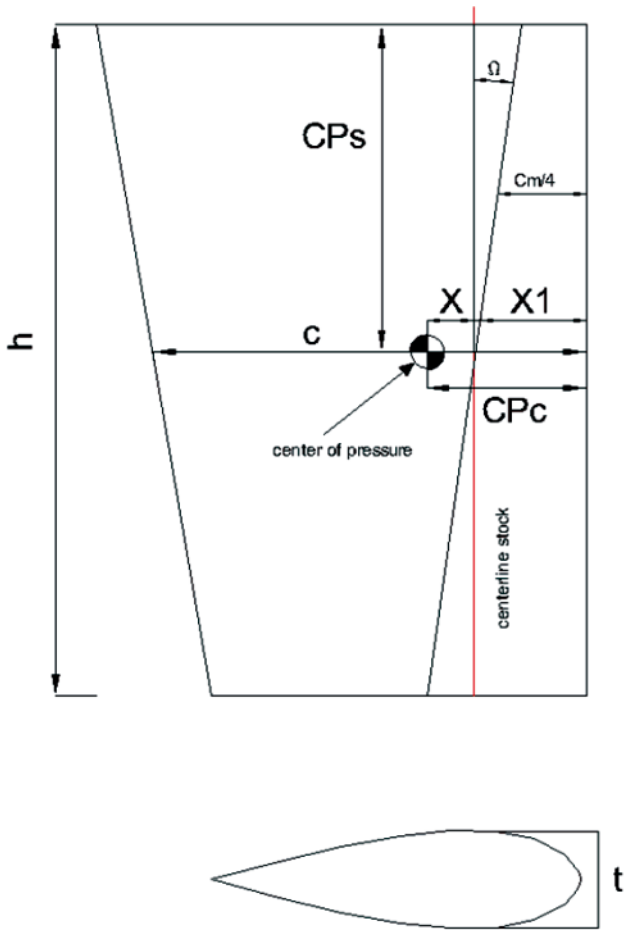


***Fig. 7.*** *Notation of the main parameters in the rudder*

- It is recommended that the elongation ratio (λ) is as high as possible because of the increase in the lift force. However, on the other hand, for flap rudders the chord must be wider. Due to the restriction of the space on tuna vessels, the possible maximum span is 6 m.
- Observing the flow speed on the rudder and the possible chords (16), the Re values are expected to be high. Therefore, as the lift coefficient increases ($C_{ft}$) the drag decreases ($C_d$), and the separation angle ($\alpha_s$) and cavitation risk also increase (see Table 2).
- Finally, note that for equal values of Re, the drag force coefficient ($C_{fd}$) increases when the t/c ratio also rises [11].

$$C_{fd}/\alpha = \frac{F_d/\alpha}{\frac{1}{2}\rho \cdot A_r \cdot V_r^2} \tag{30}$$

Table 2 shows different calculated possibilities of rudders for different Re values (and therefore chords), analysing their respective stall angles. These have been calculated through expressions (17), (27) and (28) integrated into [3]:

$$\alpha_s(\text{degrees}) = 7.11\left(1 + 7\cdot\frac{t}{c}\right)\left(1 + \frac{1.25}{\lambda}\right)\cdot \left(1 + 0.048\left(\ln\left(1 + \frac{8K_t}{\pi J^2}\right)\right)^{0.5}\right)\cdot\frac{h}{d} \tag{31}$$

The previous expression has been obtained from model tests and verified with real fishing vessels up to 6 m of rudder span. In addition to this, for the t/c calculation expressions (8) and (16) have been integrated together with the minimum lift force value obtained in [3]:

$$\frac{C_{ft}}{\alpha} = \frac{\frac{F_t}{\alpha}}{\frac{1}{2} A_r V_r^2} = \frac{2\pi\lambda}{\lambda+2.55}\left(1 - 0.35\frac{t}{c}\right)\cdot \left(1 + K_t \frac{\frac{8}{(\pi J^2)d}}{h}\right)\left(\frac{C_b+0.3}{1+1.214\left(1-e^{-0.3\left(\frac{K_t}{J^2}\right)}\right)}\right) \quad (32)$$

Finally, the expression used is:

$$\frac{t}{c} = \frac{1}{0.35}\left(1 - 12.41\frac{\lambda + 2.55}{h(h+4.52)}\right) \quad (33)$$

***Tab. 2.*** *Rudder geometric characteristics for different Re values with their respective stall angles*

| Re | C (m) | λ | H (m) | t/c | $A_r$ (m²) | $\alpha_s$ (rad) |
|---|---|---|---|---|---|---|
| **3 10⁷** | **3** | 1.85 | 5.55 | 0.07 | 16.65 | 0.39 |
| | | 1.90 | 5.70 | 0.15 | 17.10 | 0.56 |
| | | 1.95 | 5.85 | 0.23 | 17.55 | 0.72 |
| | | **2.00** | **6.00** | **0.30** | **18.00** | **0.88** |
| 2.9 10⁷ | 2.9 | 1.90 | 5.51 | 0.00 | 15.98 | 0.22 |
| | | 1.95 | 5.66 | 0.08 | 16.40 | 0.27 |
| | | 2.00 | 5.80 | 0.16 | 16.82 | 0.43 |
| | | 2.05 | 5.95 | 0.24 | 17.24 | 0.58 |
| | | 2.10 | 6.09 | 0.31 | 17.66 | 0.73 |
| 2.8 10⁷ | 2.8 | 2.00 | 5.60 | 0.01 | 15.68 | 0.28 |
| | | 2.05 | 5.74 | 0.09 | 16.07 | 0.43 |
| | | 2.10 | 5.88 | 0.16 | 16.46 | 0.58 |
| | | 2.15 | 6.02 | 0.23 | 16.86 | 0.72 |

Table 2 shows the valid solutions achieved which meet the maximum span rudder allowed (6 m) with relation t/c remaining positive. The chosen option is that highlighted in Tab. 2. This option is the most interesting for a flap rudder as it has the wider chord (c), a not very high t/c profile relation and the highest stall angle (critical for tuna vessels). This option also complies with the minimum rudder area demanded by CS.

## *Stall angle correction*

The stall angles, indicated previously, have been calculated using empirical expressions obtained in successive tests on tuna vessels of fixed rudders blades with taper ratios different to one. Therefore, one must consider the effect of the rudder with a taper ratio value equal to one in the stall angle calculation. For this, the following expressions (suitable for rudders with a squared blade tip) have been used [9], where the angles shown are expressed in degrees:

$$C_{ft} = \left(1.95\frac{\pi}{57.3\left(1+\frac{3}{\lambda}\right)}\right)\alpha + \frac{C_{dc}}{\lambda}\left(\frac{\alpha}{57.3}\right)^2 \quad (34)$$

$$Cdc = 0.1 + 1.6.\ TR \quad (35)$$

It will be assumed that in the most unfavourable condition ($\alpha = \alpha_s$), the value of ($F_t/\alpha$) will be the minimum obtained in section 2.1. Substituting this value in expression (8) $C_{ft}/\alpha$ is obtained. With this initially assumed value of TR = 1 plus the $C_{ft}/\alpha$ value now acquired, we see that the separating angle is 52.24° or 0.91 rad (a difference of 3.4% with respect to the value calculated through expression (31)).

Being prudent, the most unfavourable separating angle regarding the vessel axis is taken (0.88 rad), therefore it is necessary to adjust expression (35):

$$C_{dc} = 0.1 + 1.62\ TR \quad (36)$$

Because of this, we arrive at a new more conservative expression that defines the law for lift force per unit of flap rudder angle (34), which will be evaluated later.

$$C_{ft}/\alpha = 0.04 + 2.61 \cdot 10^{-4} \cdot \alpha \quad (37)$$

## *Calculation of the rudder forces and profile type*

In this section, the forces per angle turn of the rudder will be evaluated to determine whether the minimum force demanded is achieved (section 2.1). For this, force coefficients will be analysed, of which the normal force is:

$$C_{fn}/\alpha = \frac{\frac{F_n}{\alpha}}{0.5 \cdot \rho \cdot V_r^2 \cdot A_r} \quad (38)$$

Taking into account the value of $(F_t/\alpha)_{min}$ calculated in section 2.1, with α as 0.61 rad (35°) in equation (38) $(C_{fn}/\alpha)_{min}$ can be obtained.

On the other hand, in fishing vessels the transverse components and normal force on the rudder can be connected in the following form [3].

$$F_n = F_t/C \quad (39)$$

Where C is a constant determined empirically, and is defined as:

$$C = 1 - 0.00286\alpha \quad (40)$$

By substituting these two expressions in equation (38), and bearing in mind (37), a new equation is defined, as a function only of turning angle α:

$$\frac{C_{fn}}{\alpha} = \frac{\frac{C_{ft}}{\alpha}}{C} = \frac{0.04 + 2.61 \cdot 10^{-4} \cdot \alpha}{1 - 0.00286\alpha} \quad (41)$$

In this expression, we have already remembered the selected rudder (with flap and taper ratio equal to 1), because expression (37) is used, and it was modified for this particular case.

Although it would be convenient to evaluate expression (37) by comparing it with another expression of lift force coefficient for rudders with flaps [9]:

$$C_y = 2.262\alpha + 0.9453\beta - 0.9329\alpha^2 + - 0.6039\beta^2 + 0.4736\alpha\beta \quad (42)$$

Where β is the angle that forms the flap with the rudder axis. Setting a relation between α and β that, α/β = 1 [4], for 35ş one determines that $C_y$ is 1.91 and $C_{ft}$ is 1.95. That is to say, they achieve similar values; therefore expression (37) can be given as valid.

So for 35° $(F_n/\alpha)_{min}$ = 1545.31 kN/rad (see section 2.1) according to equation (38).

$(C_{fn}/\alpha)_{min}$ = 0.0306

And, alternatively, with respect to equation (41) for 35ş:

$C_{fn}/\alpha$ = 0.054 > $(C_{fn}/\alpha)_{min}$ = 0.0306

Like this, the manoeuvrability requirements are met, in accordance with the normal forces and that of lift required.

To test the rudder evolution at different angles (Fig. 8) expressions (8), (30) and (41) are used. The resistance coefficients for drag and the resulting force can be calculated by:

$$C_{fn} = C_{ft} \cdot \cos\alpha + C_{fd} \cdot \sin\alpha \quad (43)$$

$$\frac{C_{fr}}{\alpha} = \left(\left(\frac{C_{ft}}{\alpha}\right)^2 + \left(\frac{C_{fd}}{\alpha}\right)^2\right)^{0.5} \quad (44)$$

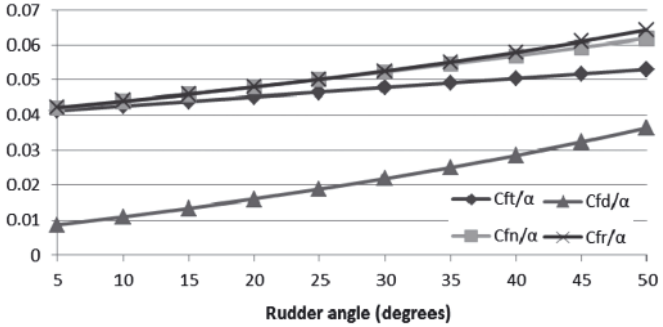


***Fig. 8.*** *Evolution of dimensionless force coefficients on the rudder for different angles*

One can see in Fig. 9 that, for whatever the angle of rudder turn, it complies with P > 0.275.

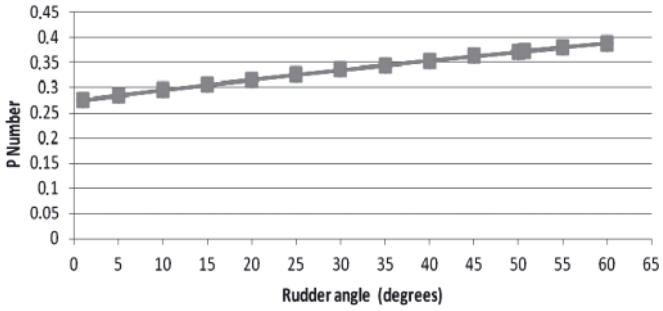


***Fig. 9.*** *Number P of Norrbin for different angles*

The main characteristic that defines the type of profile is the relation t/c (33), as it will affect the minimum resistance and the stall angle. The profile characteristics are those which have greatest influence on cavitation.

For the study of the flap rudder, a symmetrical NACA 0030 profile was used (Table 2). In this profile we shall examine whether cavitation exists in each section, for each angle of action according to expressions (12) and (13).

Firstly, the pressure coefficient ($C_P$) has been obtained from expression (15), taking into account the profile surface perimeter (I), where pressure is expressed as:

$$1 = \int \left(1 + y'(x)^2\right)^{0.5} dx \quad (45)$$

At the same time, the profile thickness referred to as axis "y" is a function of the position (x) considered on the chord (c). Consequently, for the NACA 0030 profile [1], y (x) is a percentage of c:

$$y(x) = \pm \frac{tmax}{0.20} \cdot \cdot \left(\begin{matrix} 0.26690x^{0.5} - 0.12600x + \\ -0.35160x^2 + 0.28430x^3 - 0.10150x^4 \end{matrix}\right) \quad (46)$$

The chord point considered for this study is the pressure centre for each angle of attack of the rudder. The evolution of $C_P$ with angle of turn is shown in Fig. 10.

The cavitation coefficient (σ) was calculated for different angles of attack of the rudder (α), and from different sections of the rudder (Table 3). The calculation of $P_0$ in each one of them (defined by their hg values) has been found by considering the draft (T) and the project trim for the vessel base (see table 1).

***Tab. 3.*** *Cavitation number for different transversal sections of the rudder*

| | Sections | hg (m) | $P_0$ (Pa) | σ |
|---|---|---|---|---|
| **1** | The nearest to the heel pintle | 6.36 | 165161 | 3.17 |
| **2** | Coincident with the lowest propeller tip | 5.99 | 161535 | 3.09 |
| **3** | Coincident with the propeller axis | 3.84 | 139938 | 2.67 |
| **4** | Coincident with the top propeller tip | 1.69 | 118341 | 2.25 |
| **5** | The nearest to the rudder root | 0.66 | 107904 | 2.05 |

For every section considered and the range of rudder angles analysed, the risk of excessive cavitation is not noticeable (Fig. 10), therefore it seems correct to assume the initially selected NACA0030 profile.

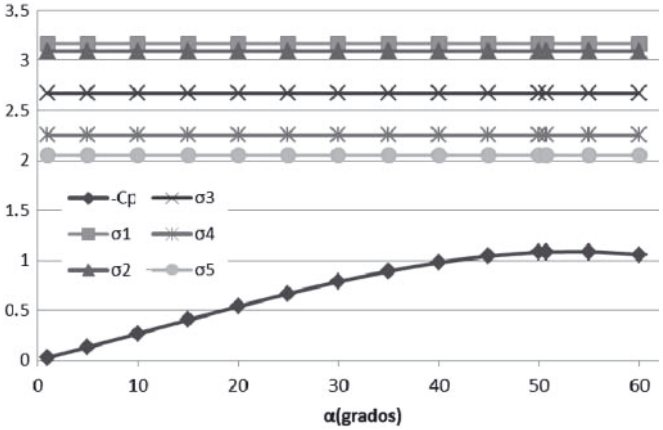


***Fig. 10.*** *Pressure coefficient and cavitation numbers by section for different angles*

## *Selection of rudder balancing*

The compensation ($X_1$) is the relation between the blade surface to the bow axis for turning, and the total surface area. This parameter has a fundamental importance for reducing torque moments and therefore on the stock diameter. Its principal limitation is that the centre of pressure, considering that this moves with the angles of turn, always remains at the stern.

The evolution of the transverse pressure centre position ($CP_c$), measured as a percentage of the chord from the bow (see Fig. 7), for distinct attack angles has been calculated with expressions (36) and (41) together with [9]:

$$CP_c = \left(0.25 - \frac{\frac{C_{mc}}{4}}{C_{fn}}\right) \quad (47)$$

$$\frac{\frac{C_{mc}}{4}}{\alpha} = 0.25 + \quad (48)$$

$$-\left(\left(0.5 - \frac{1.11\left((\lambda^2+4)^{0.5}\right)+2}{4(\lambda+2)}\right) \cdot 1.95 \frac{\pi}{57.3\left(1+\frac{3}{\lambda}\right)}\right) +$$

$$-0.5 \cdot \frac{C_{dc}}{\lambda} \cdot \frac{\alpha}{57.3^2}$$

Substituting the values for the base vessel (Table 1) the following expression is reached (with α in degrees):

$$CP_c = 0.25 - \frac{3 \cdot 10^{-3} - 1.49 \cdot 10^{-4}\alpha}{\frac{0.04 + 2.61 \cdot 10^{-4}\alpha}{1 - 0.00286\alpha}} \quad (49)$$

In addition, the values achieved for TR = 1 (see section 2) should be displaced by 1% to the stern [9] (Fig. 8). The longitudinal centre of pressure is expressed as:

$$CP_s = \left(\frac{0.85}{(5+\lambda)^{0.25}} TR^{0.11}\right) \quad (50)$$

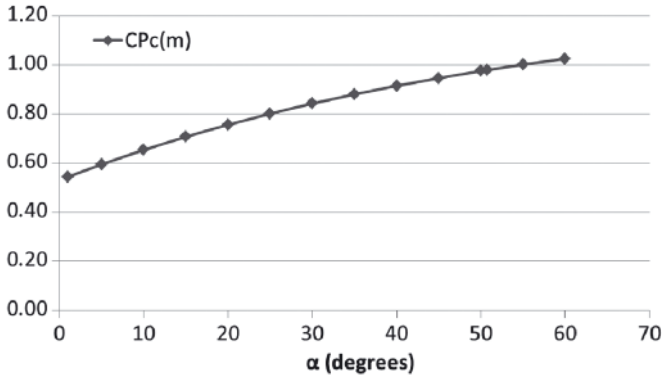


***Fig. 11.*** *Distance from the transverse pressure centre with the rudder angles*

Figure 11 shows that for angles close to zero, the distance from the transverse pressure centre ($CP_c$) is 0.54 m. Therefore, $X_1$ = 0.54 m will be used as this guarantees positive torque moments. The compensation factor for the value of $X_1$ is 18%, and the reduction of torque respective to a compensation of 0% is shown in Fig. 12.

The torque moment supported by the rudder at 35° (the bending moment) exceeds the minimum values demanded by DNV [4] for balanced rudders, as well as the recommendations on maximum compensable area (23%) and the maximum compensable chord (35%).

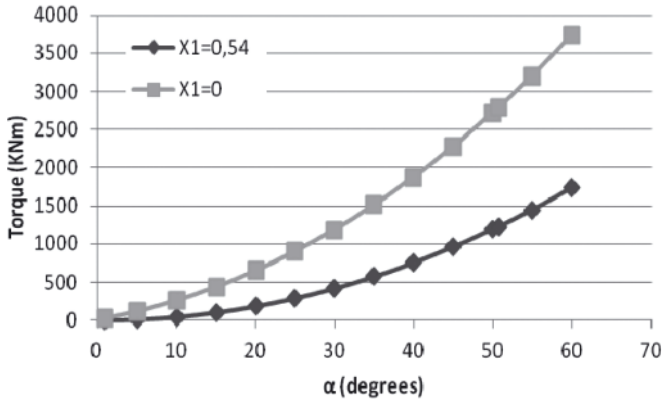


***Fig. 12.*** *Torque moments for zero compensation and of 18% ($X_1$ = 0.54) for different rudder angles*

## *Calculation of the stock diameter*

For this calculation the following equation will be used [4]:

$$d_m = 42\left(1 + \frac{4}{3} \cdot \left(\frac{M_f}{M_t}\right)^2\right)^{\frac{1}{6}} \cdot \left(\frac{M_t}{F1}\right)^{\frac{1}{3}} (mm) \quad (51)$$

This expression requires that the torque moments ($M_t$) are calculated along with the bending moments ($M_f$), for a rudder angle of 35%. For these calculations expressions (50), (47), (38) and (44) are used.

$$M_t = F_n\left((CP_c \cdot c) - X_1\right) \quad (52)$$

$$M_f = F_r(CP_c/7) \quad (53)$$

Finally, the diameter obtained d = 334.46 mm meets to the CS requirements [4].

## *Selection of rudder flap*

From the trials taken on symmetric profiles NACA for the rudders, with a ratio aspect, λ = 2, and Re = 0.125·10⁶ [9], it could be concluded that the lift forces were almost double for rudders with a flap ratio of 0.25, and a relation of flap angle/rudder angle = 2.

A fundamental parameter, that affects the effectiveness of a rudder flap, is the compensation factor. In section 2.5, a compensation of 18% was defined, and for this, according to experimental results mentioned, the greatest relation $C_{ft}/C_{fd}$ is given for the relation flap chord/total chord = 0.4. It is this value that is taken in order to proceed with the calculations.

## RESULTS

As a consequence of the steps indicated in the previous sections, an optimised rudder model, which is actively supported and adapted to the vessel base, has been obtained. This model has a NACA 0030 profile, a flap chord of 40% and squared edges. The rudder characteristics are summarised in Table 4 and its relative position is shown in Fig. 13.

***Tab. 4.*** *Operating and geometric characteristics of the rudder*

| c (m) | λ | h(m) | t/c | x1 | TR | Ω | Re |
|---|---|---|---|---|---|---|---|
| 3 | 2 | 6 | 0.3 | 18% | 1 | 0 | $3 \cdot 10^7$ |

The rudder defined has been designed to comply with the forces per angle unit and moments, which allow the certain existing operational requirements of the regulations to be achieved, as well as those recommended by the experimental test results obtained (section 2).

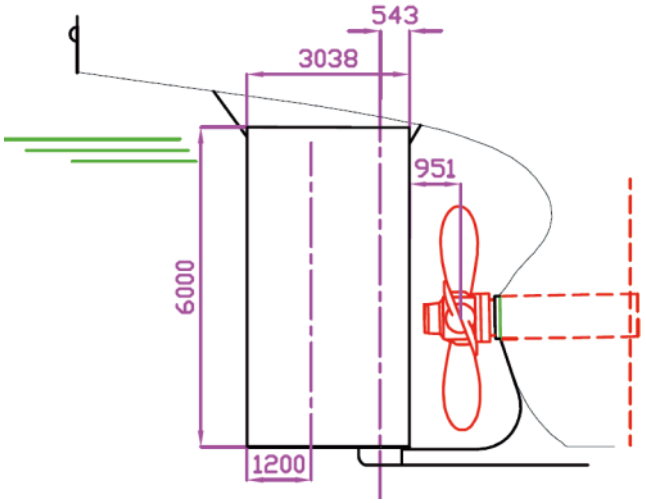


***Fig. 13.*** *Dimensions and relative position of the rudder for tuna purse seiners (mm)*

However, other demands are not guaranteed, such as the SOLAS Chapter II–1, Rule 29 extreme, or the aptitude in order to correct the yaw in respect to OMI Circular MSC.1053. For that it will be necessary to model the rudder defined here in a hydrodynamic design tool, which allows the model used to be optimised with evolutionary algorithms.

## DISCUSSION

- This paper has introduced a method of definition for the principal characteristics of a high–performance rudder and its relative position in the boat, in order to optimise the manoeuvrability of the fishing vessel.
- The method is initiated with the definition of the minimum normal, and lift forces per rudder unit angle, which must be exerted on the rudder to assure the "turning ability", `course keeping´ and "yaw checking". Integrating the results obtained from trials with fishing vessels and rudders have defined expressions that relate the rudder geometry and its relative position in relation to the propeller and said forces.
- Finally, the method is applied to a representative vessel with high manoeuvrability demands: a tuna purse seiner. The results obtained allow not only knowing all the parameters that define the rudder, but also its behaviour in various sections and for different angles. Also, the rudder has been checked for compliance to the Classification Societies' requirements.
- Even though the rudder defined assures certain manoeuvrability conditions in the vessel, other regulative demands must be checked. For that, the model obtained and its respective evolution can be anticipated by the application of evolutionary algorithms which will be tested with CFDs.
- The results acquired for the base vessel show a remarkably high Re value reached at service speed. This, together with the need for manoeuvrability at large rudder angles, leads to a high risk of reaching early separating angles. For this, it is proposed that subsequent simulations of the behaviour of these models consider the `flow straightening´ effect, and that of cavitation along the profile surface where the laws of pressure show lower values than at all other respective points.

**NOMENCLATURE**

$a$ – hysteresis loop width (m)
$A_r$ – rudder area ($m^2$)
$A_v$ – advance (m). The distance travelled by the centre of the vessel in the direction of the original course from the initiation of the turning manoeuvring until that the course has been modified by 90ş
$B$ – breadth (m)
$c$ – average rudder chord (m)
$C$ – empirical coefficient which relates transversal and normal rudder force components
$Cb$ – block coefficient
$Cdc$ – transversal advance resistance coefficient
$C_{fd}$ – dimensionless rudder drag force coefficient
$C_{fn}$ – dimensionless rudder normal force coefficient
$C_{fr}$ – dimensionless resultant force coefficient
$C_{ft}$ – dimensionless lift force coefficient
$C_p$ – dimensionless pressure coefficient
$CP_s$ – vertical distance to pressure centre (m)
$CP_c$ – transversal distance to pressure centre (m)
$C_{mc}/4$ – torque coefficient on the first quarter of the chord
$C_y$ – lift coefficient for flap rudders
$d$ – propeller diameter (m)
$d_m$ – stock diameter (mm)
$D$ – turning circle diameter (m)
$D_t$ – tactical diameter (m)
$D_v$ – course deviation (m)
$F_n$ – normal force to the axial plane of the rudder (N)
$F_t$ – lift force perpendicular to the inflow direction on the rudder (N)
$F_r$ – resulting force (N)
$F1$ – material factor (see DNV rules, Pt.3 Ch.3, Sec.2)
$g$ – gravity (9.8 $m/s^2$)
$h$ – rudder span (m)
$hg$ – distance to the rudder section considered from the floating line (m)
$J$ – propeller advance ratio.
$K', T'$ – coefficients of hydrodynamic absorption
$K_i$ – transversal radius of inertia of the mass of the vessel (in fishing vessels 0.24–0.26)
$K_j$ – inertial radius for the dragged water of the vessel (0.2 for the base vessel [3])
$K_t$ – propeller thrust coefficient (0.18 for the base vessel with 0.55 of blade area ratio and P/D = 1).
$l$ – length of the profile surface where the lift is acting (m)
$L$ – total length of the vessel (m)
$L_{pp}$ – length between perpendiculars (m)
$M$ – displacement of the vessel (T)
$M_t$ – torque moment (Nm)
$M_f$ – root bending moment (Nm)
$N$ – propeller rate of revolutions (rps)
$P$ – Norrbin P number
$P_0$ – free flow pressure (Pa)
$P_{at}$ – atmospheric pressure (Pa). Pat = 101325 Pa.
$P_l$ – local pressure on the sections (Pa)
$P_v$ – local vapour pressure (Pa). $P_v$ = 1706 Pa for an average temperature of the sea 15şC
$Re$ – Reynolds Number
$t$ – rudder section thickness (m)
$T$ – average design draft (m)
$T_{pp}$ – aft draft related to the design draft (m)
$T_{pr}$ – fore draft related to the design draft (m)
$TR$ – taper ratio
$V$ – service speed of the vessel (m/s)
$V_r$ – inflow speed on the rudder (m/s)
$X$ – separation between the fore edge of the rudder and the propeller plane (m)
$X_l$ – rudder compensation (%)
$x$ – point on the chord profile
$X_b$ – longitudinal distance from the midship of the vessel to the centre of buoyancy (m)
$Y$ – distance from the propeller axis to the longitudinal axis of the rudder (m)
$y(x)$ – profile thickness law relative to the chord
$Z$ – distance from the top tip of the propeller blade to the lower tip of the rudder blade (m).

$\alpha$ – angle of attack (rad except where another unit is mentioned)
$\alpha_0$ – angle between the axis vessel and the hydrodynamic inflow direction on the rudder for lift zero (rad except where another unit is mentioned)
$\alpha_e$ – effective rudder angle (rad except where another unit is mentioned)
$\alpha_s$ – stall angle with respect to the vessel axis
$\gamma$ – flow straightening factor
$\rho$ – sea water density $1.025\times10^3$ ($Kg/m^3$)
$\nu$ – kinematic viscosity of water ($10^6$ $m^2/s$ for an average temperature of the sea of 20şC and normal atmospheric conditions)
$\beta$ – rudder turning angle. The angle that forms the flap with the rudder axis.
$\beta_R$ – drift angle
$\lambda$ – aspect ratio
$\sigma$ – cavitation number

## BIBLIOGRAPHY


1. Abbott I, Von Doenhoff A.: *Theory of wing sections*. McGraw–Hill, Dover, 1959.
2. Baquero A.: *Experimentación en el campo de la hidrodinámica del buque: Ensayos de maniobrabilidad*, Publicación No. 64, El Pardo Model Basin. Ministerio de Defensa, Madrid, 1980.
3. Baquero A.: *La maniobrabilidad del buque pesquero*, Publicación No. 123, El Pardo Model Basin. Ministerio de Defensa, Madrid, 1987.
4. Det Norske Veritas (DNV): *Hull equipment and safety rules for classification of ships*, Part 3, Chapter 3. 2007.
5. International Maritime Organization (IMO): *Explanatory notes to the standards for ship maneuverability*, MSC/Circ.1053. 2002.
6. International Maritime Organization (IMO): *Standards for ship maneuverability*, Resolution MSC.137(76). 2002
7. International Maritime Organization (IMO): *International convention for the safety of life at sea*: SOLAS, 4th edition. 2002.
8. Molland A, Turnock S.: *Flow straightening effects on a ship rudder due to upstream propeller and hull*. International Shipbuilding Progress, 49(3) (2002) 195–214.
9. Molland AF, Turnock SR.: *Marine rudders and control surfaces*. Elsevier, Oxford, 2007.
10. Nobukawa T, Tushto K, Metomura K, Yoshimura Y.: *Studies on manoeuvrability standards from the viewpoint of marine pilots. International Conference on Marine Simulation and Ship Manoeuvrability* (Marsim & ICSM 90), Tokyo, Japan, June 4–7, 1990.
11. Pérez F, Zamora R.: *Influencia de los parámetros generales del buque en sus características de maniobrabilidad*. II Congreso Internacional de Ingeniería Oceánica (Océano 2000), Valdivia, Chile, October 25–27, 2000.


---

## CONTACT WITH THE AUTHORS


Alba Martínez–López – Ph.D. Marine Engineering
amartinezl@udc.es
Alicia Munín–Doce – Marine Engineering
a.munin@udc.es
Integrated Group of Engineering Research
Department of Naval Engineering, University of a Coruńa (Spain)
c/ Mendizabal s/n, Escola Politécnica Superior de Ferrol, Campus de Esteiro, Ferrol (A Coruńa)
CP: 15403 (Spain)

**POLISH MARITIME RESEARCH** 3(75) 2012 Vol 19; pp. 36-44
10.2478/v10012-012-0029-z

# Effect of the working liquid compressibility on the picture of volumetric and mechanical losses in a high pressure displacement pump used in a hydrostatic drive

## Part II

## Mechanical losses in a pump

**Zygmunt Paszota**, Prof.
Gdansk University of Technology, POLAND

ABSTRACT

*Working liquid compressibility may considerably change the values and proportions of coefficients of the volumetric and mechanical energy losses in the displacement pump used in a hydrostatic drive system. This effect can be particularly seen in the operation under high pressure and also in the system, where aeration of the working liquid can occur. In the Part II the mathematical model is presented of the torque of mechanical losses in the pump and its laboratory verification. Conclusions are drawn regarding the effect of working liquid compressibility on the mechanical and volumetric losses in the pump.*

**Keywords**: hydrostatic drive system; pressure displacement pump; energy losses; energy efficiency; energy saving; liquid compressibility; Sankey diagram

## 8. MODEL OF THE MECHANICAL LOSSES IN THE PUMP „WORKING CHAMBERS - SHAFT" ASSEMBLY

The pump shaft torque $M_P$ (required by the pump of its driving motor) must be greater than the torque $M_{Pi}$ indicated in the pump working chambers because of the necessity of balancing also the torque $M_{Pm}$ of mechanical losses in the „working chambers - shaft" assembly. The assembly forms the working chambers and changes their capacity and also connects the working chambers with the shaft. Therefore, the torque $M_P$ required on the pump shaft is a sum of the torque $M_{Pi}$ indicated in the working chambers and the torque $M_{Pm}$ of mechanical losses in the pump „working chambers - shaft" assembly [19]:

$$M_P = M_{Pi} + M_{Pm} \tag{8.1}$$

Torque $M_{Pm}$ of mechanical losses in the pump with variable capacity $q_{Pgv}$ per one shaft revolution is, at the maximum value of $q_{Pgv}$ i.e. $q_{Pgv} = q_{Pt}$ (with $b_P = q_{Pgv}/q_{Pt} = 1$), equal to the torque of mechanical losses in that pump working as a pump with constant capacity $q_{Pt}$ per one shaft revolution. The theoretical and mathematical models describing the torque $M_{Pm}$ of mechanical losses in the pump with variable capacity $q_{Pgv}$ per one shaft revolution may be based on models of $M_{Pm}$ describing the torque of mechanical losses in the pump with constant capacity $q_{Pt}$ per one shaft revolution (with $b_P = 1$). Considering the models describing the torque of pump mechanical losses, we assume, that, in the hydrostatic transmission, pump is driven with practically constant rotation speed $n_P$, and the decrease of shaft speed (decrease of the pump driving motor speed as a result of the increase of torque $M_P$ loading the motor shaft) to a value $n_P < n_{P0}$ ($n_{P0}$ – rotational speed of unloaded pump driving motor) is negligible from the point of view of the impact of speed $n_P$ on the value of torque $M_{Pm}$ of mechanical losses.

**Torque $M_{Pm}$ of mechanical losses in the pump is mainly an effect of friction forces between elements of the „working chambers - shaft" assembly, depending, among others, on the torque $M_{Pi}$ indicated in the working chambers – $M_{Pi} = q_{Pgv}\,\Delta p_{Pi}/2\Pi = b_P\, q_{Pt}\,\Delta p_{Pi}/2\Pi$.**

**Friction forces between elements of the „working chambers - shaft" assembly are, to some extent, also an effect of the load on those elements of the inertia forces from rotational and reciprocating motion and depend on the pump capacity $q_{Pgv}$ per one shaft revolution ($b_P$ coefficient).**

**Particularly, in piston (axial or radial) pumps with casing (crankcase) filled with liquid, friction forces also occur between elements of the „working chambers - shaft" assembly and the liquid and depend on the liquid viscosity $\nu$.**

The value of torque $M_{Pm|\Delta p_{Pi}, b_P, \nu_n}$ of mechanical losses in the pump „working chambers - shaft" assembly, loaded with indicated increase $\Delta p_{Pi}$ of pressure in the working chambers, in the pump operating at the capacity $q_{Pgv} = b_p\, q_{Pt}$ per one shaft revolution and discharging the working liquid with (constant)

reference viscosity $\nu_n$, can be described as a sum of torque $M_{Pm|\Delta p_{Pi}=0, b_P, \nu_n}$ of mechanical losses in the unloaded pump (torque of the losses when the indicated increase $\Delta p_{Pi}$ of pressure in the pump working chambers is equal to zero – $\Delta p_{Pi} = 0$) and increase $\Delta M_{Pm|\Delta p_{Pi}, b_P, \nu_n}$ of torque of mechanical losses, the increase being an effect of loading the assembly structure elements with torque $M_{Pi}$ indicated in the pump working chambers (torque $M_{Pi}$ appearing when the indicated increase $\Delta p_{Pi}$ of pressure in the pump working chambers is greater than zero – $\Delta p_{Pi} > 0$):

$$M_{Pm|\Delta p_{Pi}, b_P, \nu_n} = M_{Pm|\Delta p_{Pi}=0, b_P, \nu_n} + \Delta M_{Pm|\Delta p_{Pi}, b_P, \nu_n} \quad (8.2)$$

Torque $M_{Pi}$ indicated in the pump working chambers is proportional to the increase $\Delta p_{Pi}$ of pressure in the chambers and to the active volume of the chambers created during one pump shaft revolution, which is equal to the theoretical capacity $q_{Pt}$ ($V_P$) per one shaft revolution in a pump with constant capacity per one shaft revolution or to the geometrical capacity $q_{Pgv} = b_P\, q_{Pt}$ per one shaft revolution in a pump with variable capacity per one shaft revolution.

Therefore, the „working chambers - shaft" assembly structure elements are loaded:

– in a pump with theoretical (constant) capacity $q_{Pt}$ per one shaft revolution – with indicated torque:

$$M_{Pi} = \frac{q_{Pt}\Delta p_{Pi}}{2\Pi}$$

– in a pump with geometrical (variable) capacity $q_{Pgv}$ per one shaft revolution – with indicated torque:

$$M_{Pi} = \frac{q_{Pgv}\Delta p_{Pi}}{2\Pi} = \frac{b_P q_{Pt}\Delta p_{Pi}}{2\Pi}$$

which, in effect, causes a differentiated intensity of the increase $\Delta M_{Pm|\Delta p_{Pi}, b_P, \nu_n}$ of the torque of mechanical losses, determined, with different values of coefficient $b_P = q_{Pgv}/q_{Pt}$, as a function of the increase $\Delta p_{Pi}$ of pressure in the pump working chambers.

In the theoretical and mathematical models describing the torque $M_{Pm|\Delta p_{Pj}, b_P, \nu_n}$ of mechanical losses a hypothesis is assumed, that the **increase $\Delta M_{Pm|\Delta p_{Pi}, b_P, \nu_n}$ of the torque of mechanical losses in the pump is proportional to the torque $M_{Pi}$ indicated in its working chambers**.

**The impact of inertia forces of the „working chambers - shaft" assembly elements, performing the rotational and reciprocating motion in the pump, on the torque $M_{Pm}$ of mechanical losses can be presented, under the assumption that rotational speed $n_P$ of the pump driving motor changes only in a small range, as a function of capacity $q_{Pgv}$ ($b_P$ coefficient) per one shaft revolution of a variable capacity pump. Inertia forces do not depend on the value of increase $\Delta p_{Pi}$ of pressure in the working chambers, therefore their impact on the torque $M_{Pm}$ of mechanical losses in the pump may be included in the evaluation of the torque $M_{Pm|\Delta p_{Pi}=0, b_P, \nu_n}$ of mechanical losses determined at the increase $\Delta p_{Pi} = 0$.**

**The impact of the friction forces between the „working chambers - shaft" assembly elements and the liquid on the torque $M_{Pm}$ of mechanical losses in the pump can be presented, under the assumption that speed $n_P$ changes in a small range, as a relation of $M_{Pm}$ to the viscosity ν and to the capacity $q_{Pgv}$ ($b_P$ coefficient) per one shaft revolution** (Fig. 8.1).

It is assumed, that the **impact of liquid viscosity ν on the friction forces between the „working chambers - shaft" elements and the liquid in the piston pump casing (crankcase), and in effect on the torque $M_{Pm}$ of mechanical losses in the pump, can be evaluated** at one level of the increase $\Delta p_{Pi}$ of pressure indicated in the working chambers, e.g. **at the increase $\Delta p_{Pi} = 0$**. This assumption is connected with a simplification assuming that there is no significant impact of the increase $\Delta p_{Pi}$ of pressure on the liquid viscosity ν and with assuming in the model describing the torque $M_{Pm}$ of mechanical losses the liquid viscosity ν determined in the pump inlet conduit (at pressure $p_{P1}$ equal to zero (at liquid absolute pressure equal to atmospheric pressure)).

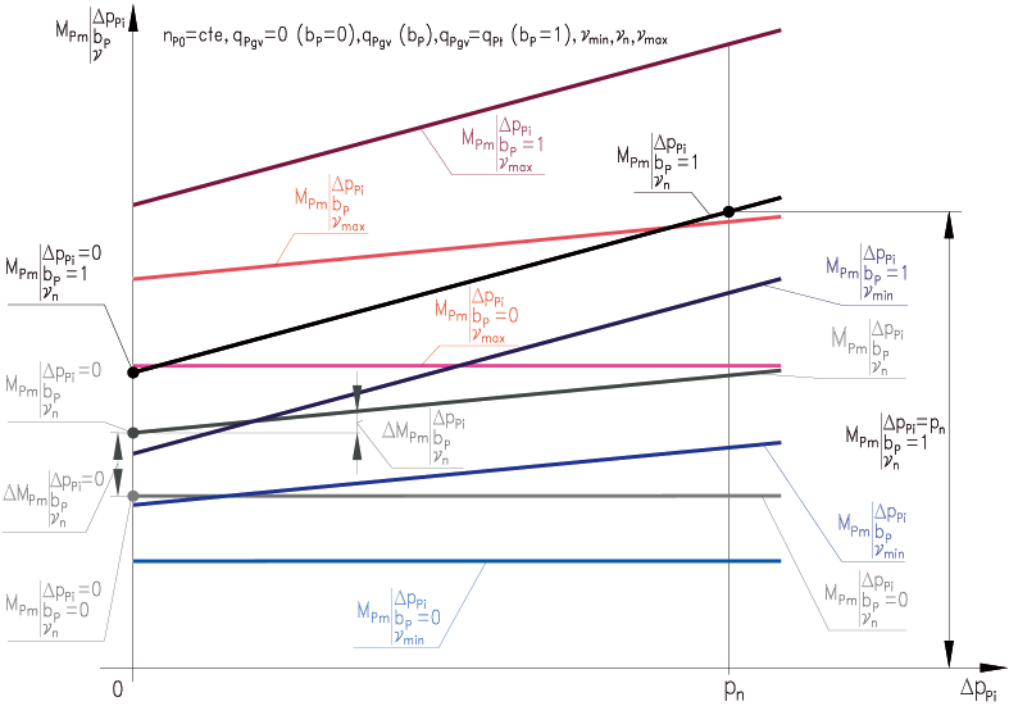


***Fig. 8.1.*** *Torque $M_{Pm|\Delta p_{Pi}, b_P, \nu}$ of mechanical losses in a pump (especially in a piston (axial or radial) pump with crankcase filled with liquid) and with variable capacity $q_{Pgv} = b_P q_{Pt}$ per one shaft revolution, as a function of the indicated increase $\Delta p_{Pi}$ of pressure in the pump working chambers – graphical interpretation of theoretical model (9); capacity $q_{Pgv}$ per one shaft revolution (coefficient $b_P$ of pump capacity): $q_{Pgv} = 0$ ($b_P = 0$), $q_{Pgv}$ ($b_P$), $q_{Pgv} = q_{Pt}$ ($b_P = 1$); liquid viscosity $\nu_{min}$, $\nu_n$ and $\nu_{max}$*

The impact of inertia forces of structure elements performing the rotational or reciprocating motion in the pump and also the impact of liquid viscosity ν on the torque $M_{Pm}$ of mechanical losses in the pump is then described in the model of the torque $M_{Pm|\Delta p_{Pi}=0,\, b_P,\, \nu}$ of those losses in an unloaded pump (at $\Delta p_{Pi} = 0$) supplied with working liquid of changing viscosity ν.

The proposed **theoretical models, describing the torque $M_{Pm|\Delta p_{Pi}=0,\, b_P,\, \nu}$ of mechanical losses in an unloaded pump (at the indicated increase $\Delta p_{Pi} = 0$ of pressure in the working chambers) and at changing working liquid viscosity ν,** have the form:

- in the pump with theoretical (constant) capacity $q_{Pt}$ ($b_P = 1$) per one shaft revolution:

$$M_{Pm|\Delta p_{Pi}=0,\, b_P=1,\, \nu} = M_{Pm|\Delta p_{Pi}=0,\, b_P=1,\, \nu_n}\left(\frac{\nu}{\nu_n}\right)^{a_{vm}} \tag{8.3}$$

- in the pump with geometrical (variable) capacity $q_{Pgv}$ ($q_{Pgv} = b_P\, q_{Pt}$) per one shaft revolution:

$$M_{Pm|\Delta p_{Pi}=0,\, b_P,\, \nu} = \left(M_{Pm|\Delta p_{Pi}=0,\, b_P=0,\, \nu_n} + \Delta M_{Pm|\Delta p_{Pi}=0,\, b_P,\, \nu_n}\right)\left(\frac{\nu}{\nu_n}\right)^{a_{vm}} \tag{8.4}$$

where:

$$\Delta M_{Pm|\Delta p_{Pi}=0,\, b_P,\, \nu_n} = M_{Pm|\Delta p_{Pi}=0,\, b_P,\, \nu_n} - M_{Pm|\Delta p_{Pi}=0,\, b_P=0,\, \nu_n} = \left(M_{Pm|\Delta p_{Pi}=0,\, b_P=1,\, \nu_n} - M_{Pm|\Delta p_{Pi}=0,\, b_P=0,\, \nu_n}\right) b_P \tag{8.5}$$

**Exponent $a_{vm}$** in expressions (8.3) and (8.4) **describes the impact of the ratio $\nu/\nu_n$ of working liquid ν to reference viscosity $\nu_n = 35 mm^2 s^{-1}$ on the value of torque of mechanical losses especially in a piston displacement machine with liquid filling the casing (crankcase)** (in the pump and in the hydraulic motor).

**The increase $\Delta M_{Pm|\Delta p_{Pi},\, b_P,\, \nu}$ of the torque of mechanical losses in the pump, due to the load of the assembly elements with the indicated torque $M_{Pi}$ resulting from the indicated increase $\Delta p_{Pi}$ of pressure in the pump working chambers, is independent of the inertia forces of elements performing the rotational or reciprocating motion in the pump. It is also practically independent of the working liquid viscosity ν; therefore, it may be determined at one viscosity value, e.g. at the liquid reference viscosity $\nu_n$** (Fig. 8.1).

**In the mathematical models describing the torque $M_{Pm}$ of mechanical losses in the pump, coefficients $k_i$ of losses are used relating (comparing) the components describing the torque $M_{Pm}$ of losses in theoretical models to the pump theoretical torque $M_{Pt}$.** The pump theoretical torque $M_{Pt}$ is also a reference value used in the description of the torque $M_{Pi}$ indicated in the pump working chambers:

– theoretical torque:

$$M_{Pt} = \frac{q_{Pt}\, p_n}{2\Pi}$$

of the pump, with theoretical (constant) capacity $q_{Pt}$ per one shaft revolution ($b_P = 1$), is determined with the increase $\Delta p_P$ of pressure in the pump equal to the system nominal pressure $p_n - \Delta p_P = p_n$, and with the assumption that there are no pressure and mechanical losses in the pump,

– indicated torque:

$$M_{Pi} = \frac{q_{Pt}\, \Delta p_{Pi}}{2\Pi} = \frac{q_{Pt}\, p_n}{2\Pi}\,\frac{\Delta p_{Pi}}{p_n} = M_{Pt}\,\frac{\Delta p_{Pi}}{p_n}$$

in working chambers of the pump with theoretical (constant) capacity $q_{Pt}$ per one shaft revolution ($b_P = 1$) is determined with the indicated increase $\Delta p_{Pi}$ of pressure in the working chambers,

– indicated torque:

$$M_{Pi} = \frac{q_{Pgv}\, \Delta p_{Pi}}{2\Pi} = \frac{b_P q_{Pt}\, \Delta p_{Pi}}{2\Pi} = \frac{q_{Pt}\, p_n}{2\Pi}\, b_P\, \frac{\Delta p_{Pi}}{p_n} = M_{Pt}\, b_P\, \frac{\Delta p_{Pi}}{p_n}$$

in working chambers of the pump with geometrical (variable) capacity $q_{Pgv} = b_P\, q_{Pt}$ per one shaft revolution is determined with the indicated increase $\Delta p_{Pi}$ of pressure in the working chambers.

The theoretical and mathematical models describe the torque $M_{Pm}$ of mechanical losses in the pump with theoretical (constant) capacity $q_{Pt}$ per one shaft revolution or with geometrical (variable) capacity $q_{Pgv} = b_P\, q_{Pt}$ per one shaft revolution:

– $q_{Pt} = q_{P|\Delta p_{Pi}=0,\, p_{P1i}=0,\, b_P=1,\, \nu_n}$ is theoretical capacity per one shaft revolution of the pump with constant capacity per one revolution ($b_P = 1$) determined at $\Delta p_{Pi} = 0$, $p_{P1i} = 0$ and $\nu_n$, which is equal to the working volume of the working chambers created during one shaft revolution,

– $q_{Pgv} = b_P\, q_{Pt}$ is geometrical capacity per one shaft revolution of the pump with variable capacity per one revolution at $\Delta p_{Pi} = 0$, $p_{P1i} = 0$ and $\nu_n$, which is equal to the working volume of the working chambers created during one shaft revolution. Capacity $q_{Pgv}$ per one shaft revolution changes in the $0 \le q_{Pgv} \le q_{Pt}$ range and coefficient $b_P = q_{Pgv}/q_{Pt}$ of the pump capacity changes in the $0 \le b_P \le 1$ range.

The proposed **mathematical models describing the torque $M_{Pm}$ of mechanical losses in the pump, related to theoretical models of the torque of mechanical losses**, take the form:

- in a pump with theoretical (constant) capacity $q_{Pt}$ per one shaft revolution ($b_P = 1$):

$$M_{Pm|\Delta p_{Pi},\, \nu} = k_{4.1}\, M_{Pt}\left(\frac{\nu}{\nu_n}\right)^{a_{vm}} + k_{4.2} M_{Pt}\,\frac{\Delta p_{Pi}}{p_n} = \left[k_{4.1}\left(\frac{\nu}{\nu_n}\right)^{a_{vm}} + k_{4.2}\,\frac{\Delta p_{Pi}}{p_n}\right] M_{Pt} = \left[k_{4.1}\left(\frac{\nu}{\nu_n}\right)^{a_{vm}} + k_{4.2}\,\frac{\Delta p_{Pi}}{p_n}\right]\frac{q_{Pt}\, p_n}{2\Pi} \tag{8.6}$$

where:

$$k_{4.1} = \frac{M_{Pm|\Delta p_{Pi}=0,\, b_P=1,\, \nu_n}}{M_{Pt}} = \frac{M_{Pm|\Delta p_{Pi}=0,\, b_P=1,\, \nu_n}}{\dfrac{q_{Pt}\, p_n}{2\Pi}} \tag{8.7}$$

$$k_{4.2}=\frac{\Delta M_{Pm|\Delta p_{Pi},b_P=1,\nu_n}}{M_{Pi}}=\frac{\Delta M_{Pm|\Delta p_{Pi},b_P=1,\nu_n}}{\frac{q_{Pt}\Delta p_{Pi}}{2\Pi}}=$$
$$=\frac{M_{Pm|\Delta p_{Pi},\,b_P=1,\nu_n}-M_{Pm|\Delta p_{Pi}=0,b_P=1,\nu_n}}{\frac{q_{Pt}\Delta p_{Pi}}{2\Pi}}=$$
$$=\frac{M_{Pm|\Delta p_{Pi}=p_n,b_P=1,\nu_n}-M_{Pm|\Delta p_{Pi}=0,b_P=1,\nu_n}}{\frac{q_{Pt}p_n}{2\Pi}}= \tag{8.8}$$
$$=\frac{M_{Pm|\Delta p_{Pi}=p_n,b_P=1,\nu_n}-M_{Pm|\Delta p_{Pi}=0,b_P=1,\nu_n}}{M_{Pt}}$$

- in a pump with geometrical (variable) capacity $q_{Pgv}$ ($q_{Pgv} = b_P\, q_{Pt}$) per one shaft revolution):

$$M_{Pm|\Delta p_{Pi},b_P,\nu}=(k_{4.1.1}+k_{4.1.2}\,b_P)M_{Pt}\left(\frac{\nu}{\nu_n}\right)^{a_{vm}}+$$
$$+k_{4.2}M_{Pt}b_P\frac{\Delta p_{Pi}}{p_n}= \tag{8.9}$$
$$=\left[(k_{4.1.1}+k_{4.1.2}\,b_P)\left(\frac{\nu}{\nu_n}\right)^{a_{vm}}+k_{4.2}\,b_P\frac{\Delta p_{Pi}}{p_n}\right]M_{Pt}=$$

where:

$$=\left[(k_{4.1.1}+k_{4.1.2}\,b_P)\left(\frac{\nu}{\nu_n}\right)^{a_{vm}}+k_{4.2}\,b_P\frac{\Delta p_{Pi}}{p_n}\right]\frac{q_{Pt}p_n}{2\Pi}$$

$$k_{4.1.1}=\frac{M_{Pm|\Delta p_{Pi}=0,\,b_P=0,\,\nu_n}}{M_{Pt}}=\frac{M_{Pm|\Delta p_{Pi}=0,\,b_P=0,\,\nu_n}}{\frac{q_{Pt}p_n}{2\Pi}} \tag{8.10}$$

$$k_{4.1.2}=\frac{M_{Pm|\Delta p_{Pi}=0,b_P=1,\,\nu_n}-M_{Pm|\Delta p_{Pi}=0,\,b_P=0,\nu_n}}{M_{Pt}}=$$
$$=\frac{M_{Pm|\Delta p_{Pi}=0,b_P=1,\,\nu_n}-M_{Pm|\Delta p_{Pi}=0,\,b_P=0,\nu_n}}{\frac{q_{Pt}p_n}{2\Pi}} \tag{8.11}$$

$$k_{4.2}=\frac{\Delta M_{Pm|\Delta p_{Pi},b_P,\nu_n}}{M_{Pi}}=\frac{\Delta M_{Pm|\Delta p_{Pi},b_P,\nu_n}}{\frac{b_P\,q_{Pt}\Delta p_{Pi}}{2\Pi}}=$$
$$=\frac{\Delta M_{Pm|\Delta p_{Pi},b_P=1,\nu_n}}{\frac{q_{Pt}\Delta p_{Pi}}{2\Pi}}= \tag{8.12}$$
$$=\frac{M_{Pm|\Delta p_{Pi}=p_n,b_P=1,\nu_n}-M_{Pm|\Delta p_{Pi}=0,b_P=1,\nu_n}}{\frac{q_{Pt}p_n}{2\Pi}}=$$
$$=\frac{M_{Pm|\Delta p_{Pi}=p_n,b_P=1,\nu_n}-M_{Pm|\Delta p_{Pi}=0,b_P=1,\nu_n}}{M_{Pt}}$$

**Commentary**:

- The sum ($k_{4.1.1} + k_{4.1.2}$) of coefficients used in mathematical model (8.9) describing the torque $M_{Pm}$ of mechanical losses in the pump with geometrical (variable) capacity $q_{Pgv}$ ($q_{Pgv} = b_P\, q_{Pt}$) per one shaft revolution is equal to coefficient $k_{4.1}$ used in the mathematical model (8.6) describing the torque $M_{Pm}$ of mechanical losses in that pump working as a pump with theoretical (constant) capacity per one shaft revolution: $k_{4.1.1} + k_{4.1.2} = k_{4.1}$.
- Coefficient $k_{4.2}$ used in mathematical model (8.9) describing the torque $M_{Pm}$ of mechanical losses in the pump with geometrical (variable) capacity $q_{Pgv}$ ($q_{Pgv} = b_P\, q_{Pt}$) per one shaft revolution is equal to coefficient $k_{4.2}$ used in the mathematical model (8.6) describing the torque $M_{Pm}$ of mechanical losses in that pump working as a pump with theoretical (constant) capacity $q_{Pt}$ per one shaft revolution.

## 9. RESULTS OF INVESTIGATION OF THE TORQUE $M_{PM}$ OF MECHANICAL LOSSES IN THE MEDIUM PRESSURE AXIAL PISTON VARIABLE CAPACITY PT0Z2-25 TYPE PUMP USED IN A HYDROSTATIC TRANSMISSION SYSTEM

Michał Czyński [21] performed the investigation of the PT0Z2-25 medium pressure pump as laboratory verification of the mathematical model of the hydrostatic transmission energy efficiency. The pump was loaded by a hydraulic motor and not by an overflow valve (as it was in the case of the investigation of the high pressure axial piston HYDROMATIK A7V.58. DR.1.R.P.F.00 type pump). The threat of the hydraulic oil aeration was smaller. The system operated under the nominal pressure $p_n$ = 16MPa, half of the value of pressure used in the investigation of the A7V.58.DR.1.R.P.F.00 pump.

The investigation lasted relatively short time, the hydraulic oil tank was large in relation to the pump power. Therefore, the effect of oil aeration and of its compressibility was minimized.

The torque $M_{Pm}$ of mechanical losses in the „working chambers - shaft" assembly of the pump is determined from the measurement of the shaft torque $M_P$ and the torque $M_{Pi}$ indicated in the working chambers. Direct measurement of the torque $M_{Pi}$ is not possible. Therefore, it is necessary to determine the torque $M_{Pm}$ of mechanical losses by an indirect method from the formula:

$$M_{Pm}=M_P-M_{Pi}=M_P-\frac{q_{Pgv}\,\Delta p_{Pi}}{2\Pi}=$$
$$=M_P-\frac{b_P\,q_{Pt}\,\Delta p_{Pi}}{2\Pi} \tag{9.1}$$

Fig. 9.1 presents results of the investigation of the torque $M_P$ on the pump shaft as a function of the indicated increase $\Delta p_{Pi}$ of pressure in the working chambers for different values of the coefficient $b_P$ of the pump capacity $q_{Pgv} = b_P\, q_{Pt}$ per one pump revolution. The investigation results show a very high (close to 1) value of the determination coefficient $R^2$.

Fig. 9.2 and 9.3 present the calculated values of the torque $M_{Pi}$ indicated in the pump working chambers and the torque $M_{Pm}$ of mechanical losses in the pump „working chambers - shaft" assembly.

Fig. 9.4 presents the torque $M_{Pm|\Delta p_{Pi}=0,\,b_P,\,\nu_n}$ of mechanical losses in the unloaded pump as a function of the pump capacity coefficient $b_P$.

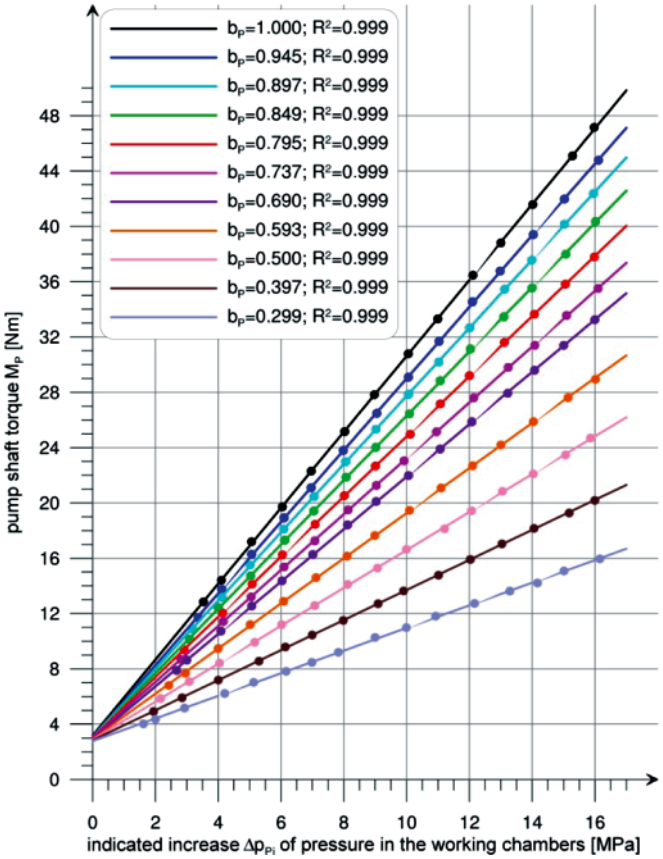


***Fig. 9.1.*** *Torque $M_p$ on the PTOZ2-25 pump shaft as a function of the indicated increase $\Delta p_{Pi}$ of pressure in the working chambers, for different values of the pump capacity coefficient $b_p$, at $v_n$ working liquid viscosity [ 21]*

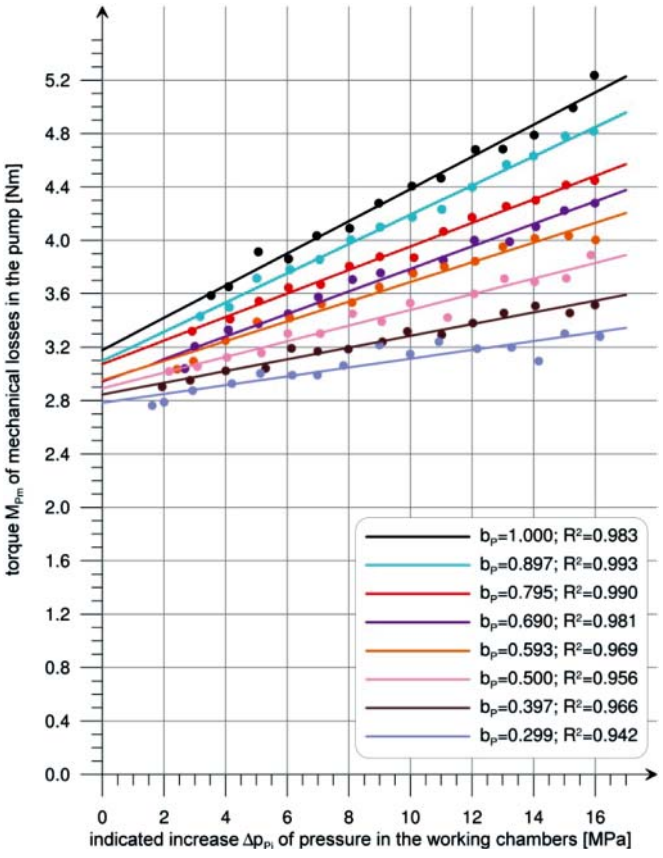


***Fig. 9.3.*** *Torque $M_{Pm}$ of mechanical losses in the PTOZ2-25 pump „working chambers - shaft" assembly as a function of the indicated increase $\Delta p_{Pi}$ of pressure in the working chambers, for different values of the pump capacity coefficient $b_p$, at $v_n$ working liquid viscosity [21]*

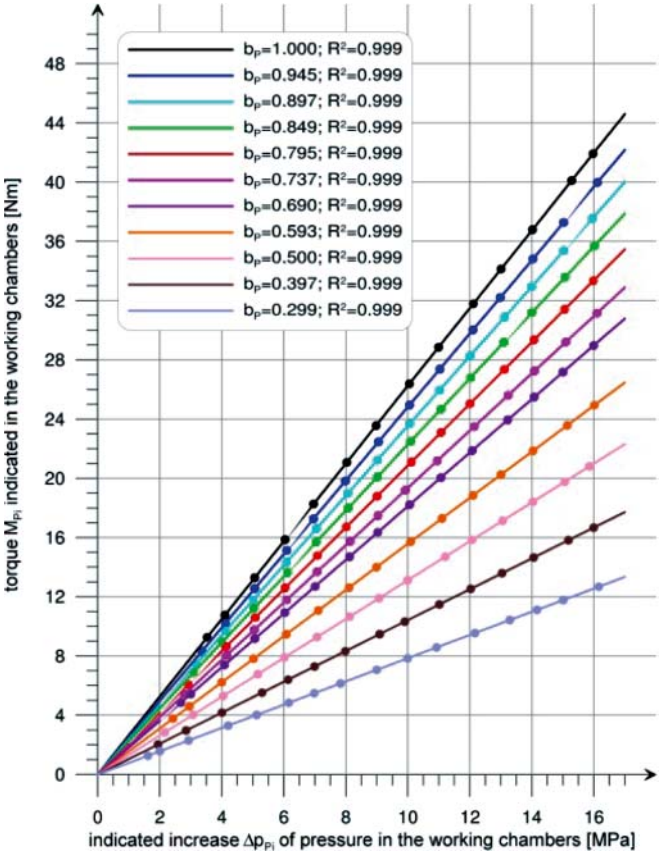


***Fig. 9.2.*** *Torque $M_{Pi}$ indicated in the PTOZ2-25 pump working chambers as a function of the indicated increase $\Delta p_{Pi}$ of pressure in the working chambers, for different values of the pump capacity coefficient $b_p$, at $v_n$ working liquid viscosity [21]*

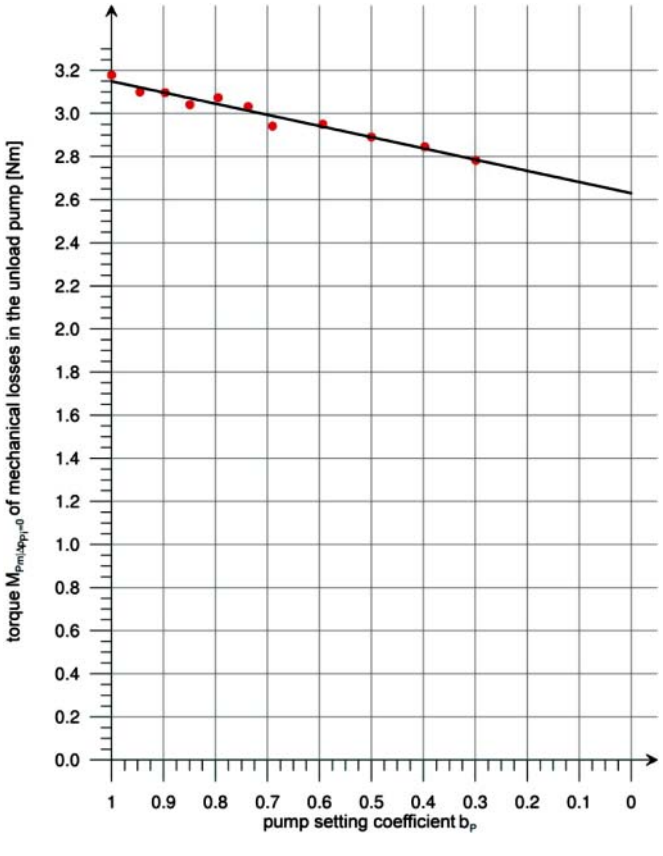


***Fig. 9.4.*** *Torque $M_{Pm|\Delta p_{Pi}=0,\, b_P,\, v_n}$ of mechanical losses in the unloaded PTOZ2-25 pump „working chambers - shaft" assembly as a function of the pump capacity coefficient $b_p$, at $v_n$ working liquid viscosity [21]*

Fig. 9.5 presents the values of increase $\Delta M_{Pm|\Delta p_{Pi}, b_P, \nu_n}$ of torque of mechanical losses calculated from the investigation results. The increase $\Delta M_{Pm|\Delta p_{Pi}, b_P, \nu_n}$ is proportional to the increase $\Delta p_{Pi}$ of pressure in the working chambers and to the instantaneous value $q_{Pgv} = b_P\, q_{Pt}$ of the pump geometrical working volume.

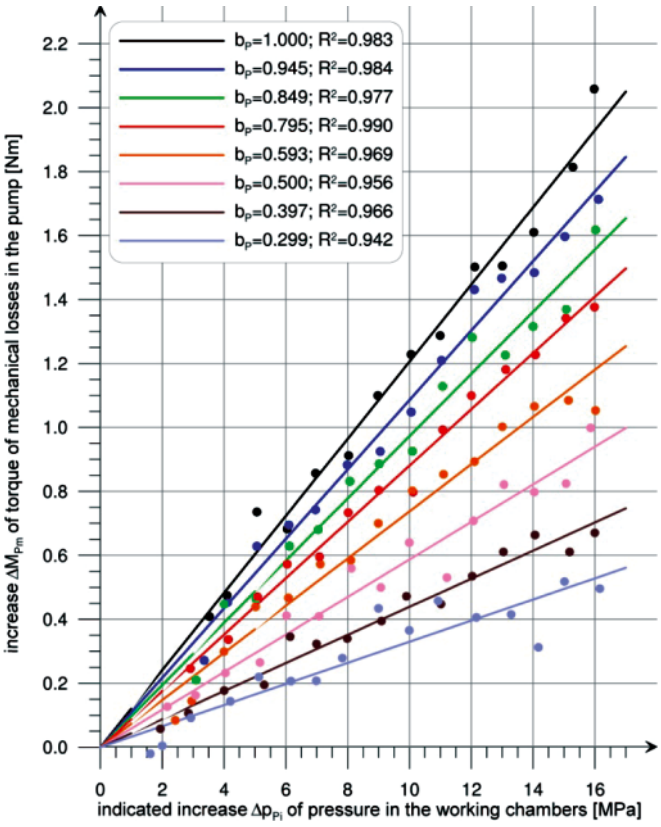


*Fig. 9.5. Increase $\Delta M_{Pm|\Delta p_{Pi}, b_P, \nu_n}$ of the torque of mechanical losses in the PTOZ2-25 pump „ working chambers - shaft" assembly as a function of the indicated increase $\Delta p_{Pi}$ of pressure in the working chambers, for different values of the pump capacity coefficient $b_P$ at $\nu_n$ working liquid viscosity [21]*

Results of the investigation of the torque $M_{Pm}$ of mechanical losses in the PTOZ2 - 25 pump „working chambers - shaft" assembly confirm the mathematical models ((8.9), (8.12)) of mechanical losses in the displacement pump at reference viscosity $\nu_n = 35 mm^2 s^{-1}$.

The above presented results can be achieved with the assumption of little hydraulic oil compressibility, i.e. compressibility with insignificant effect on the change of pump theoretical working volume $q_{Pt}$ ($V_P$) of the working chambers (or the geometrical working volume $q_{Pgv} = b_P\, q_{Pt}$) under the influence of the change of indicated increase $\Delta p_{Pi}$ of pressure in the working chambers.

**The picture of the increase $\Delta M_{Pm|\Delta p_{Pi}, b_P, \nu_n}$ of the torque of mechanical losses in the pump „working chambers - shaft" assembly, complying with the mathematical model (equations (8.9) and (8.12), Fig. 9.5), can be a tool for evaluation of the coefficient $k_{lc|p_n}$ of compressibility of the working liquid used in the hydrostatic transmission system**. The picture of $\Delta M_{Pm|\Delta p_{Pi}, b_P, \nu_n}$ different from that model is then a result of the liquid compressibility, which reduces the values $q_{Pt|\Delta p_{Pi}=p_n}$ (or $q_{Pgv|\Delta p_{Pi}=p_n} = b_P\, q_{Pt|\Delta p_{Pi}=p_n}$) under the influence of the increase $\Delta p_{Pi}$ and, in consequence, reduces the value of indicated torque $M_{Pi}$ in the working chambers and torque $M_P$ on the pump shaft.

In consequence, the value of the increase $\Delta M_{Pm|\Delta p_{Pi}, b_P, \nu_n}$ of the torque of mechanical losses, calculated from expression (9.1), decreases as a difference between torque $M_P$ measured on the pump shaft and torque $M_{Pi}$ calculated with the assumption of non-decreased value $q_{Pt}$ ($V_P$) (or $q_{Pgv} = b_P\, q_{Pt}$). Also decreases the value of coefficient $k_{4.2}$ of the increase $\Delta M_{Pm|\Delta p_{Pi}, b_P, \nu_n}$.

## 10. RESULTS OF INVESTIGATION OF THE TORQUE $M_{PM}$ OF MECHANICAL LOSSES IN THE HIGH PRESSURE PISTON PUMP HYDROMATIK A7V.DR.1.R.P.F.00 TYPE LOADED BY AN OVERFLOW VALVE

Jan Koralewski [22], apart from the verification investigation of the model of volumetric losses of the axial piston variable

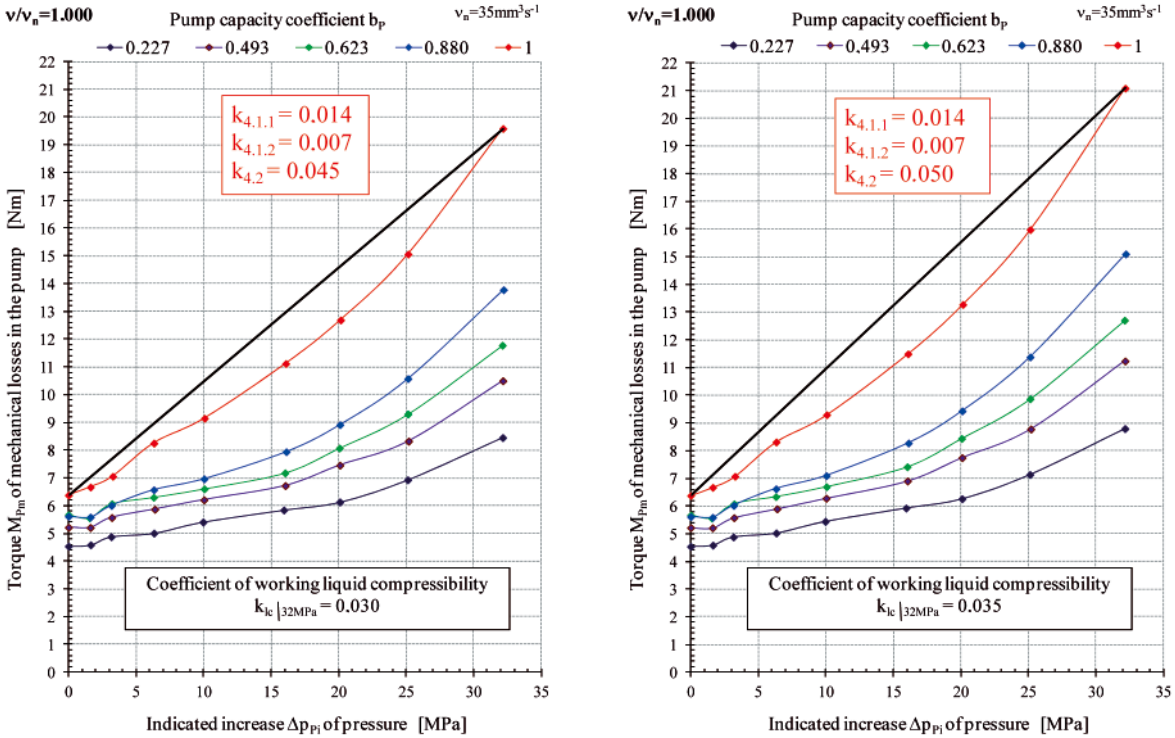


*Fig. 10.2. Picture of the torque $M_{Pm}$ of the pump mechanical losses in the pump "working chambers - shaft" assembly as a function of the indicated increase $\Delta p_{Pi}$ of pressure in the working chambers, at the constant value $\nu/\nu_n = 1$ of the ratio of working liquid viscosity $\nu$ to the reference viscosity $\nu_n$, at the pump capacity coefficient $b_P$ and at different assumed values of working liquid compressibility $k_{lc|32MPa}$: 0.030; 0.035 (pump of the HYDROMATIK A7V.DR.1.R.P.F.00 type) [22]*

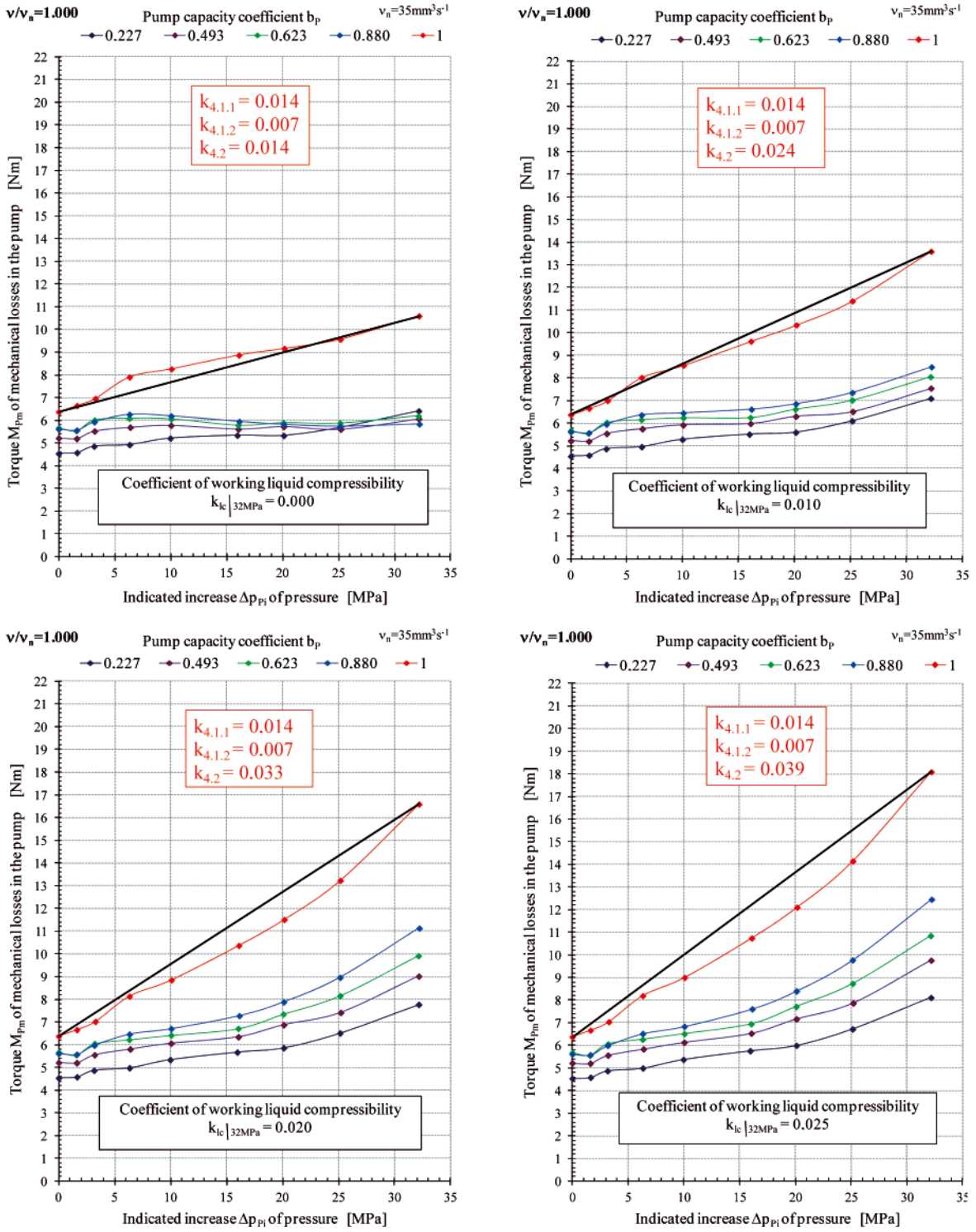


***Fig. 10.1.*** *Picture of the torque $M_{Pm}$ of the pump mechanical losses in the pump „ working chambers - shaft" assembly as a function of the indicated increase $\Delta p_{Pi}$ of pressure in the working chambers, at the constant value $\nu/\nu_n = 1$ of the ratio of working liquid viscosity $\nu$ to the reference viscosity $\nu_n$, at different values of the pump capacity coefficient $b_P$ and at different assumed values of working liquid compressibility $k_{lc|32MPa}$: 0.000; 0.010; 0.020; 0.025 (pump of the HYDROMATIK A7V.DR.1.R.P.F.00 type) [22]*

displacement pump of bent axis design (HYDROMATIK A7V. DR.1.R.P.F.00) (presented in chapter 7), performed, on the test stand presented in Fig. 7.2, the investigation verifying the models (8.9), (8.10), (8.11) and (8.12) of torque of mechanical losses in that pump.

Investigations of volumetric and mechanical losses were carried out simultaneously. The pump was loaded with an overflow valve.

As the investigation of torque $M_{Pm|\Delta p_{Pi}=0}$ of mechanical losses in the „working chambers - shaft" assembly of the unloaded pump (at $\Delta p_{Pi} = 0$) confirmed fully the (8.9), (8.10), and (8.11) models, the investigation of the increase $\Delta M_{Pm|\Delta p_{Pi}, b_P, \nu_n}$ connected with the indicated increase $\Delta p_{Pi}$ of pressure in the pump working chambers did not confirm the model (8.12).

Picture of the increase $\Delta M_{Pm|\Delta p_{Pi}, b_P, \nu_n}$ of the torque of mechanical losses determined by indirect method from expression (9.1) at the assumption, that the coefficient of working liquid compressibility is equal to zero ($k_{lc|32MPa} = 0.000$), presented in Fig. 10.1, differed significantly from the expected picture from models (8.9) and (8.12) and from Fig. 9.5.

Calculations performed with the assumed coefficient of working liquid compressibility $k_{lc|32MPa} > 0$ showed the picture (Fig. 10.1, Fig. 10.2) of the increase $\Delta M_{Pm|\Delta p_{Pi}, b_P, \nu_n}$ closer to models (8.9) and (8.12) and to Fig. 9.5.

Picture most similar to those of models (8.9) and (8.12) is diagram $\Delta M_{Pm|\Delta p_{Pi}, b_P, \nu_n}$ obtained with the assumed coefficient of working liquid compressibility $k_{lc|32MPa} = 0.030$ (Fig. 10.2).

With the assumption of the coefficient $k_{lc|32MPa} = 0.030$, **the obtained increase** of the coefficient $k_{4.2}$ of $\Delta M_{Pm|\Delta p_{Pi}, b_P, \nu_n}$ of the torque of mechanical losses **was from the value $k_{4.2} = 0.014$ to the value of the order of $k_{4.2} = 0.045$**.

At the same time, taking into account the compressibility of working liquid defined by the coefficient $k_{lc|32MPa} = 0.030$, **the decrease is obtained** of the coefficient $k_1$ of volumetric losses in the pump (expression (7)) **from the value $k_1 = 0.065$ to the value of the order of $k_1 = 0.035$**.

## CONCLUSIONS

1. Energy investigation of the high pressure displacement **variable capacity pump** operating in an aerated hydrostatic system allows to determine **approximate value of the coefficient $k_{lc|p_n}$ of working liquid compressibility** by comparing the picture of the increase $\Delta M_{Pm|\Delta p_{Pi}, b_P, \nu_n}$ of the torque of mechanical losses in the „working chambers - shaft" assembly with the model of increase of that torque.
2. The approximate determination of the value of $k_{lc|p_n}$ coefficient of working liquid compressibility allows to modify the coefficient $k_{4.2}$ of the increase $\Delta M_{Pm|\Delta p_{Pi}, b_P, \nu_n}$ of the torque of mechanical losses in the pump „working chambers - shaft" assembly (towards its increase) and the value of coefficient $k_1$ of volumetric losses in the pump working chambers (towards its decrease).
3. Therefore, it is possible to determine approximately the effect of the working liquid compressibility on the picture of values and proportion of the mechanical losses and volumetric losses in the pump.
4. Working liquid compressibility reduces the pump theoretical working volume $q_{Pt|\Delta p_{Pi}=p_n}$ of the working chambers (or the geometrical working volume $q_{Pgv|\Delta p_{Pi}=p_n} = b_P\, q_{Pt|\Delta p_{Pi}=p_n}$) under the influence of the change of indicated increase $\Delta p_{Pi}$ of pressure in the working chambers.
5. The simplifying assumption is adopted, that the sum of the values of working liquid compressibility coefficient $k_{lc|p_n}$ and coefficient $k_1$ of volumetric losses in the pump equals to the value of coefficient $k_1$ when it includes also the effect of working liquid compressibility.
6. In the mathematical models of pump energy efficiency and hydrostatic drive system efficiency and also of the system operation field ($0 \le \overline{\omega}_M < \overline{\omega}_{Mmax}$, $0 \le \overline{M}_M < \overline{M}_{Mmax}$), either the coefficient $k_1$ (which includes also the effect of working liquid compressibility) or the above defined sum ($k_{lc|p_n} + k_1$) must be used.

### BIBLIOGRAPHY


1. Paszota Z.: *Graphical presentation of the power of energy losses and power developed in the elements of hydrostatic drive and control system. Part I – Rotational hydraulic motor speed series throttling control systems*. Chapter in the monograph: *„Research, design, production and operation of hydraulic systems"* (in Polish), Adam Klich, Edward Palczak and Andrzej Meder editors. „Cylinder" Library. Komag Mining Mechanisation Centre, Gliwice 2008
2. Paszota Z.: *Graphical presentation of the power of energy losses and power developed in the elements of hydrostatic drive and control system. Part II – Rotational hydraulic motor speed parallel throttling control and volumetric control systems*. Chapter in the monograph: *„Research, design, production and operation of hydraulic systems"* (in Polish), Adam Klich, Edward Palczak and Andrzej Meder editors. „Cylinder" Library. Komag Mining Mechanisation Centre, Gliwice 2008
3. Paszota Z.: *Direction of increase of power stream in the hydrostatic drive and control system. Graphical presentation of the power of energy losses and power developed in the elements of hydrostatic drive and control system. Part I – Rotational hydraulic motor speed series throttling control systems* (in Polish), Napędy i sterowanie, scientific monthly, No 10 (114), October 2008
4. Paszota Z.: *Direction of increase of power stream in the hydrostatic drive and control system. Graphical presentation of the power of energy losses and power developed in the elements of hydrostatic drive and control system. Part II – Rotational hydraulic motor speed parallel throttling control and volumetric control systems* (in Polish), Napędy i sterowanie, scientific monthly, No 11 (115), November 2008
5. Paszota Z.: *Graphical presentation of the power of energy losses and power developed in the elements of hydrostatic drive and control system. Part I – Rotational hydraulic motor speed series throttling control systems*. Polish Maritime Research 3 (57) 2008, Vol. 15
6. Paszota Z.: *Graphical presentation of the power of energy losses and power developed in the elements of hydrostatic drive and control system. Part II – Rotational hydraulic motor speed parallel throttling control and volumetric control systems.* Polish Maritime Research 4 (58) 2008,Vol. 15
7. Paszota Z.: *The operating field of a hydrostatic drive system*. Chapter in the monograph: *„Research, design, production and operation of hydraulic systems"* (in Polish), Adam Klich, Antoni Kozieł and Edward Palczak editors. „Cylinder" Library. Komag Mining Mechanisation Centre, Gliwice 2009
8. Paszota Z.: *Parameters of the energy efficiency investigations of pumps and hydraulic motors. The operating field of a hydrostatic drive system* (in Polish), Napędy i sterowanie, scientific monthly, No 11 (127), November 2009
9. Paszota Z.: *The operating field of a hydrostatic drive system parameters of the energy efficiency investigations of pumps and hydraulic motors*. Polish Maritime Research 4 (62) 2009, Vol. 16
10. Paszota Z.: *Energy losses in a rotational hydraulic motor – definitions and relations for evaluation of the efficiency of motor and hydrostatic drive*. Chapter in the monograph: *„Research, design, production and operation of hydraulic systems"* (in Polish), Adam Klich, Antoni Kozieł and Edward Palczak editors. „Cylinder" Library. Komag Mining Mechanisation Centre, Gliwice 2010
11. Paszota Z.: *Theoretical and mathematical models of the torque of mechanical losses in a hydraulic rotational motor for hydrostatic drive*. Chapter in the monograph: *„Research, design, production and operation of hydraulic systems"* (in Polish), Adam Klich, Antoni Kozieł and Edward Palczak editors. „Cylinder" Library. Komag Mining Mechanisation Centre, Gliwice 2010
12. Paszota Z.: *Energy losses in a rotational hydraulic motor – definitions and relations for evaluation of the efficiency of motor and hydrostatic drive* (in Polish), Napędy i sterowanie, scientific monthly, No 10 (138), October 2010
13. Paszota Z.: *Theoretical and mathematical models of the torque of mechanical losses in a hydraulic rotational motor for hydrostatic drive* (in Polish), Napędy i sterowanie, scientific monthly, No 11(139), November 2010
14. Paszota Z.: *Energy losses in the hydraulic rotational motor – definitions and relations for evaluation of the efficiency of motor and hydrostatic drive*. Polish Maritime Research 2 /2010
15. Paszota Z.: *Theoretical and mathematical models of the torque of mechanical losses in a hydraulic rotational motor for hydrostatic drive*. Polish Maritime Research 3/2010
16. Paszota Z.: *Hydrostatic drives as safe and energy saving machines* (in Polish), Napędy i sterowanie, scientific monthly, No 1(141), January 2011

17. Paszota Z.: *Hydrostatic drives as safe and energy saving machines* (in Polish), Proceedings of the „Innovative machines and Technologies - Safety" conference, Szczyrk 03 – 04 February 2011
18. Paszota Z.: *Hydrostatic drives as safe and energy saving machines. The drive investigation method compatible with the diagram of power increase opposite to the direction of power flow*. Polish Maritime Research 1/2011,
19. Paszota Z.: *Theoretical models of the torque of mechanical losses in the pump used in a hydrostatic drive*. Polish Maritime Research 4 / 2011,
20. Koralewski J.: *Influence of hydraulic oil viscosity on the volumetric losses in a variable capacity pump.* Polish Maritime Research. 3/2011
21. Czyński M.: *Laboratory investigation of the model of hydrostatic transmission energy efficiency.* (in Polish). Doctor dissertation. Szczecin University of Technology, Faculty of Marine Engineering, 2005,
22. Koralewski J.: *Effect of the working liquid viscosity on the energy losses in a variable capacity piston pump.* (in Polish). Doctor dissertation (continued). Gdansk University of Technology, Faculty of Ocean Engineering and Ship Technology,
23. Skorek G.: *Energy characteristics of the hydraulic system with proportional control of the hydraulic cylinder fed by a constant capacity pump in a constant pressure and variable pressure system.* (in Polish). Doctor dissertation. Gdansk University of Technology, Faculty of Ocean Engineering and Ship Technology, 2008
24. Paszota Z.: *Model of volumetric losses in the variable capacity displacement pump used in hydrostatic drive* (in Polish). „Napędy i Sterowania'2006". „TECHNICON'06" Gdańsk, 25.10.2006.
25. Paszota Z.: *Aspects énergétiques des transmissions hydrostatiques*. Monograph, Gdansk 2002.
26. Paszota Z.: *Model of the energy losses in the displacement rotational machines for description of efficiency of the hydrostatic drive. Part I. Model of volumetric losses*. Polish Maritime Research. 3/2000.

---

**CONTACT WITH THE AUTHOR**

Prof. Zygmunt Paszota
Faculty of Ocean Engineering
and Ship Technology
Gdansk University of Technology
Narutowicza 11/12
80-233 Gdansk, POLAND
e-mail: zpaszota@pg.gda.pl

**POLISH MARITIME RESEARCH** 3(75) 2012 Vol 19; pp. 45-52
10.2478/v10012-012-0030-6

# Computational model for simulation of lifeboat motions during its launching from ship in rough seas

**Paweł Dymarski**, Ph.D.
**Czesław Dymarski**, Prof.
Gdańsk University of Technology

ABSTRACT

*This paper presents a computational model which describes motion of an object of six degrees of freedom (DoF), intended for simulation of spatial motion of one- or two- rope-sling lifeboat or rescue boat during its launching from ship in rough sea. This is a complex model which accounts for sea conditions as well as elasticity and damping properties of davit's elements and mechanisms, rope and boat hull. Also, are presented results of example calculations for an assumed set of technical parameters of davit and boat as well as sea conditions.*

**Key words**: ship in rough seas; life saving appliances (LSA); lifeboat launching; lifeboat motions; lifeboat launching simulation

## INTRODUCTION

Human life protection and rescue is one of the most important problems which must be faced by designers of objects doing duty for man, especially sea-going passenger ships.

Life saving appliances (LSA) systems which make it possible to evacuate persons especially from large passenger ships, have evaluated beginning from the simplest open lifeboats and rafts thrown off into water and ending to unsinkable sheltered boats of high strength and fire resistance, lowered with the use of more and more advanced side davits.

In Fig. 1 is presented a photo of an example contemporary davit together with suspended boat during launching it into water.

Operation of launching boats together with embarked persons into water is the most hazardous phase of process of rescuing persons from endangered ship in rough seas. Boat, during its launching from a significant height in the neighbourhood of rolling ship's side, often impacts against the side. In the case of large passenger ships the lowering height is significant and boat displaces close to ship side, that often leads to its bumping against the side. The bumps generate the relatively largest overloading which results from a change of motion of the boat and affects persons inside the boat. The overloads may lead to failures of boat and person injures and even casualties. For this reason many recognized research centres as well as leading producers of ship life saving and rescue appliances are searching for more and more exact methods for calculation of motion parameters of boat lowered from ship to water in rough seas conditions. When a reliable computational software is at disposal it is possible to perform investigations of LSA systems intended for rough seas conditions. This allows to improve the existing design solutions and test new ones of the devices in question.

***Fig. 1.*** *View of the lifeboat and the luffing-jib davit during launching test*

The problem was included into the scope of the research program realized, in the period of 2004-2009, within the frame of the European project SAFECRAFTS (Safe Abandoning of Ships - improvement of current Life Saving Appliances Systems) in which also the Faculty of Ocean Engineering and Ship Technology, Gdansk University of Technology, took part [2].

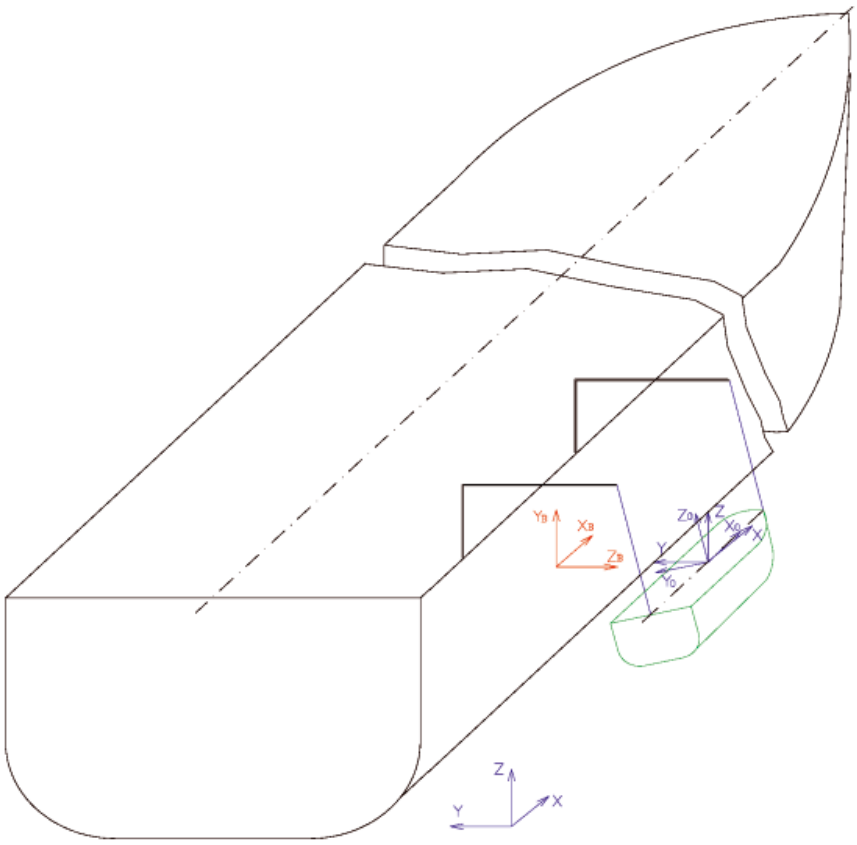


***Fig. 2.*** *Coordinate systems:* $x, y, z$ *– absolute coordinate system,* $x_0, y_0, z_0$ *– local coordinate system of the boat,* $x_B, y_B, z_B$ *– local coordinate system of the ship*

This paper presents results of one of the project's tasks realized by these authors, which concerns elaboration of a complex mathematical model and computational program, called RESBO, intended for simulation of lifeboat motion during its launching from ship in rough seas.

## GENERAL DESCRIPTION OF RESBO PROGRAM

RESBO program serves to simulation of 3D motion of one- or two – suspension - point object during its launching from the ship in waves and its recovering as well. The program is prepared for simulation of the 1 - point lifeboat, 1- point fast rescue boat, 1- point davit for launching life raft and 2 - point lifeboat.

The RESBO was written in C++ language and compiled under Linux system.

Algorithm of the program takes into account:

- movement of the ship in waves
- operation of davit mechanisms
- elasticity and damping properties of davit parts
- elasticity and damping properties of object hull
- influence of wind
- lifeboat impact against ship's side
- lifeboat impact against water during launching
- movement of the lifeboats in waves during a short period after releasing the hooks.

## THEORETICAL MODEL

### *Assumptions*

The object (e.g. lifeboat) is modelled as a rigid body. However special flexible elements called "fenders" are attached to one side of the lifeboat hull. The object performs motions of 6 DoF. Elements and factors restricting (extorting) motion of the object are formulated as external forces dependent on

- relative position between the object and a restricting (extorting) element
- relative velocity
- time

Influence of the elasticity and damping properties of the object structure on its motion is formulated as a separate segment of the extorting forces function.

The elements and factors restricting (extorting) motion of the object are the following:

- suspension system and mechanisms: ropes, davit arm, absorber, brake, with regard to elasticity and damping properties of the hull construction in hook suspension point
- ship's side which restricts area range of the object's motions (possibility of the impact against ship's side)
- wind – aerodynamic reaction
- force of gravity
- water – hydrostatic and hydrodynamic reaction, including slamming
- functioning the hydrostatic locking device

The launching system includes: brake and the elements connected in series: davit arm, absorber, rope and catch. The elements transfer the same load, hence deformation of the system is a sum of their deformations.

### *The object's motion equations*

The dynamic equations of free spatial motion of the solid are as follows [1]:

$$m\,\ddot{x}_c = \sum_{i=1}^{k} F_{xi} \quad m\,\ddot{y}_c = \sum_{i=1}^{k} F_{yi} \quad m\,\ddot{z}_c = \sum_{i=1}^{k} F_{zi}$$

$$J_{x_0}\ddot{\varphi}_{x_0} - (J_{x_0} - J_{z_0})\dot{\varphi}_{y_0}\dot{\varphi}_{z_0} = \sum_{i=1}^{k} M_{x_0 i}$$

$$J_{y_0}\ddot{\varphi}_{y_0} - (J_{z_0} - J_{x_0})\dot{\varphi}_{z_0}\dot{\varphi}_{x_0} = \sum_{i=1}^{k} M_{y_0 i}$$

$$J_{z_0}\ddot{\varphi}_{z_o} - (J_{x_0} - J_{y_0})\dot{\varphi}_{x_0}\dot{\varphi}_{y_0} = \sum_{i=1}^{k} M_{z_0 i}$$

$x_c, y_c, z_c$ – coordinates of the solid's mass centre
$x_o, y_o, z_o$ – principal central axes of inertia (moving system)
$\dot{\varphi}_{x_o}, \dot{\varphi}_{y_o}, \dot{\varphi}_{z_o}$ – momentary angular velocities of the solid rotating around principal central axes of inertia
$J_{x_o}, J_{y_o}, J_{z_o}$ – principal central moments of inertia of the boat
$F_{xo}, F_{yo}, F_{zo}$ – vectors of „i" force
$M_{x_o}, M_{y_o}, M_{z_o}$ – vectors of moment of „i" force relative to central axes of inertia

## *Forces*

The forces which influence the object $\mathbf{F}_i$, depend on:

- the position of the gravity centre of the object, $\mathbf{x}_c$, and the vector of the angular position, $\boldsymbol{\varphi}$, (position of the object's local coordinate system determined by the principal central axes of inertia: $\mathbf{x}_o, \mathbf{y}_o, \mathbf{z}_o$)
- the vector of linear velocity, $\dot{\mathbf{x}}_c$, and angular velocity, $\dot{\boldsymbol{\varphi}}$
- the wind velocity and direction, $\mathbf{v}_{wind}$
- time t

$$\mathbf{F}_i = \mathbf{F}_i(\mathbf{x}_c, \dot{\mathbf{x}}_c, \boldsymbol{\varphi}, \dot{\boldsymbol{\varphi}}, \mathbf{v}_{wind}, t)$$

Detailed description of the forces function $F_i$ follows from reaction of the elements on the object.

## *Characteristics of the system's elements*

### Davit

The davit is modelled as a linear springy element (without restriction of linear range). The stiffness of the davit, EI, is an input parameter of the algorithm.

### Absorber

The absorber is modelled as a linear springy element with restrictions for the deformation: $\Delta l_0$ and $\Delta l_1$ As assumed, the absorber starts working when the force in the rope, Fr, reaches its nominal value Frn, and stops when it obtains the value of 1,5 Frn. The absorber has immanent friction – if velocity of the deformation is not zero, then the friction force Ta which inhibits progress of the process, appears. Module of the force has constant value, independent of the force transferred by the absorber. The absorber is defined by the following parameters: $\Delta$lo, Fr, Ta, $v_0$.

The parameter $v_0$ - velocity of friction waning (below this value of deformation velocity, friction linearly decreases to zero) is added only to obtain numerical solution. It does not follow from physical model of the system.

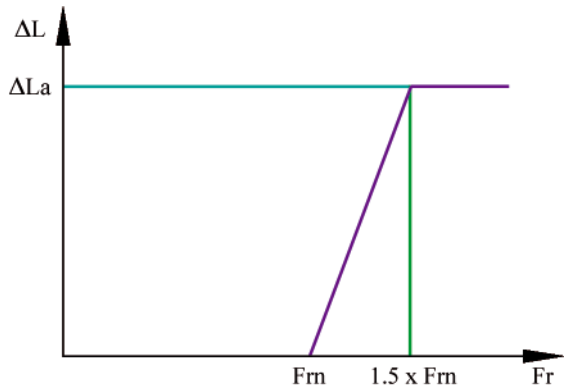


*Fig. 3. Assumed static characteristic of the absorber*

### Steel rope

The rope is modelled as a linear springy element with the minimum restriction for the transferred force: $Q_0 = 0$. It means that the force in the rope cannot be negative, but process of the rope length reduction can be still in progress. The rope is defined by the following parameters: its length l, cross-section area A, Young modulus E.

### "Catch" of the rope to the object

This is an imaginary element added for taking into account elasticity and damping properties of the object's hull structure. When we simulate a system without absorber, function of the catch can be especially noticeable. The catch is modelled as a linear springy element. Its damping is modelled as an immanent friction, linearly dependent of transferred force.

The catch characteristic is defined by the following parameters: its stiffness I, friction coefficient f, velocity of friction waning $v_0$.

### Fender

The fender is modelled as a linear springy element with a minimum restriction for the transferred force. It cannot work on stretching. It starts working in the moment of contact with ship's side. Its damping properties are: immanent friction which is in opposite direction to the perpendicular vector of the fender velocity relative to ship side surface. Damping force depends linearly on fender pressure force. Tangent friction force of the fender on the ship side surface is modelled analogously.

The fender characteristic is defined by the following parameters: its stiffness I, perpendicular friction coefficient $f_n$, tangent friction coefficient $f_t$, velocity of friction waning $v_0$.

### Centrifugal brake

The centrifugal brake controls unreeling velocity of the ropes during launching the boat. The velocity is linearly dependent of force transferred by the rope. The brake's characteristic is presented in Fig. 4.

### Hydrostatic locking device

The hydrostatic locking device is used for releasing the hook and disconnecting lifeboat's steel ropes during launching. The device is defined by its position level.

### Aerodynamic reaction

Motion of the object in the air causes aerodynamic reaction. This force can be described as follows:

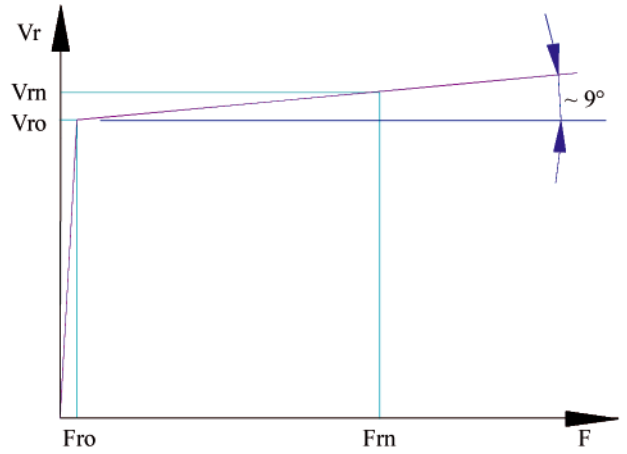


***Fig. 4.*** *Assumed characteristic of the centrifugal brake, where:* ***Vro*** *– the minimum value of the velocity* ***Vr*** *of the ropes which triggers the centrifugal brake and begins to control of unreeling velocity of the ropes during launching the boat,* ***Fro***, ***Frn*** *– the minimum and nominal values of the load in the ropes during controlled launching the boat*

$$R_A = C_A \frac{\rho |\mathbf{V}_A| \mathbf{V}_A S}{2}$$

where:
CA– air resistance coefficient
ρ – air density
VA – object's velocity relative to the air, including wind
S – windage area

### Hydrostatic reaction

The hydrostatic reaction is connected with hydrostatic pressure exerted on lifeboat hull's wetted area. The reaction which acts on the area element dS in the direction determined by the unit vector n, is calculated as follows:

$$dF_{hs} = -\rho_w g h \mathbf{n} dS$$

where:
$\rho_w$ – water density
g – gravitational acceleration
h – immersion depth of the area element dS
**n** – unit vector normal to the area element dS

The total hydrostatic reaction is calculated as follows:

$$F_{hs} = -\int_S \rho_w g h \mathbf{n} dS$$

### Hydrodynamic reaction

Lifeboat movement in the water induces hydrodynamic reaction which is roughly equal to sum of frictional resistance and pressure resistance. The force vector of the frictional resistance is calculated as follows:

$$R_F = C_F \, '' \, \rho_w \int_S |\boldsymbol{\upsilon}_w| (\boldsymbol{\upsilon}_w \cdot e_t) \mathbf{t} \, dS$$

where:
$C_F$ – frictional resistance coefficient
$\boldsymbol{\upsilon}_w$ – tangential component of the velocity vector of the area element dS, in relation to the water
**t** – unit vector tangent to the area element dS, defined as follows:

$$e_t = \frac{\boldsymbol{\upsilon}_w - (\boldsymbol{\upsilon}_w \cdot \mathbf{n})\mathbf{n}}{|\boldsymbol{\upsilon}_w - (\boldsymbol{\upsilon}_w \cdot \mathbf{n})\mathbf{n}|}$$

where:
**n** – unit vector normal to the area element dS.

The force vector of the pressure resistance is calculated as follows:

$$R_p = C_p \, '' \, \rho_w \int_S |\boldsymbol{\upsilon}_w \cdot \mathbf{n}| (\boldsymbol{\upsilon}_w \cdot \mathbf{n}) \mathbf{n} \, dS$$

where:
$C_p$ – pressure resistance coefficient.

### Free surface reaction (slamming)

The pressure caused by hull impact against free water surface is calculated by using the von Karman formula:

$$p_{slam} = \frac{\rho_w \upsilon_0^2}{2} \frac{\pi ctg(\alpha)}{(1 + \frac{\rho_w g \pi x^2}{2W})}$$

where:
$\upsilon_o$ – first impact velocity [m/s]
α – angle of inclination of the lifeboat bottom surfaces [deg]
$\rho_w$ – water density [kg/m$^3$]
g – gravitational acceleration [m/s$^2$]
x – breadth of the wetted part of the bottom [m]
W – weight of the body per unit length [N/m]

The total reaction of slamming is calculated by using the following integral:

$$R_{slam} = -\int_S p_{slam} \mathbf{n} \, dS$$

where:
**n** – unit vector normal to the area element dS

## NUMERICAL MODEL

The applied calculation algorithm of the object motion is based on the Euler explicit method. Its essence can be described as follows:

0. START. Initiation of the constant values. Reading input data.
1. Number of updating: n = n+1
2. Calculation of current position of ship.
3. Calculation of forces in the elements according to positions of ship and object.
4. Summing the forces and reactions which influence the object:
   a. Gravity force
   b. Aerodynamic reaction
   c. Force in the rope
   d. Force in the fender
   e. Hydrostatic reaction
   f. Hydrodynamic reaction
   g. Force of the free water surface impact (slamming)
5. Calculation of a new position and velocity of the object, resulting from forces working in the time interval Δt.
6. Calculation of a new length of the rope
7. Updating the time: $t_{n+1} = t_n + \Delta t$.
8. If $t_{n+1} = t_{max,}$ then go to STOP; if not, go to 1.

## RESBOVI PROGRAM

The RESBOVI program is the post-processor for the RESBO program. It serves to visualize (animate) the calculation results of the lifeboat (or rescue boat) motion during its launching (and recovering) from the ship in waves. The RESBOVI was written in C++ language and compiled under Linux system.

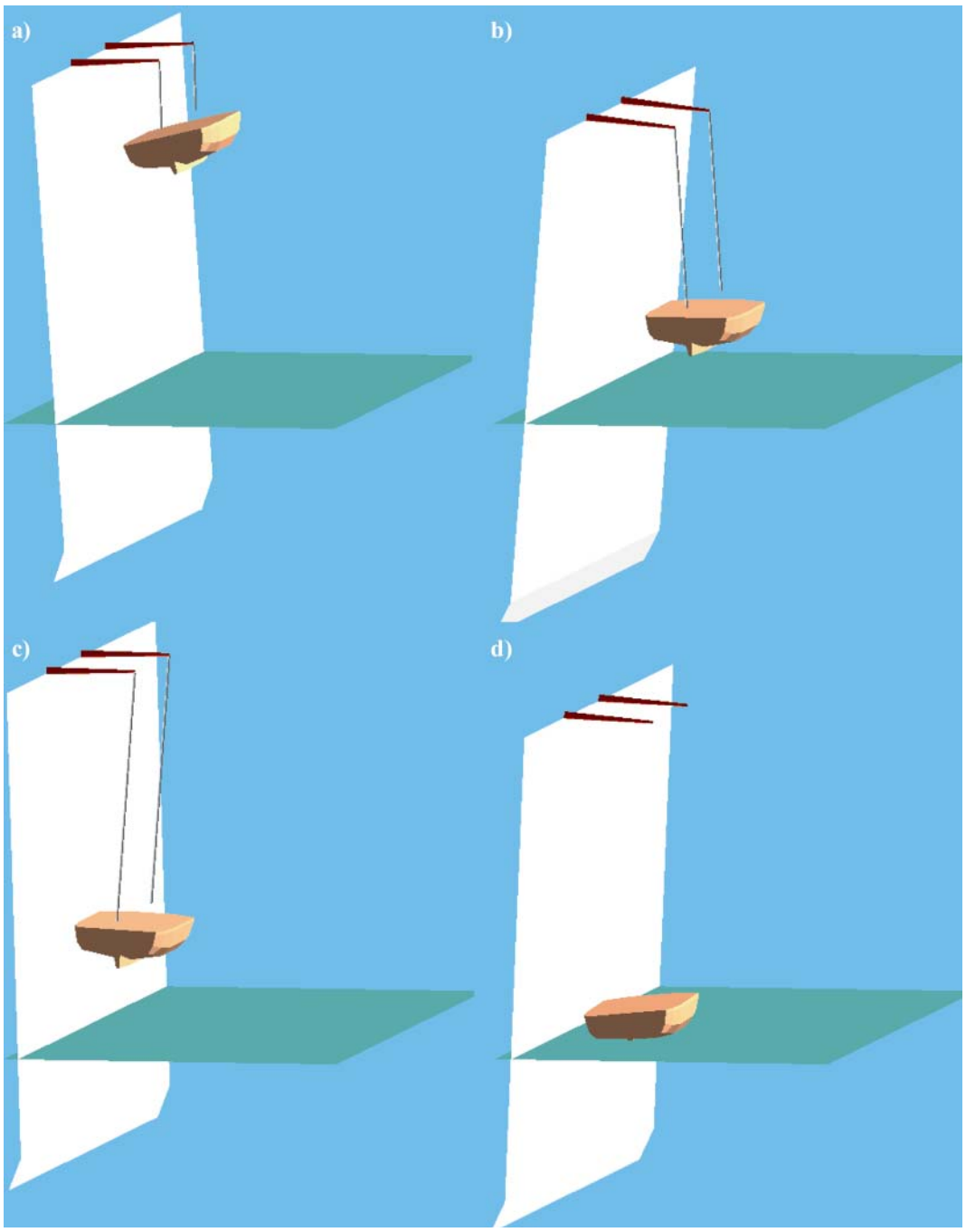


***Fig. 5.*** *Lifeboat during launching. Freeze frames (dumps) taken from the RESBOVI animation*

In Fig. 5 are given 4 successive screen dumps of animation which presents calculation results based on the following example test data:

- Heave and roll period of ship: T = 8 s
- Heave amplitude: $Z_A$ = 1.0 m
- Drift amplitude: $Y_A$ = 0.8 m
- Roll amplitude: $\Phi_A$ = 1.0 m
- Distance between ship's side and its symmetry plane (PS): B/2 = 16.1 m
- Distance between boat's centre of gravity(CG) and ship's PS: bl = 20.1 m
- Distance between ropes suspending the boat: l = 8 m
- Initial position of the suspension point: h = 20 m
- Mass of the boat: m = 15550 kg
- Boat's moments of inertia: Jx, Jy, Jz = 36792, 80102, 80102 kg, respectively
- Steel rope diameter: d = 16 mm
- Nominal lay-out velocity of rope: $V_{rn}$ = 0.8 m/s

## CALCULATION CASES

The calculation cases concern the two- suspension- point lifeboat in 3D movement during launching (and recovering) from the ship in waves. Two cases are selected to compare their calculation results.

The first case applies to the system with elasticity and damping properties of the davit arm, rope, centrifugal brake and boat's hull. For comparison purposes, a small absorber is added to the system which is used for fast rescue boat davit. The second case, without any absorber, applies to the lifeboat davit system. Below in the sections 6.1 and 6.2 in the successive figures are presented calculation results for both the considered systems in the form of runs of the main parameters which describe motion of the life boat with embarked persons during its launching from ship to water in rough seas. The successive figures present the following:

- Fig. 6 and 11: Displacement (linear motion) of the boat's centre of gravity against the Earth (in the coordinate system x,y,z – acc. Fig. 2).
  $G_X$ – displacements along x- axis – horizontal parallel to the ship's plane of symmetry (PS);
  $G_Y$ – displacements along y- axis – horizontal perpendicular to the ship's plane of symmetry (PS);
  $G_Z$ – displacements along z- axis – vertical.
- Fig. 7 and 12: Run of change in position of the local boat-fixed coordinate system in the global system:
  $Exo_x$, $Exo_y$, $Exo_z$ – coordinates of the unit vector **Exo** which determines direction and sense of Xo – axis of the local boat-fixed coordinate system;
  $Eyo_x$, $Eyo_y$, $Eyo_z$ – coordinates of the unit vector **Eyo** which determines direction and sense of Yo – axis of the local boat-fixed coordinate system;
  $Ezo_x$, $Ezo_y$, $Ezo_z$ – coordinates of the unit vector **Ezo** which determines direction and sense of Zo – axis of the local boat-fixed coordinate system).
- Fig. 8 and 13: Displacement (linear motion) of the centre of gravity of boat and its oscillations (angular motions) against ship's side (the coordinate system $X_B$, $Y_B$, $Z_B$ – acc. Fig. 2).
  $G_{XB}$ – displacements along $X_B$ - axis –parallel to the ship's plane of symmetry (PS);
  $G_{YB}$ – displacements along $Y_B$ - axis –parallel to the ship's plane of symmetry (PS);
  $G_{ZB}$ – displacements along $Z_B$ - axis –perpendicular to the ship's plane of symmetry (PS);
  Roll, pitch, yaw – angular displacements (motions) of the boat;
- Fig. 9 and 14: Linear and angular accelerations acting onto the boat.
  $a_x$, $a_y$, $a_z$– components of linear acceleration vector;
  $\varepsilon_x$, $\varepsilon_y$, $\varepsilon_z$ – components of angular acceleration around the axis X,Y, Z, respectively;
- Fig. 10 and 15: Linear and angular velocities of the boat against the Earth.
  $V_x$, $V_y$, $V_z$ – components of linear velocity vector;
  $\omega_x$, $\omega_y$, $\omega_z$ – components of angular velocity vector.

## *System with absorber and elasticity and damping properties Diagrams*

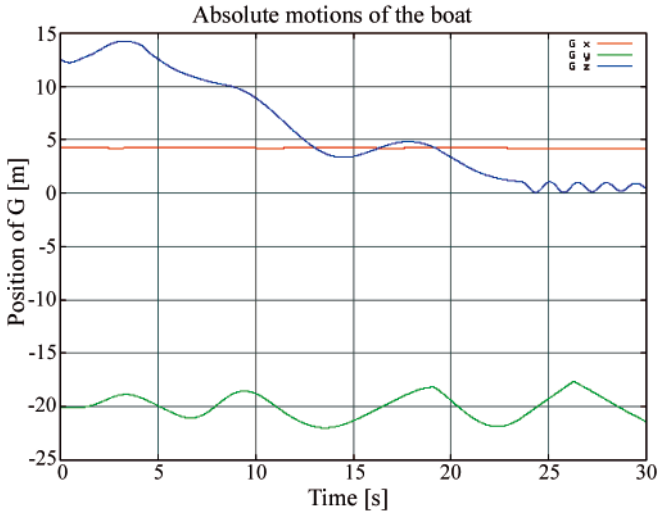


***Fig. 6.*** *Linear and angular motions of the lifeboat. Absolute coordinate system. Diagram of the mass centre motions*

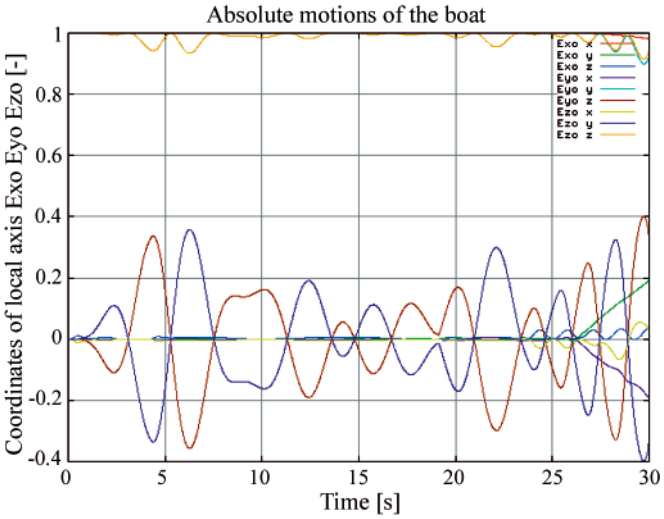


***Fig. 7.*** *Angular motions of the lifeboat. Absolute coordinate system. Unit vectors of the boat's local coordinate system*

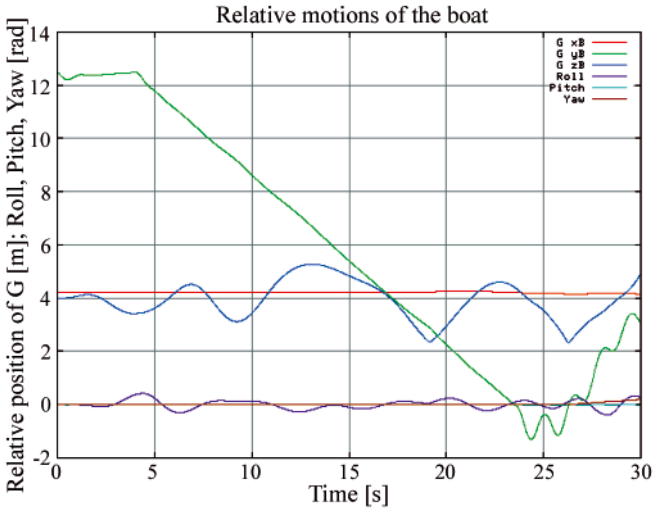


***Fig. 8.*** *Linear and angular motions of the lifeboat. Ship side's coordinate system. Diagram of the relative motions of lifeboat's mass centre and the lifeboat rotations: roll, pitch, yaw*

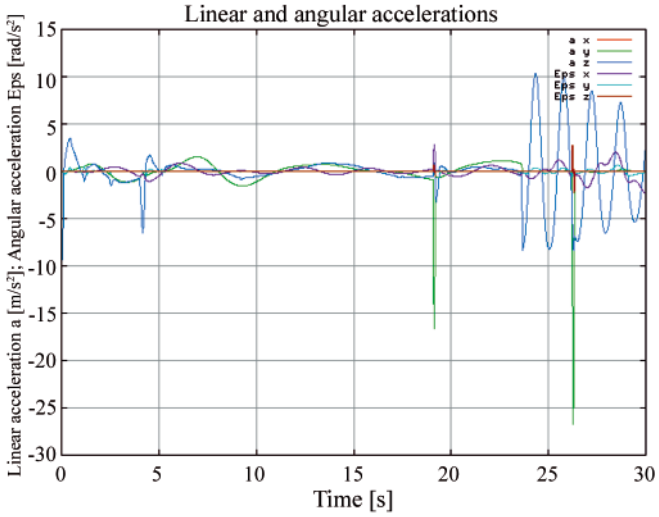


***Fig. 9.*** *Linear and angular accelerations of the lifeboat*

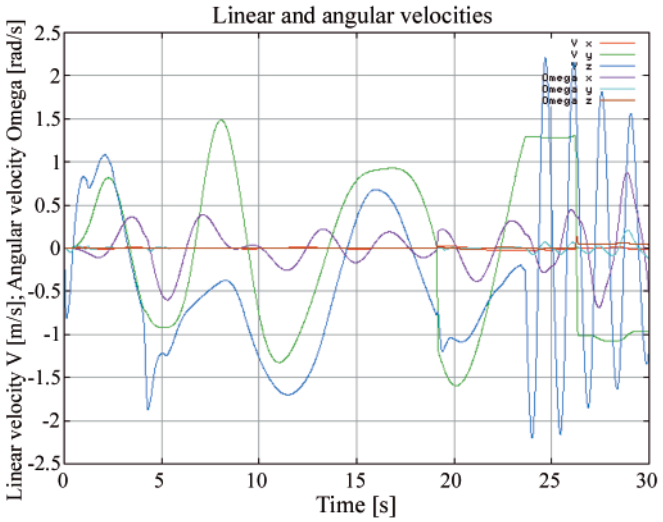


*Fig. 10. Linear and angular velocities of the lifeboat*

## *System without absorber Diagrams*

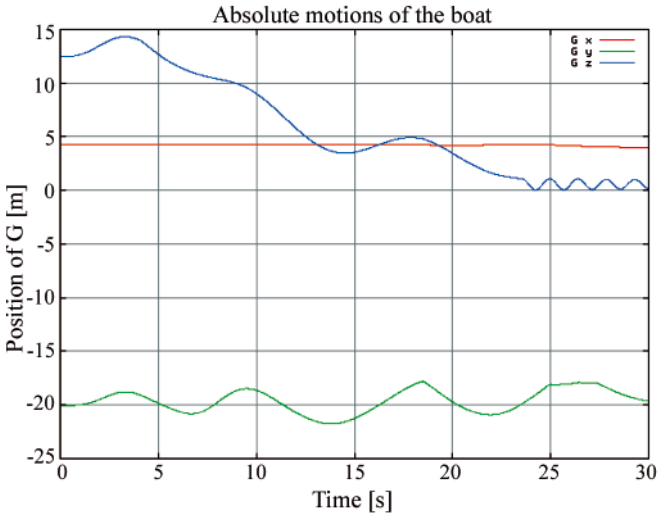


*Fig. 11. Linear and angular motions of the lifeboat. Absolute coordinate system. Diagram of the mass centre motions*

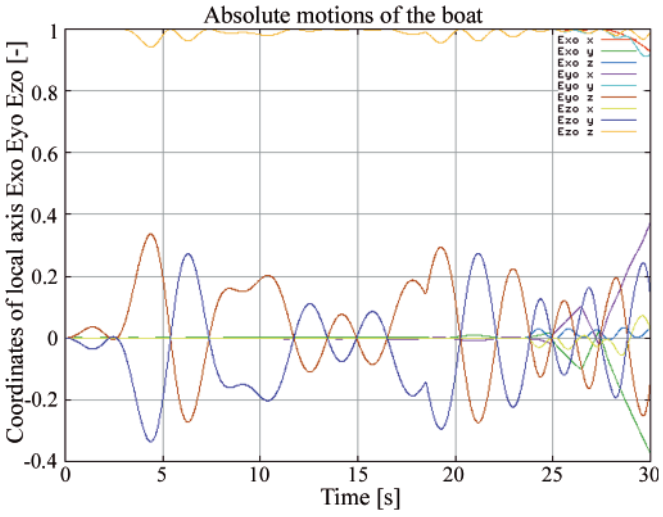


*Fig. 12. Angular motions of the lifeboat. Absolute coordinate system. Unit vectors of the boat's local coordinate system*

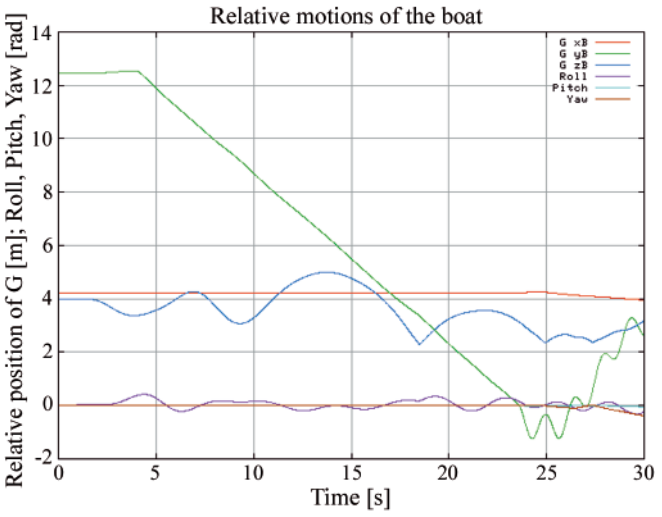


*Fig. 13. Linear and angular motions of the lifeboat. Ship side's coordinate system. Diagram of the relative motions of lifeboat's mass centre and the lifeboat rotations: roll, pitch, yaw*

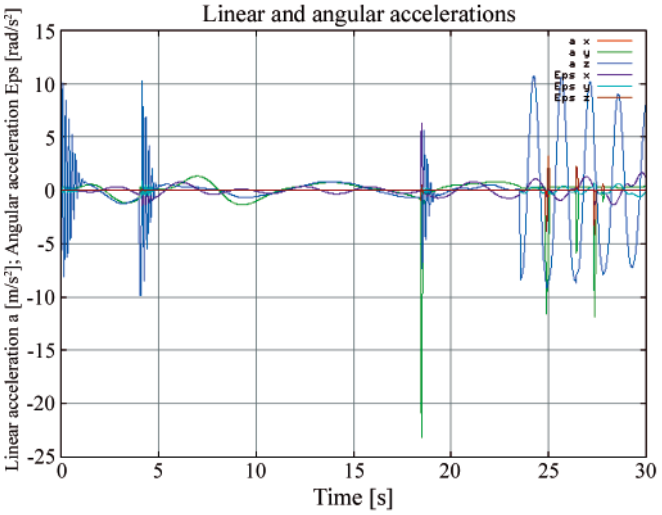


*Fig. 14. Linear and angular accelerations of the lifeboat*

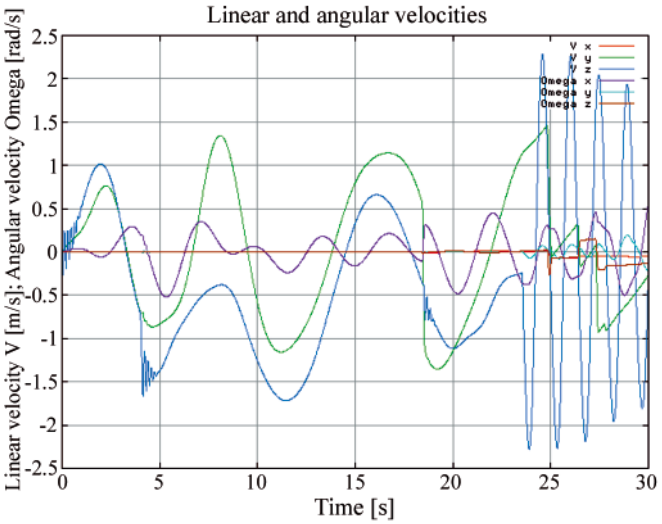


*Fig. 15. Linear and angular velocities of the lifeboat*

## DESCRIPTION OF RESULTS AND CONCLUSIONS

- The graphs in Fig. 6 and 11 show position of lifeboat's mass centre in the absolute coordinate system (x, y, z). The graphs in Fig. 8 and 13 show relative, linear and angular motions of the lifeboat in ship side's co-ordinate system. The graph G z B shows sway. During launching (lengthening the rope) we can notice increasing the period and amplitude of the motion. At about 18th second of launching process we observe impact of the lifeboat against ship side.
- The graphs in Fig. 7 and 10 show positions of unit vectors of the local lifeboat coordinate system in the absolute coordinate system.
- The graphs in Fig. 9 and 14 show linear and angular accelerations of the lifeboat. The blue ones (a_z) show vertical accelerations. The green ones show horizontal accelerations (a_y). At about 4th second we can notice start of lifeboat lowering, and at about 18th second - impact of the lifeboat against ship side.
- The graphs in Fig. 10 and 15 show linear and angular velocities of the lifeboat.
- The presented calculation results concern a typical launching operation of lifeboat for two cases which differ to each other with rope system only. The first case concerns the system equipped with an absorber and the other – that without absorber. In view of that the absorber works only under load in the rope greater than nominal one the courses of the functions are reliable and the differences between two presented cases are inconsiderable. In the graphs in Fig. 9 and 14 the main expected difference in lifeboat vertical accelerations can be observed. However it should be stressed that in the presented model elasticity of davit's structural elements was taken into account but their damping properties were neglected as to estimate them was difficult. If the properties are taken into account, then values of calculated accelerations will be lower, hence the difference between the acceleration courses for the two calculated cases will be smaller.
- The program in question is prepared for further development. It is possible to add elements for simulating more complex absorbers (e.g. dampers of longitudinal and transversal motions of the boat or drive and control systems for compensators). It could be useful in elaborating new systems.

**BIBLIOGRAPHY**


1. Kruszewski J., Ostachowicz W., Wittbrodt E.: *General mechanics* (in Polish). Politechnika Gdańska (Gdansk University of Technology). Gdańsk, 1993.
2. Von Karman Th.: *The impact on seaplane floats during landing.* Technical notes, National Advisory Committee for Aeronautics. Washington, 1929.
3. Dymarski P., Dymarski Cz.: *Safecrafts GUT_WP2_D2.3 – Report.* Gdańsk, 2006-04-07.


**CONTACT WITH THE AUTHORS**


Paweł Dymarski, Ph.D.
Prof. Czesław Dymarski
Faculty of Ocean Engineering
and Ship Technology,
Gdańsk University of Technology
Narutowicza 11/12
80-233 Gdańsk, POLAND
e-mail: cpdymars@pg.gda.pl

**POLISH MARITIME RESEARCH** 3(75) 2012 Vol 19; pp. 53-59
10.2478/v10012-012-0031-5

# Genetic algorithm for solving celestial navigation fix problems

**Ming-Cheng Tsou**, Ph.D.
National Kaohsiung Marine University, Taiwan

ABSTRACT

*As we enter the 21st century and advance further into the information age, traditional methods for computing a celestial navigation fix can no longer meet the requirements of modern vessels in terms of calculation speed and precision. Study of precise, rapid, and convenient celestial navigation computational methods and the application of information technology to modern celestial navigation is especially meaningful, considering the current push for e-Navigation. In this work, we employ a genetic algorithm, from the field of artificial intelligence, due to its superior search ability that mimics the natural process of biological evolution. Unique encodings and genetic operators designed in this study, in combination with the fix principle of celestial circles of equal altitude in celestial navigation, allow the rapid and direct attainment of accurate optimum vessel position. Test results indicate that this method has more flexibility, and avoids tedious and complicated computation and graphical procedures.*

**Key words**: genetic algorithm; celestial navigation; intercept method; celestial fix

## INTRODUCTION

Celestial navigation is one of the important positioning and navigation methods for ocean voyages due to its low cost, high reliability, strong independence, and inability to be detected. It is also one of the traditional navigational skills required of navigators by the International Maritime Organization (IMO). However, since 1994, the revolutionary Global Positioning System (GPS) has become widely available to the general public. GPS meets almost all of the requirements of seafarers, such as high precision, all weather functionality, automatic operation, and global coverage. This has resulted in the successive abandonment of other radio navigation systems (e.g. OMEGA, NNSS, DECCA, and LORAN A). The celestial navigation system, with its longstanding history, also faces a severe situation. However, while we enjoy the convenience that GPS has brought us, we are also exposed to the risks arising from our over-reliance on it. Navigation safety is endangered when satellite signals are cut off or interfered with, or when the satellite receiver system is broken; both situations render positioning of the vessel impossible. Even today, when navigation is dominated by GPS, a celestial fix still serves as an important backup measure. Nonetheless, as we enter the 21st century and advance into the information age, traditional methods for computing a celestial navigation fix can no longer meet the requirements of modern vessels in terms of calculation speed and precision.

At the Manila Conference hosted by the IMO in 2010, a new amendment regarding the Seafarers' Training, Certification, and Watchkeeping (STCW) Code was issued. The amendment describes e-Navigation as the focus of the development of navigation technology, and the application of information technology as a key direction of development. In addition, while celestial navigation received sustained emphasis in the Manila amendment, there is an explicit encouragement for the usage of electronic nautical almanacs and celestial navigation calculation software in Section B-II/1 of Chapter 2, "Guidance regarding the master and the deck department", which concerns training and competency requirements. This can be seen as an effort to lead the development of traditional celestial navigation gradually toward e-Navigation.

For these reasons, the study of high precision, rapid, and convenient celestial navigation computational methods and the application of information technology to modern celestial navigation is very meaningful. This work is based on the concept of the genetic algorithm from the field of artificial intelligence. It combines a search method that mimics the natural process of biological evolution with the celestial fix principle of circles of equal altitude to rapidly and directly obtain accurate optimum vessel position data. Test results show that in addition to avoiding tedious and complicated computation and graphical procedures, this method is also more flexible, and is consistent with the development trend of celestial navigation in the electronic and information age.

## DEVELOPMENT OF CONTEMPORARY CELESTIAL NAVIGATION TECHNOLOGY

The objective of celestial navigation, as traditionally practiced, is to determine the latitude and longitude of a vessel

at a specific time using observations of the altitudes of celestial bodies. This objective and the basic principles still remain unchanged today, and have formed a foundation on which a number of methods have been developed. The following is a review of the development of contemporary celestial navigation technology.

### *Intercept Method*

The intercept method, which is the oldest method, was developed in 1875 by Marcq de St. Hilaire. This method translates each celestial altitude observation into a line of position (LOP) on the surface of the Earth. In principle, a series of observations defines a group of intersecting LOPs and this intersection represents the observer's position the fix. Having been practiced for more than a hundred years, the intercept method is able to provide complete solutions for problems of astronomical vessel positioning. Its applicability continues in today's maritime education and training, and in merchant shipping practice. However, it is an approximate method and involves graphical procedures. The entire process consists of observing, calculating, and plotting. Even when performed by professional seafarers, one astronomical positioning will take around 20 minutes. Considering the high speed of modern vessels, this method fails to achieve real-time positioning, and the lag time in positioning cannot guarantee navigation safety. Moreover, there are two theoretical assumptions implied in the intercept method. One is that the azimuth at the observer's position with respect to the celestial body's geographical position is the same as the azimuth at the assumed position. The other assumption is that when the co-altitude is sufficiently large, the circle of position can be taken as line of position. In view of these assumptions, the accuracy of astronomical vessel positioning is subject to the following two restrictions:

1) As the choice of assumed position (AP) is by a trial-and-error method, its distance to the actual vessel position largely affects the accuracy of the result. Therefore, this distance should not exceed 30 NM.
2) The altitude of the celestial body should not exceed 70 degrees. Otherwise, the resulting error of curvature will increase when using line of position in lieu of circle of position on the Mercator Chart due to the reduced co-altitude.

Following the widespread application of information technology, some researchers applied the intercept method using computer programs. In Van Allen [13], the development is based on the geometry of the two LOPs. A least-squares approach for a multi-star fix is presented in Dewit [4] based on the plane geometry and straight lines formed by LOPs near the estimated position. This method is a direct mathematical translation of chart-based navigation. Although the intercept method has been computerized, the inherent drawbacks due to the two aforementioned assumptions still exist and limit its accuracy.

### *Spherical Triangle Method (STM) and Vector-Matrix Method*

With the aid of computer programs, problems that could not be solved previously using the inspection table can now be solved using the STM or Vector-Matrix methods. With these tools, the celestial fix becomes fast and accurate. Unlike with the intercept method, there is no limitation on accuracy. Either the assumed position is not needed or the knowledge of an approximate position is sufficient. Some researchers have studied a two-body fix [2, 3, 5, 6, 12, 14]. It is proposed that at a given time, the astronomical vessel position can be determined by observing circles of equal altitude of two celestial bodies. In a multi-body celestial fix, a statistical method such as the least mean squares technique is applied on the results of a number of two-body fixes to deal with the over-determined celestial fix problem and to solve for the final position [1]. However, in practice, it is rare to use two celestial bodies to obtain a vessel fix, and the statistical computation adds complexity to this method. Some other researchers have studied the multi-body celestial fix by invoking the circle of equal altitude. In this method, a celestial body's altitude is viewed as a function of latitude and longitude, and a multi-body celestial fix is carried out directly, using the vector-matrix method, instead of indirectly using results of a two-body fix [9, 11, 15]. The vector-matrix formulations, while elegant, have the disadvantage that the solution still assumes prior knowledge of the observer's position. Furthermore, the algorithm that proceeds from some initial value by sliding down the gradient of the goodness-of-fit parameter can converge to a local minimum that is not the best solution [7]. In addition, a multi-body celestial fix that is based on the least squares fit requires more than three celestial bodies. When there are only two celestial bodies available, this method cannot be used. In these cases, a virtual celestial body is introduced according to the vessel's dead reckoning position. Consequently, the accuracy is affected by the assumed vessel position.

## GENETIC ALGORITHM TO SOLVE FOR ASTRONOMICAL VESSEL POSITION

Advances in information technology have brought new changes to celestial navigation, especially in the early 1990s when research in this field blossomed. At this time, artificial intelligence began to be widely used in various research fields. Unfortunately, research on celestial navigation was soon largely replaced by the rapid emergence and development of GPS. At present, celestial navigation still serves as an important backup measure of vessel positioning in the ocean. It is therefore necessary to investigate the applications of information technology and artificial intelligence technology in celestial navigation and to improve the shortcomings of existing methods, which were described in the previous section.

### *General principle of GA*

In recent years, the development of artificial intelligence technology has enjoyed mutual influence with the life sciences. The flourishing of evolutionary computation methods, such as the genetic algorithm (GA), reflects this characteristic and development trend. GAs are among the most effective methods for optimization problems. All types of objective functions and constraints can be processed without many mathematical prerequisites. During the search process, knowledge of the search space can be automatically obtained and accumulated. Accordingly, the search is modified to solve for the optimal solution or a less suboptimal solution. This method is very efficient and enables a parallel search. Two main features of GAs are a search strategy in a population and the exchange of information between individuals in a population. It simulates the overall learning process involved in the creation of a population from individuals. Starting from an initial population, in which each individual is a candidate solution in the search space of an optimization problem, the fitness of each individual is evaluated based on a fitness function. Multiple individuals with better fitness are subsequently selected, and then modified through

genetic manipulations such as crossover (analogous to the exchange of information between individuals in nature) and mutation (where an individual is subjected to a sudden change and escapes the local optimum) to form a new population, thus achieving screening and evolution. The process is repeatedly executed. During the iteration process, every new population is superior to the population in the previous generation. Individuals continuously evolve toward better solutions, and eventually reach the optimum solution.

There is always complexity and uncertainty associated with a celestial fix, which makes it difficult to obtain the exact solution mathematically. In this study, the superior search ability of GA is combined with fundamental positioning principles in celestial navigation to perform a fitting calculation for the optimum vessel position.

## *The celestial fix principle of circles of equal altitude*

The central idea behind the celestial circle-of-equal-altitude fix is to find the best fit to the altitude of a celestial body observed as a function of time. The calculation altitude (Hc) of a celestial body is given as a function of the declination of body (Dec), the Greenwich hour angle (GHA), the observer's assumed longitude (λ), and the observer's assumed latitude (L) by:

$$\begin{aligned}\text{Sin Hc}_i &= \text{SinL} \times \text{SinDec}_i + \\ &+ \text{CosL} \times \text{CosDec}_i \times \text{Cos}(\text{GHA}_i - \lambda)\end{aligned} \tag{1}$$

where i = 1 to n represents the celestial body and the observation data of the $i^{th}$ celestial body

The GHA and the Dec can be found from the time of observation using the *Nautical Almanac* or the electronic edition of Nautical Almanac. Hc in Equation 1 is the calculated altitude, which differs from the actual observed altitude. The altitude of a celestial body (hs) is measured by a sextant. An instrumental error correction (I), index correction (IC), and correction for optical deviations such as dip and refractions are applied to the sextant altitude. The resulting value is the actual observed altitude (Ho). Since the actual vessel position can be seen as a function of the altitude of the celestial body, which is a nonlinear function of L and λ, we cannot solve equation 1 directly. Therefore, the latitude and longitude of the actual vessel position may be obtained from the difference between Hc and Ho using an appropriate fitting algorithm. With the appropriate Dec and GHA in equation 1, any combination of altitudes of one or several celestial bodies can be used, and no plots or tables are required. Furthermore, when performing the multi-body celestial fix, different observing times lead to inconsistency in the observed altitude. It is therefore necessary to make corrections on the running fix. In this study, the correction approach proposed by Kaplan [8] is adopted.

## *Implementation of a GA for the celestial fix problem*

The optimum vessel position in a majority of multi-body celestial fix problems is found by data fitting using the least mean squares method, and it is classified as an optimization problem. However, there still exists the problem of converging to a local minimum. GA shows excellent performance in optimum fix processing problems. Its main advantages include: (a) simple calculation without any complicated mathematical procedures; (b) it does not suffer from possible sensitivity to the initial position chosen to start the iterative process, meaning it has less of a tendency to converge toward the local optimum; (c) more flexibility in practice and rapid convergence toward the final result. The GA approach can be used to obtain a fix from multiple celestial observations of a single celestial body or of multiple celestial bodies (more observation data points produce better results). This method is in line with the needs of modern navigation. The procedure includes:

1) Design of the objective function: The first step in solving an optimization problem is the design of the objective function to evaluate the fitness of each individual. A GA is used in this study to minimize the root mean squares of the altitude residuals (equation 2, root mean square error – RMSE), defined as the difference between each observed altitude (Ho) and the altitude computed from equation 1 (Hc). The residual defined differs from the altitude difference normally used to plot LOPs since the altitude difference is referred to an assumed position chosen to permit table lookup of whole degrees of Local Hour Angle. When the RMSE converges to meet the acceptance criteria, the optimum vessel position is obtained.

$$\text{RMSE} = \min \sqrt{\frac{\sum_{i=1}^{n} (\text{Ho}_i - \text{Hc}_i)^2}{n}} \tag{2}$$

2) Design and encoding of individuals and population: In order to improve the efficiency and accuracy in this study, individual encodings in the GA are not in the form of traditional binary strings. Instead, real number encodings are adopted. Each individual contains two real number columns, representing latitude and longitude, to represent a possible solution (vessel position). Each population consists of multiple individuals. In generating the initial population, a reference position is introduced to improve search efficiency. This reference position is different from the assumed position in the intercept method. It is an approximate position of reference, which is not required to be within 30NM of the actual vessel position; indeed, it can be hundreds of nautical miles away. This permits a large degree of flexibility in choosing the reference position. This position is mainly a reference for a heuristic search. However, it is certain that a reference position closer to the actual position results in a smaller search space, resulting in higher efficiency and a better quality solution. The introduction of a new reference position does not add much inconvenience to seafarers. As stated by Pepperday [10], "If you know your approximate position. Why not use it?". In fact, methods that claim that no DR reference position is required still need to assume prior knowledge of the observer's position, or that it be obtained through complicated computational procedures. Moreover, DR position is also required for applying corrections on the running fix. The reference position is used as the datum point in this work. In the user defined maximum search degree and numbers of generations, random numbers are used to generate the initial position data of each individual in the initial population as the starting point of the evolution (equation 3, 4, 5):

$$\text{Data structure of each individual Di:} \begin{cases} \text{double latitude} \\ \text{double longitude} \end{cases} \tag{3}$$

$$\text{Data of every initial individual} \begin{cases} \text{IniL} + \text{Tol} \times \text{RandNum} \\ \text{Ini}\lambda + \text{Tol} \times \text{RandNum} \end{cases} \tag{4}$$

$$\text{Initial Population } (P_1) = \{D_{11}, D_{12}, D_{13}, D_{14}, ..., D_{1n}\} \quad (5)$$

where IniL and Iniλ represent the latitude and longitude values of the reference position, respectively. Tol is the user defined maximum search degree. RandNum is random real number between -1 and +1, and the random positions are generated to correct for the reference position. $P_1$ is the initial population, and n is the number of individuals in a population.

3) Selection: The traditional roulette method is adopted as the selection method. This is a proportional selection strategy. In this method, individuals with a higher fitness level have a better chance of being selected to generate the new population. This concept is used in GA to mimic biological evolution.
4) Crossover: The crossover rate is denoted as $P_c$. n individuals in the population are stochastically paired to form n/2 pairs. In order to determine in which pairs crossover takes place, the following procedure is repeated from i = 1 to n/2: Generate a random number r in the interval [0, 1], and if $r<P_c$, then apply crossover on the $i^{th}$ pair. The crossover proceeds according to equation 6 and 7:

$$D_{New}: \begin{cases} L_{New} = L_1 + |L_1 - L_2| \times RandNum \\ \lambda_{New} = \lambda_1 + |\lambda_1 - \lambda_2| \times RandNum \end{cases} \quad (6)$$

or:

$$D_{New}: \begin{cases} L_{New} = L_2 + |L_1 - L_2| \times RandNum \\ \lambda_{New} = \lambda_2 + |\lambda_1 - \lambda_2| \times RandNum \end{cases} \quad (7)$$

where $D_{New}$ represents new individuals generated through crossover. $L_{New}$ and $\lambda_{New}$ denotes the latitude and longitude of new individuals generated through cross. $L_1$, $\lambda_1$, $L_2$, $\lambda_2$ are latitude and longitude of the parent individuals on which crossover is applied. RandNum is random real number between -1 and +1, and they are used to generate more optimum random positions. The crossover step can bring new positions closer (as shown in Figure 1) or further away (as shown in Figure 2). Since the parent individuals are already individuals with better fitness, it is more likely for the newly generated individuals to have further improvement (more closer to the actual vessel position).

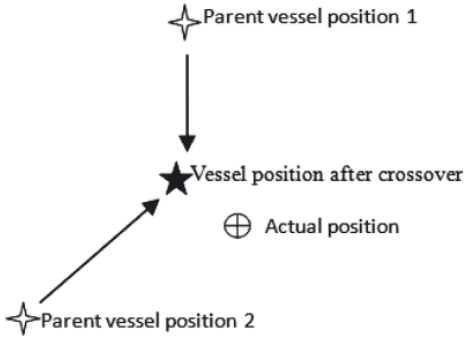


***Fig. 1.*** *Position becomes closer after crossover*

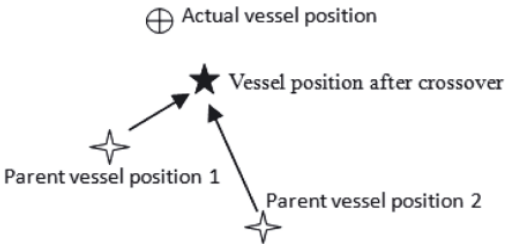


***Fig. 2.*** *Position becomes further away after crossover*

5) Mutation: The mutation rate is defined as $P_m$. The following procedure is repeated on individual i = 1 to n: Generate a random number r in the interval [0, 1], and if $r < P_m$ then apply the mutation operation according to:

$$D_{Mutation}: \begin{cases} L_{Mutation} = L_{Old} + Noise \times RandNum \\ \text{or} \\ \lambda_{Mutation} = \lambda_{Old} + Noise \times RandNum \end{cases} \quad (8)$$

$D_{Mutation}$ represents the data of individuals after mutation. $L_{Mutation}$ and $\lambda_{Mutation}$ represent the latitude and longitude of individuals after mutation. $L_{Old}$ and $\lambda_{Old}$ represent the latitude and longitude of individuals before the mutation. Noise is a user defined degree of allowable perturbation, in place for starting new research. RandNum is random real number between -1 and +1, and these numbers are used to generate the stochastic perturbation degree. The mutation operation can prevent the search from converging to the local optimum (as shown in Figure 3).

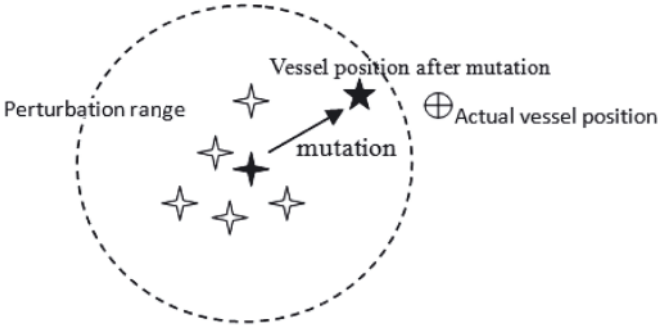


***Fig. 3.*** *Mutation prevents the search from converging to the local optimum*

6) Improvement of the efficiency of the GA: In some cases, individuals in the population become increasingly similar to each other during the evolutionary process, thus limiting the GA's global search ability, and causing the GA to converge toward a local optimum instead of the global optimum. To avoid this, we have enhanced the global search ability of the GA in the current study. At the early stage of evolution, a large crossover rate and mutation rate are imposed in order to maintain diversity in the population. At the later stages of evolution, individuals have already developed to a near optimal state. At this time, a large crossover rate or large mutation rate are likely to impair individual fitness. Therefore, the crossover rate and mutation rate are reduced at the later stages.

## *Procedures of implementation*

Although a large population size is helpful in the search of vessel position, it inevitably increases the search time, making it difficult to use for real time positioning. In the current study, the population size is set at 50 individuals. The crossover rate and mutation rate are 0.6 and 0.05, respectively. The maximum search space is set to 2 degrees (i.e. 4 degrees in latitude and longitude), which is sufficient for navigation. The perturbation range is set to 1 degree. Applying these settings in the genetic operations creates new generations to replace the parent generation. The search is terminated when either the RMSE converges to the acceptance criteria, or a fixed number of generations is reached. Termination of the search indicates that the optimal vessel position has been obtained. Experiments show that convergence to the accurate position generally occurs within 50 generations, and within approximately 5 seconds.

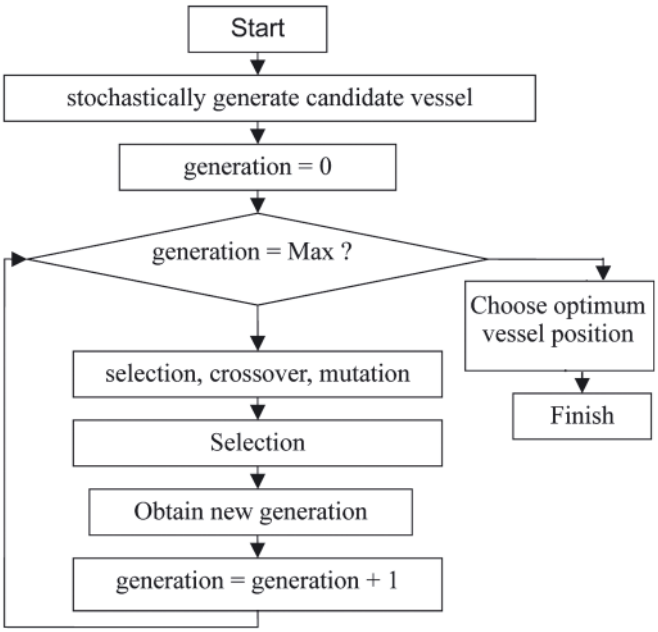


***Fig. 4.*** *The flowchart of GA for obtaining the optimum vessel position*

This satisfies the requirement of real-time positioning. The step-by-step procedures are (refer to Figure 4):

1) Use real numbers to encode individuals in the solution space. Each individual corresponds to a candidate vessel position.
2) Set the initial population size to contain 50 individuals, i.e. stochastically generate 50 candidate vessel positions.
3) Calculate the value of the fitness function of each individual according to equation (1) and (2), and determine which individuals in the population are relatively close to the actual vessel position.
4) Select individuals close to the actual vessel positions using the roulette technique.
5) Apply crossover to the population. Crossover between vessel positions with good fitness generates vessel positions that are closer to the optimal positions.
6) Apply genetic mutation to the population to avoid converging to local optima instead of the global optimum.
7) Re-calculate the value of the fitness function of each individual according to equations (1) and (2).
8) Determine whether the termination criteria has been met. If yes, then the genetic operation ends and proceeds to step (9), where the current optimum vessel position is exported. Otherwise, move back to step (4).
9) Export the optimum vessel position.

## RESULT VALIDATION

The validity of this study is verified by comparing results of a two celestial body fix and a multiple celestial body fix with those obtained by other methods. Visual Basic.Net 2010 is used as the development tool. In order to add visual effects, components of Geographic Information System (GIS) are also introduced. This is also aimed at future celestial navigation education and integration with an Electronic Chart Display and Information System (ECDIS).

***Tab. 1.*** *Comparison of GA and relevant information from Hsu et al. [6] for two-body fix*

| Body | ZT | Ho | GHA | Dec |
|---|---|---|---|---|
| Capella | 20-03-58 | 15°19.3’ | 131°24.8’ | 45°58.4’ N |
| Alkaid | 20-02-56 | 77°34.9’ | 003°14.2’ | 49°25.7’ N |
| DR (20-04-00) | L = 41°34.8’ N | λ = 017°00.5’ W | | |
| Intercept Method | L = 41°38.6’ N | λ = 017°08.1’ W | | |
| SEEM | L = 41°39.1’ N | λ = 017°07.3’ W | | |
| GA | L = 41°39.1’ N | λ = 017°07.3’ W | | |

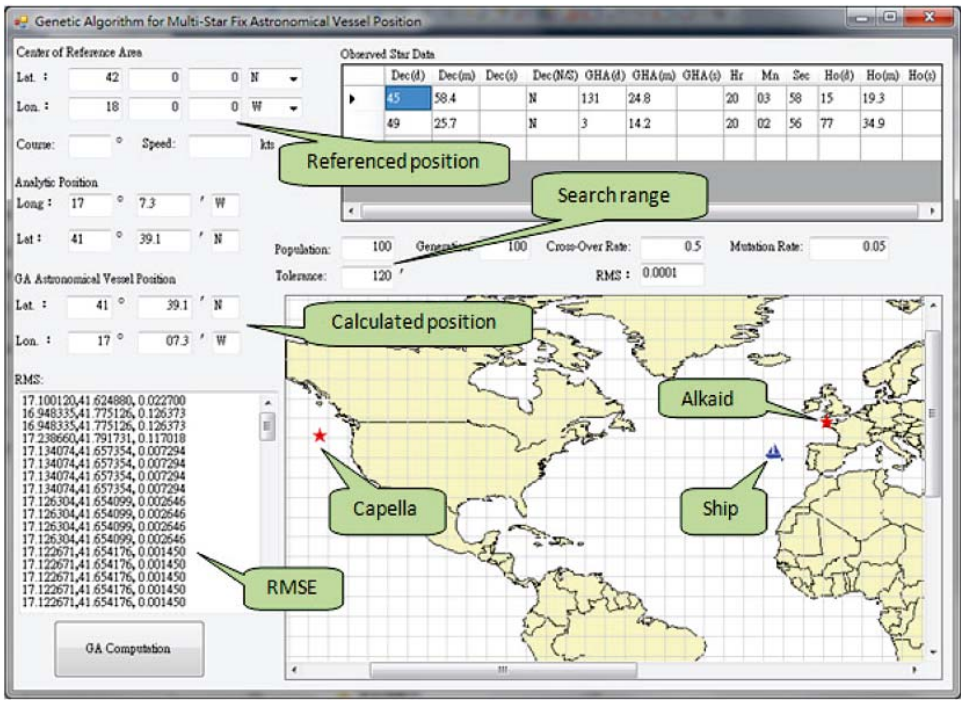


***Fig. 5.*** *GA of two-body celestial fix*

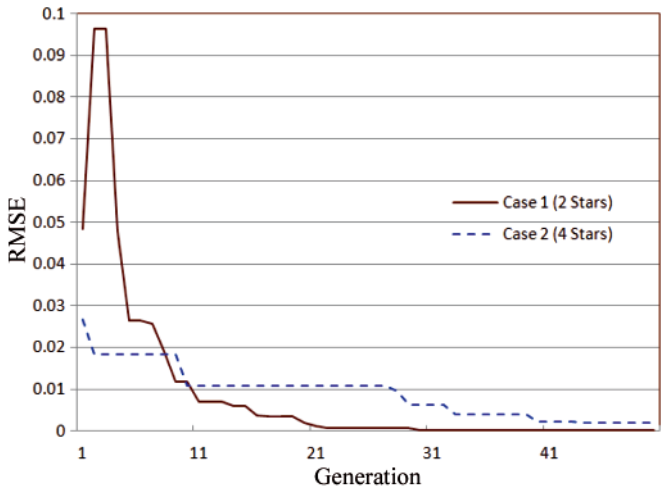


*Fig. 6. The evolutionary process for calculation of a fix*

**Case 1 - Two-Body Fix:** The data in this case study is taken from Hsu et al. [6]. The authors used the Simultaneous Equal-altitude Equation Method (SEEM) to perform a two-body celestial fix. Table 1 contains relevant experiment data.

It can be seen from Table 1 that the observed altitude of Alkaid is as high as 77°34.9', which exceeds the upper limit of 70° of the intercept method. Hsu et al. [6] found that the LOP drawn using the intercept method shifted due to curvature error, thus resulting in an inaccurate vessel position estimate.

The present study however is free from this drawback. In our experiments, even if the distance between the reference position and the actual vessel position exceeds 30NM and the search degree reaches 4°×4° (refer to Figure 5), the correct vessel position can still be obtained. Moreover, the RMSE converges to 0.0001 within 30 generations and within 3 seconds (refer to Case 1 in Figure 6). The calculation is performed in a rapid and accurate manner without the need to construct a visual celestial body.

**Case 2 - Multi-body Fix**: There are four celestial bodies involved in this case study and more realistic in real marine navigation situation. Table 2 presents relevant observational data. In addition to the increased number of celestial bodies, correction on the running fix is also applied. The parameters in this experiment are in general identical to those in the previous case. However, the reference position is deliberately placed further so that it is almost 2 degrees away from the actual vessel position. Though the final RMSE (about 0.002) is slightly bigger than Case 1, caused by observation errors from multi-star sights, it can converge within 50 generations (refer to Case 2 in Figure 6). Results of this experiment show a good agreement with those obtained by the vector-matrix method or the graphical intercept method (refer to Figure 7 and Figure 8). No plots or sight reduction tables are needed. The running time is within 5 seconds, and can meet the demands of real-time navigation fix. The applicability of the GA approach for both the two-body fix and multi-body fix is thus verified.

*Tab. 2. Multi-body fix*

| Body | ZT (1993/9/13) | Ho | GHA | Dec |
|---|---|---|---|---|
| Altair | 18-00-00 | 37°53.0' | 325°06.6' | 08°51.4' N |
| Fomalhaut | 18-04-00 | 27°54.0' | 279°24.2' | 29°39.1' S |
| Achernar | 18-08-00 | 17°46.5' | 240°21.7' | 57°15.8' S |
| Rasalhague | 18-12-00 | 41°35.5' | 002°04.8' | 12°34.1' N |
| DR | L = 35°13.0' S λ = 005°20.0' E Course = 220° Speed = 18 kts | | | |
| Intercept Method | L = 35°19.0' S λ = 005°26.5' E | | | |
| Vector-Matrix | L = 35°18.6' S λ = 005°26.9' E | | | |
| GA | L = 35°18.6' S λ = 005°27.0' E | | | |

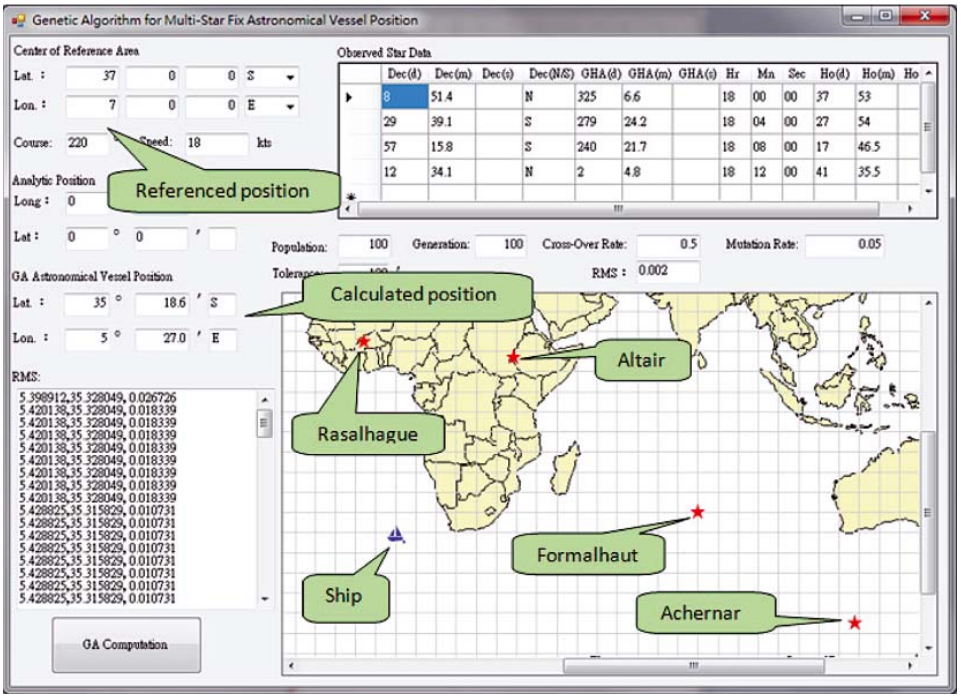


*Fig. 7. GA of multi-body celestial fix*

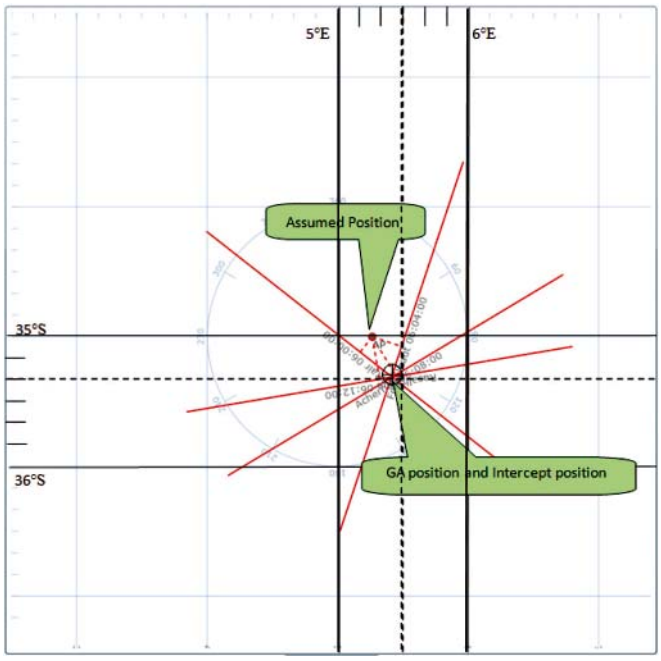


***Fig. 8.*** *Comparison of GA and intercept method in multi-body celestial fix*

## CONCLUSIONS

Although celestial navigation has its shortcomings, it cannot be replaced by GPS due to the advantages of low cost, high reliability, strong independence, and inability to be detected. In this study, a genetic algorithm that mimics biological evolution, taken from the field of artificial intelligence, is applied to the celestial navigation fix problem. The main features of the GA include: (1) simple calculation without any complicated mathematical procedures; (2) Avoidance of converging toward a local optima; (3) more flexibility in practice and rapid convergence toward the final position estimate. The algorithm can be used to obtain a fix from observation of a single celestial body (multiple observations) or of multiple celestial bodies, and more observation data produces better results. Experimental results show that in addition to evading tedious and complicated computation and graphical procedures, the GA approach is more flexible compared with other methods. This approach also has the potential to be integrated with ECDIS. Moreover, it can also be used to confirm whether GPS is functioning normally. Navigation technology is moving into the age of e-Navigation, and the continuous development of celestial navigation can only be realized through integration with information technology.

## BIBLIOGRAPHY

1. Chen C.-L., Chang J.-R., Hsu T.-P.: *A New Computation Method to Solve the LOP Without the Intercept* (In Chinese). Maritime Research Journal, 2003, 15, 77-93.
2. Chen C.-L., Hsu T.-P., Chang J.-R.: *A Novel Approach to Determine the Astronomical Vessel Position*. Journal of Marine Science and Technology, 2003, 11, 221-235.
3. Chiesa A., Chiesa R.: *A Mathematical Method of Obtaining an Astronomical Vessel Position*. The Journal of Navigation, 1990, 43, 125-129.
4. Dewit C.: *Optimal Estimation of a Multi-Star Fix*. *NAVIGATION,* Journal of The Institute of Navigation, 1974, 21, 320-325.
5. Gibson, K.: *On the Two-Body Running Fix*. *The Journal of Navigation*, 47, 103-107, 1994.
6. Hsu T.-P., Chen C.-L., Chang J.-R.: *New Computation Methods for Solving Problems of the Astronomical Vessel Position*. The Journal of Navigation, 2005, 58, 315-335.
7. Kaplan G. H.: *Determining the Position and Motion of a Vessel from Celestial Observations*. *NAVIGATION,* Journal of The Institute of Navigation, 1996, 42, 631-649.
8. Kaplan G. H.: *The Motion of the Observer in Celestial Navigation*, Online Information for the Defense Community, 1996, (Available online at http://www.dtic.mil/cgi-bin/GetTRDoc?Location = U2&doc = GetTRDoc.pdf&AD = ADA423226)
9. Metcalf T. R., Metcalf, F. T.: *On the Overdetermined Celestial Fix*. *NAVIGATION,* Journal of The Institute of Navigation, 1991, 38, 79-89.
10. Pepperday M.: *The 'Two-Body Problem' At Sea*. The Journal of Navigation, 1992, 45, 138-142.
11. Severance R. W.: *Overdetermined Celestial Fix by Iteration*. NAVIGATION, Journal of The Institute of Navigation, 1989, 36, 373-378.
12. Spencer B.: *Astronomical Fixes Without an Assumed Position*. The Journal of Navigation, 1990, 43, 449-451.
13. Van Allen, J. A: *An Analytical Solution of the Two Star Sight Problem of Celestial Navigation*. Journal of The Institute of Navigation, 1981, 28, 40-43.
14. Vulfovich B., Fogile V.: *New Ideas for Celestial Navigation in the Third Millennium*. The Journal of Navigation, 2010, 63, 373-378.
15. Wu G.: *An Optimal Estimating Method for Celestial Navigation*. The Journal of Navigation, 1991, 44, 266-269.

### CONTACT WITH THE AUTHOR

Ming-Cheng Tsou, Ph.D.
National Kaohsiung Marine University, Taiwan
e-mail: d86228006@yahoo.com.tw

**POLISH MARITIME RESEARCH** 3(75) 2012 Vol 19; pp. 60-64
10.2478/v10012-012-0032-4

# Information unfitness as a factor constraining Automatic Identification System (AIS) application to anti-collision manoeuvring

**Andrzej Felski**, Prof.
**Krzysztof Jaskólski**, M.Sc.
Naval Academy of Gdynia, Poland

ABSTRACT

*Common use of shipboard AIS creates conditions for the use of a new kind of dynamic data in the situation of the risk of collision. AIS position report is a source of supplementary information derived from error leveraged radar measurement. However, in view of the results of the studies there are opinions with regard to inconsistent AIS dynamic data in the process of decision-making by the officer of the watch. By taking into consideration the recordings of the studies and technical specification of AIS it can be concluded that the results of inconsistent data have significant role in collision avoidance manoeuvring.*

**Key words**: AIS; collision avoidance

## INTRODUCTION

According to International Regulations for Preventing Collisions at Sea, Rule V "Look-out" [7] „*Every vessel shall at times maintain a proper look-out by sight and hearing as well as by all available means appropriate in the prevailing circumstances and conditions so as to make a full appraisal of the situation and of the risk of collision*". Effective look-out should ensure early detection of objects. Another problem is to assess ship motion parameters and foresight situation. One of the effective undertakings is radar look-out in any conditions of visibility, especially, when the vessel navigates in area of intensity traffic or at night. It is common knowledge that Radar and ARPA have some efficacy limitations [8]. Detection of small objects is limited by sea clutters and unfavourable weather conditions (rain, snowstorm), and by close frequency working radio-transmitters.

Characteristic phenomenon is death-zone appearance (minimum range of detection), radar shadow effect (there are reflections from funnel, mast and other constructions on the vessel) and wave reflection. The radar information, usually presented in polar coordinates system is subject to some measurement error exceeding approximately 1% of radar range. As far as ARPA devices are concerned, automatic tracking objects can be lost during torrential ship manoeuvring or when passing ships within close distance. Therefore it is reasonable to supplement the information derived from radar with additional information delivered automatically and continuously with better accuracy. A system which appears suitable to provide this kind of information is AIS which may be classified as radio navigation system which uses radio waves to transmit data with regard to the ship motion parameters. This information is more accurate than radar information, however for many sea officers it looks less reliably than own radar information.

## QUALITY OF AIS INFORMATION

To illustrate AIS information with respect to the movement of objects in the operation area of the system the following elements of the „Position Report" containing the AIS messages 1, 2 and 3, namely:

- SOG,(Speed over ground);
- ROT,(Rate of turn);
- HDG, (Heading);
- geographic position;
- time stamp;

can be used.

Dynamic information has been used in the calculations performed by MADSS (Multi-agents Decision Support System), described by [2]. On the basic of received messages AIS calculates ship motion parameters and generates new motion parameters of own vessel (course, speed), which leads to pass by one another depending on calculated CPA (Closest Point of Approach).

Common use of AIS caused the emergence of the opinion on the imperfections of the system related to the lack of transmission or the transfer of not reliable information. Studies on the incompleteness and integrity of AIS information published to date are generally linked to the message No. 5

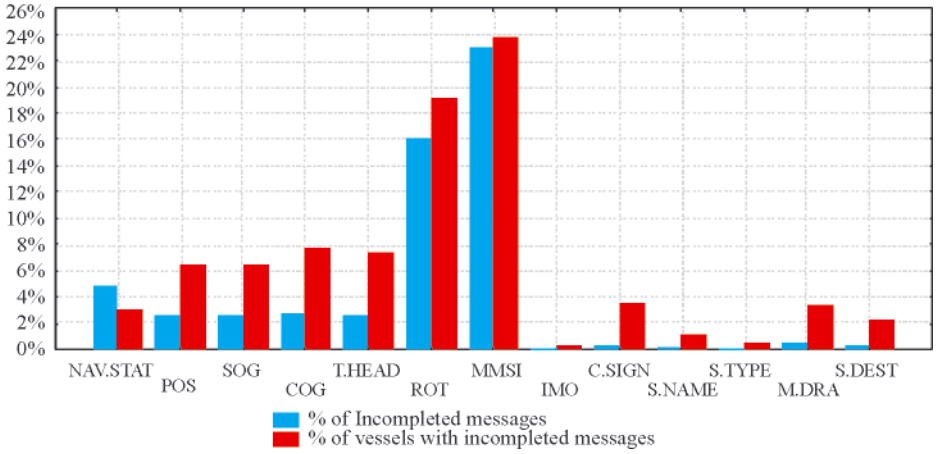


***Fig. 1.*** *Initial results of incomplete AIS information [acc. these authors' studies].* ***Abbreviations****:* ***NAV.STAT*** *– Navigational status;* ***POS*** *– Coordinates of ship's position;* ***SOG*** *– Speed over ground;* ***COG*** *– Course over ground;* ***T.HEAD*** *– true heading;* ***ROT*** *– Rate of turn;* ***MMSI*** *- Maritime Mobile Service Identity number of the ship;* ***IMO*** *– Ship's IMO number;* ***C.SIGN*** *– Ship's call signal;* ***S.NAME*** *– Ship's name;* ***S.TYPE*** *– Type of the ship;* ***M.DRA*** *– Mean draft of the ship;* ***S.DEST*** *– Destination of the ship;*

(Static & voyage related data). This problem was also analysed by [4] and [1, 3, 5, 6]. However, it seems that there are no publications concerning quality of the dynamic information, particularly the one which is important in the analysis of anti-collision maneuvering. In addition mentioned publications has been prepared in the beginning stage of AIS. In view of this facts, an initial investigation has been conducted by authors to determine to what extent the information transmitted by AIS and derived from ship sensors is complete.

## INITIAL INVESTIGATION OF THE AIS DYNAMIC INFORMATION INCOMPLETENESS

Completeness of the messages No. 1, 2, 3 based on analysis of contents of the messages AIVDM has been studied. Analysed data originate from the Gulf of Gdańsk and contain recorded information of AIVDM mnemonic from 2006.04.12, at 00.00 to 2006.04.12, at 23.59. The results of the studies are presented in Figure 1. Dark grey bar shows the percentage of messages which contain incomplete information, and the light grey bar shows the percentage of vessels responsible for this state.

The AIS information studies were based on recorded messages in text files containing the messages (received by AIS) about vessels located in the Gulf of Gdańsk during one day only. Preliminary analysis of the results leads to the conclusion that the biggest indicator of unfitness is characterised by information about the rate of turn which seems to be very important for anticollision activity. Incompletness of messages is at the level of 23%. These messages were sent by 24% of ships, approximately. Additionally, it is worth to noting the incompleteness of information concerning True Heading, which amounts about 6% and was observed in the case of 19% of vessels. Therefore, there is a reason to perform detailed studies on the incomplete information concerning True Heading and Rate of Turn.

## STUDIES OF INCOMPLETENESS OF SELECTED ELEMENTS OF AIS DYNAMIC INFORMATION

On the basis of technical specification, AIS correct statement of data concerning volume and value of the incomplete information are shown in Tab. 1.

According to the assumptions, detailed studies of dynamic information has been performed in 2010 and 2011 in selected 49 days. Data has been recorded with shore receiver situated in the building of Polish Naval Academy in Gdynia. Information about True Heading and Rate of Turn characterise the biggest information unfitness like in 2006 preliminary study. Summary of this are presented in Tab. 2.

***Tab. 1.*** *Summary of the ranges of correct and incorrect data in the message No 1*

| Type of information | Correctly value | Incomplete information |
|---|---|---|
| TRUE HEADING | [0.359] | 511 (149 hex) |
| RATE OF TURN | ±127 | 128 (80 hex) |

Figure 2 presents summary of the studies concerning AIS information unfitness, and takes into consideration

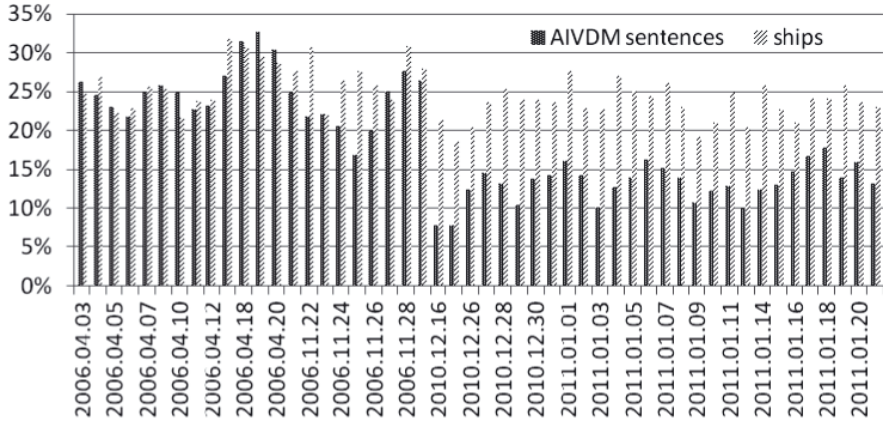


***Fig. 2.*** *Summary of unfitness studies of AIS information concerning Rate of turn [acc. these authors' studies]*

***Tab. 2.*** *Summary of unfitness studies concerning True heading and Rate of turn [acc. these authors' studies]*

| Date | TRUE HEADING [%] | | RATE OF TURN [%] | |
|---|---|---|---|---|
| | incompleteness (AIVDM sentences) | unfitness (ships) | incompleteness (AIVDM sentences) | unfitness (ships) |
| 2006.04.03 | 18.40 | 20.73 | 26.21 | 24.70 |
| 2006.04.04 | 17.68 | 22.83 | 24.58 | 26.77 |
| 2006.04.05 | 16.57 | 20.00 | 22.97 | 22.18 |
| 2006.04.06 | 15.25 | 18.95 | 21.78 | 22.88 |
| 2006.04.07 | 17.96 | 19.81 | 24.90 | 25.60 |
| 2006.04.08 | 17.65 | 21.50 | 25.69 | 25.26 |
| 2006.04.10 | 18.85 | 18.41 | 24.91 | 21.53 |
| 2006.04.11 | 16.27 | 19.11 | 22.75 | 23.82 |
| 2006.04.12 | 16.00 | 17.65 | 23.07 | 23.98 |
| 2006.04.13 | 17.81 | 24.27 | 26.98 | 31.80 |
| 2006.04.18 | 21.60 | 21.16 | 31.53 | 30.71 |
| 2006.04.19 | 20.45 | 22.26 | 32.70 | 29.38 |
| 2006.04.20 | 19.92 | 20.33 | 30.37 | 28.65 |
| 2006.04.21 | 19.71 | 20.78 | 24.80 | 27.68 |
| 2006.11.22 | 22.37 | 26.67 | 21.83 | 30.67 |
| 2006.11.23 | 19.93 | 25.77 | 21.99 | 21.99 |
| 2006.11.24 | 21.42 | 25.26 | 20.59 | 26.32 |
| 2006.11.25 | 14.62 | 24.47 | 16.81 | 27.66 |
| 2006.11.26 | 14.61 | 20.43 | 19.92 | 25.81 |
| 2006.11.27 | 16.21 | 20.45 | 24.97 | 23.86 |
| 2006.11.28 | 17.75 | 24.18 | 27.61 | 30.77 |
| 2006.11.29 | 20.94 | 23.26 | 26.45 | 27.91 |
| 2010.12.16 | 7.69 | 21.37 | 7.80 | 21.37 |
| 2010.12.17 | 7.81 | 18.56 | 7.81 | 18.56 |
| 2010.12.26 | 11.82 | 19.47 | 12.41 | 20.35 |
| 2010.12.27 | 14.97 | 23.62 | 14.57 | 23.62 |
| 2010.12.28 | 15.25 | 26.12 | 13.20 | 25.37 |
| 2010.12.29 | 10.97 | 23.88 | 10.37 | 23.88 |
| 2010.12.30 | 14.58 | 24.79 | 13.74 | 23.97 |
| 2010.12.31 | 14.59 | 25.21 | 14.15 | 23.53 |
| 2011.01.01 | 16.13 | 28.57 | 16.09 | 27.62 |
| 2011.01.02 | 14.26 | 24.56 | 14.22 | 22.81 |
| 2011.01.03 | 10.93 | 24.55 | 10.11 | 22.73 |
| 2011.01.04 | 12.86 | 27.83 | 12.70 | 26.96 |
| 2011.01.05 | 14.05 | 25.89 | 13.87 | 25.00 |
| 2011.01.06 | 17.07 | 26.09 | 16.23 | 24.35 |
| 2011.01.07 | 15.34 | 27.83 | 15.14 | 26.09 |
| 2011.01.08 | 14.64 | 24.59 | 13.96 | 22.95 |
| 2011.01.09 | 12.80 | 20.80 | 10.69 | 19.20 |
| 2011.01.10 | 14.94 | 22.58 | 12.21 | 20.97 |
| 2011.01.11 | 15.52 | 26.40 | 12.88 | 24.80 |
| 2011.01.12 | 10.08 | 21.30 | 9.91 | 20.37 |
| 2011.01.14 | 12.51 | 27.62 | 12.33 | 25.71 |
| 2011.01.15 | 14.89 | 24.53 | 12.95 | 22.64 |
| 2011.01.16 | 15.79 | 22.86 | 14.61 | 20.95 |
| 2011.01.17 | 17.01 | 25.00 | 16.62 | 24.14 |
| 2011.01.18 | 17.38 | 24.07 | 17.75 | 24.07 |
| 2011.01.19 | 13.99 | 26.61 | 13.90 | 25.69 |
| 2011.01.20 | 13.25 | 23.58 | 15.88 | 23.58 |
| 2011.01.21 | 9.12 | 21.88 | 13.21 | 22.92 |

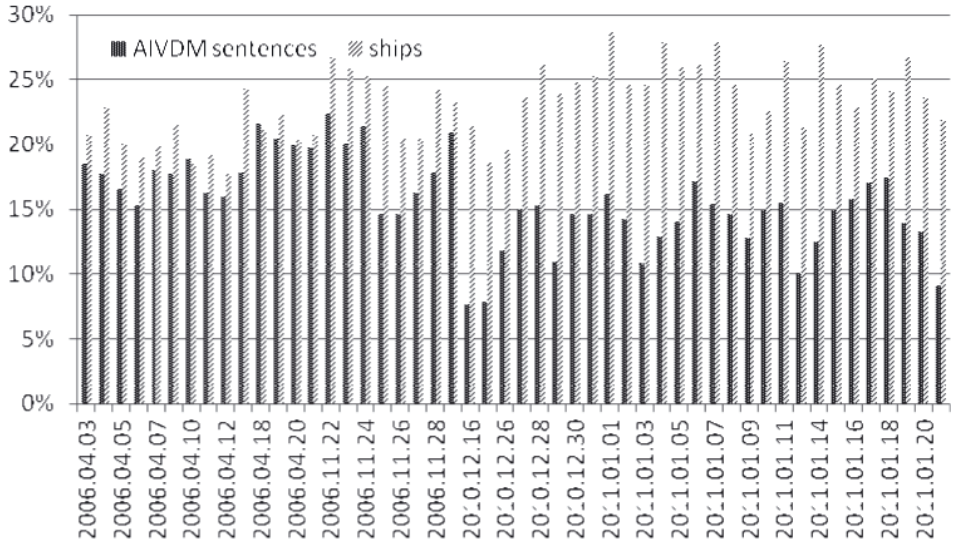


***Fig. 3.*** *Summary of the studies on unfitness of AIS information concerning True Heading [acc. these authors' studies]*

incompleteness of Rate of Turn. The Dark grey bar presents percentage of incomplete messages concerning Rate of Turn, whereas the light grey bar presents percentage of ships, which are responsible for this state.

Figure 3 presents results of the incompleteness studies of AIS information concerning True Heading. As previously mentioned, dark grey bar presents percentage of incomplete messages, whereas the light grey bar presents percentage of ships, which are responsible for this state.

Taking into consideration the investigations performed in 2010 and 2011, only an imperceptible decrease of HDG and ROT coefficients with "AIVDM sentences" criterion is observed. The analysis of the results is presented in Tab. 3.

***Tab 3.*** *Analysis of the studies on AIS information unfitness, gained in the period from 2006.04.03 to 2006.11.29*

| | TRUE HEADING | | RATE OF TURN | |
|---|---|---|---|---|
| | **Sentences (AIVDM)** | **ships** | **Sentences (AIVDM)** | **Ships** |
| $\overline{x}$ | 18.27% | 21.74% | 24.70% | 26.36 % |
| $m_e$ | 17.89% | 20.97% | 24.85% | 26.07% |
| max | 22.37% | 26.67% | 32.70% | 31.80% |
| min | 14.61% | 17.65% | 16.81% | 21.53% |
| σ | 2.25% | 2.46% | 3.68% | 3.03% |
| $\sigma^2$ | 0.05% | 0.06% | 0.14% | 0.10% |

$m_e$ - median, x - arithmetic mean,
σ - standard deviation, $\sigma^2$ - variance

***Tab. 4.*** *Analysis of the studies on AIS information unfitness, gained in the period from 2010.12.16 to 2011.01.21*

| | TRUE HEADING | | RATE OF TURN | |
|---|---|---|---|---|
| | **Sentences (AIVDM)** | **ships** | **Sentences (AIVDM)** | **Ships** |
| $\overline{x}$ | 13.58% | 24.29% | 13.19% | 23.36% |
| $m_e$ | 14.42% | 24.56% | 13.48% | 23.60% |
| max | 17.38% | 28.57% | 17.75% | 27.62% |
| min | 7.69% | 18.56% | 7.80% | 18.56% |
| σ | 2.59% | 2.49% | 2.42% | 2.21% |
| $\sigma^2$ | 0.07% | 0.06% | 0.06% | 0.05% |

$m_e$ - median, x - arithmetic mean,
σ - standard deviation, $\sigma^2$ - variance

The essential percentage of misinformation about the Heading and Rate of Turn observed during investigations demands further explanations. One of reasons can be the frequent lack of measures of ROT on smaller ships. The other sources can be moored ships with active gyro, what can give the effect of misinformation about the Heading. Possible source of unfitted information about HDG can be some problems with connection between gyro and AIS device. Interesting is observation that different strategies of investigations gives us different results. For example mean value of wrong information about ROT is 13% or 23% - depends the name of ship is analyzed or type of AIS sentence. This leads to the conclusion that probably some ships without sources of ROT be present in analyzed radius more times than another.

## CONCLUSION

- Potential application of AIS information for anti-collision manoeuvres seem to be promising however concerning True Heading and Rate of Turn data transmitted by this system rises a number of questions among practitioners. The question is why so many times information about HDG is unfitted. Suggestion is that there are some technical problems with connection between gyro and AIS device.
- During presented studies two approaches have been applied. The unfitness rate was based on analysis of messages in the system and on the number of ships transmitting this messages. The arithmetic means of statistical features take similar values. The variance of data reveals their high variability characteristics of the study and the incompleteness of Rate of turn is at the level of 15.89% (Tab. 3). The variance of random variables provides information about their low dispersion. It is worth noting that the sample taken for testing was gained only from the Gulf of Gdańsk, and the number of statistical units gives only a general view of the information unfitness during anti-collision manoeuvring. Conclusion about possible using AIS information for anti-collision tasks is that more reliable is information about course over ground transmitted by the ship than her heading.

**BIBLIOGRAPHY**

1. Bailey N., *Training, technology and AIS: Looking Beyond the Box*, Proceedings of the Seafarers International Research Centre's, 4th International Symposium Cardiff University, pp. 108-128, 2005.
2. Banachowicz A., Wołejsza P., *Calculation Accuracy of Safe Course Made Good in an anticollision system*, Scientific Bull. of Szczecin Maritime Academy, Szczecin, Transportation problems, 2008.
3. Drozd W., Dziewicki M., Waraksa M., Bibik Ł, *Operational status of Polish AIS network, Advances in marine navigation and safety of sea transportation*, 7th International Symposium TransNav. Gdynia Maritime Academy, pp. 195-198, Gdynia, 2007.
4. Harati-Mokhtari A., Wall A., Brookes P., Wang J., *AIS Contribution in Navigation Operation-Using AIS User Satisfaction Model,* 7th International Symposium TransNav. Gdynia Maritime Academy, pp. 187-193, Gdynia, 2007.
5. Harati-Mokhtari A., Wall A., Brookes P., Wang J., *Automatic Identification System (AIS): A Human Factors Approach,* Journal of Navigation 2007, Cambridge University Press, 2007. at http://www.nautinst.org/ais/PDF/AIS_Human_Factors.pdf, dostęp 04.06.2010
6. Hori A., Arai Y., Okuda S., Fujie S., *Reliability and Availability on Onboard AIS Information*, Proceedings of the Conference IAIN 2009, Stockholm, 2009.
7. Rymarz W., *The Manual of International Regulations for Preventing Collisions at Sea*, Trademar, (in Polish) Gdynia, 1998.
8. Sniegocki H., *Errors in the presentation of vessel course and speed for the VTS operator*. Annual of Navigation no. 4, Gdynia 2002.
9. *Draft Revision of Recommendation ITU-R.M.1371, Technical characteristics for a universal shipborne automatic identification system using time division multiple access in VHF maritime mobile band, Radiocommunication study Groups*, International Telecommunication Union, 1998.

**CONTACT WITH THE AUTHORS**

Andrzej Felski, Prof.
Krzysztof Jaskólski, M.Sc.
Institute of Navigation and Hydrography,
Polish Naval Academy
Śmidowicza 69
81-103 Gdynia POLAND
e-mail: a.felski@amw.gdynia.pl

**POLISH MARITIME RESEARCH** 3(75) 2012 Vol 19; pp. 65-71
10.2478/v10012-012-0033-3

# The effects of matrix module structure on shipyard panel line's throughput

**Murat Ozkok**, Ph.D.
Karadeniz Technical University, Trabzon, Turkey

ABSTRACT

*Over the last decades a really tough competitive environment has been observed in shipbuilding sector. Under these circumstances shipyards desire to reduce product cycle time in order to manufacture the product as soon as possible. For this reason it is required to make some alterations in shipyard production system in order to reduce cycle time. In this study a panel fabrication line used in a shipyard, has been considered. The workstations of the panel line have been modeled by using ARENA simulation software and the effects of matrix module assembly on panel line throughput, have been determined.*

**Key words:** shipyard; ship production; panel line; matrix module assembly; simulation

## INTRODUCTION

In recent years there is a hard competitive environment in many industry branches including shipyard industry. In order to increase their competitiveness shipyards have to consider the factors affecting competitiveness according to Rashwan and Naguib [1]. One of the factors is delivery time. To be able to keep the competitive power, the companies have to deliver the products to their customers on time and reduce the production cycle time. For this reason the companies have to investigate their production systems and improve their processes. In order to see the effects of the improvements on a real system, simulation tool is mostly used.

In this study simulation is used as an optimization tool. Simulation is used to understand character of real systems. There are many simulation applications in shipbuilding, as described in the literature. In a common study realized by Michigan University and Seoul National University, the whole processes of a shipyard are attempted to be modeled with simulation and the effects of some changes on the system are perceived [2]. In the study of Okumoto *et al*. [3], performed by modeling the scaffold placement with three-dimensional simulation CAD system, the effects of the changes on the system have been observed. Shin [4] has modelled the workstations of the sub-assembly line with the use of simulation and determined the effect of placing a welding robot on productivity. In the other study of Shin [5] an optimum shipbuilding layout has been found by using simulation. Alfeld *et al.* [6] has used a special software in simulating the shipyard processes to ensure that the planners take decisions easily. Alkaner [7] has simulated the processes of the profile cutting station and by making some changes in resources, the effects of these changes have been investigated. Doing some alterations on panel production station, Greenwood *et al.* [8] has investigated the effects of the changes on the production system**.** Lee *et al.* [9] has found the effects of the intelligent welding robot system on welding performance. Cha and Roh [10] have developed a simulation framework and applied it to block erection process. As can be concluded, there are many application fields of simulation in shipyard industry.

In this study the processes of the panel line of a shipyard located in Turkey have been considered. Firstly, the detailed process analysis of the panel line has been performed. In this way the whole work activities of the panel line and their durations have been found. In the second stage of the study the simulation model of the panel line has been elaborated by using ARENA 11.0 software. The required data achieved from the process analysis have been put in the simulation model. Then the model has been run for 10-day period and number of products manufactured by the panel line has been determined. In the third stage of the study an alteration in section spot welding station has been made. And, this alteration has been put in the simulation model and the model has been run again for 10- day period. Then the effect of this alteration on the system throughput has been determined.

As mentioned above, the alteration made in the panel line is interesting in the case of section spot welding station. In the section spot welding station of the panel line, minor and sub- assemblies are mounted on the flat panel assembly and their matrix structure is formed. In many shipyards in Turkey, minor and sub-assemblies are welded one by one on flat panel assembly in order to produce matrix structure. In this way it takes a longer time to manufacture the matrix structure and a bottleneck situation may occur on the panel line. Instead of

the mounting of minor and sub-assemblies one by one, they should be mounted on flat panel assembly as a module. In other words, the matrix structure can be mounted as a module. It is believed that mounting the matrix structure as a module reduces the production cycle time and increases the throughput of the panel line.

## METHODOLOGY

In this study, the steps presented in Fig 1 are followed, respectively. At the beginning the workstations forming the panel line are determined and defined (Step 1). Then the product to be manufactured in the panel line and its sub-compenents are defined (Step 2). After the process analysis of the workstations is performed, the panel line is modelled by using simulation (Model 1), (Step 4) and the model is run for a specified duration time (Step 5). In Step 6, work flow in the section spot welding is changed and module mounting is carried out instead of mounting the minor and sub-assemblies one by one on the flat panel assembly (Stage F). In Step 7, the panel line is modelled by using simulation again and consequently Model 2 is achieved. In Model 2, the workstations' work flows remain constant except for the section spot welding. In Step 8, Model 2 is run for the same time period as in the case of Model 1 and throughput quantity of the panel line is achieved. At the last step (Step 9), Model 1 and Model 2 are compared mutually in terms of throughput quantity.

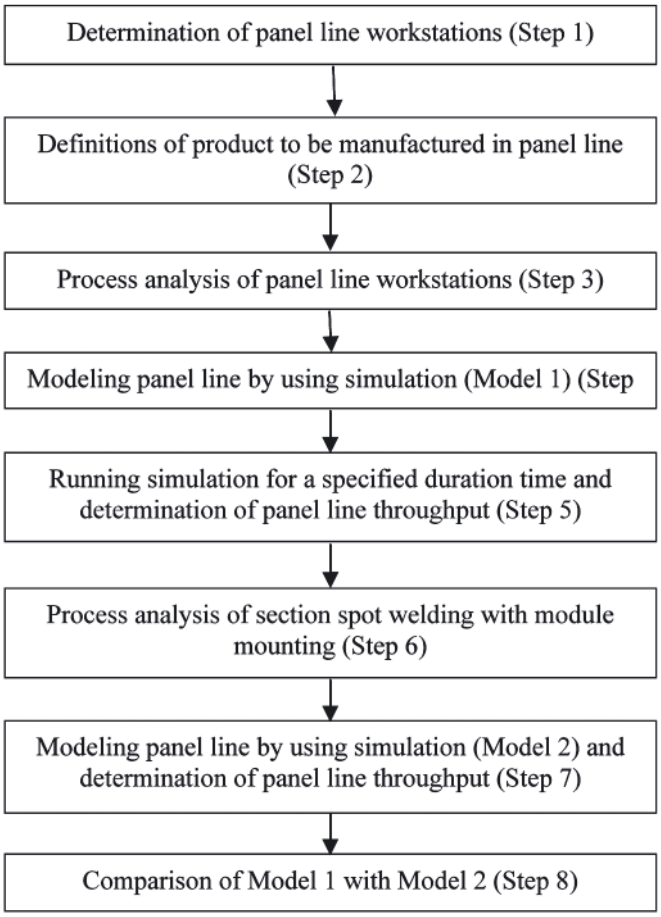


***Fig. 1.*** *Methodology of the study*

### *Determination of panel line workstations (Step 1)*

The panel line is a production cell where flat structures are fabricated. It consists of different types of workstations. There are 9 workstations on the panel line. Each workstation has a function in the production process. Tab. 1 shows the workstations located on the panel line.

***Tab. 1.*** *Workstations on the panel line*

| No. of workstation | Workstation name |
|---|---|
| I1 | Edge cutting station |
| I2 | Edge cleaning and sequencing |
| I3 | Panel production |
| I4 | Panel cutting |
| I5 | Profile spot welding |
| I6 | Profile tig welding |
| I7 | Section spot welding |
| I8 | Section tig welding |
| I9 | Grinding |

The edge cutting operations of the plates are performed in the edge cutting station (I1). The cutting operation is carried out by using plasma. The plates being cut are then sent to the edge cleaning and sequencing station (I2) where the edge cleaning operation of the cut surfaces is performed. Grinding machines are used in this operation. The sequencing operation is also carried out in this station in order to sequence the plates which enter the panel production machine. The plates are then sent to the panel production station from the edge cutting and sequencing station. In the panel production station (I3), the plates are mounted by using submerged arc welding. As an output of this station a panel is produced and then it goes to the panel cutting station where inside and outside cutting operations of the panel are performed. In the panel cutting station (I4), marking operation is also done. The cut and marked panel is sent to the profile spot welding station (I5). Here, the profiles are mounted on the flat panel and a flat panel assembly is produced as an output. a spot welding machine is used for this operation. The flat panel assembly is then sent to the profile tig welding station (I6) in order to complete the welding operations. After completion of the welding operation of the flat panel assembly it goes to the section spot welding station (I7) where minor assemblies and sub - assemblies are mounted on the flat panel assembly by using spot welding. As an output, a major sub-assembly is manufactured in this station. The major sub-assembly is sent to the section tig welding station (I8) from the section spot welding station in order to complete the welding operation. Finally, the major sub-assembly arrives at the grinding station, the last workstation of the panel line (I9). In this station the grinding operations of the welded places of the major sub-assembly are carried out. After completion of the grinding operations it leaves the panel line. Fig. 2 shows the material flow on the panel line.

### *Definitions of products to be manufactured in panel line (Step 2)*

In the panel line interim products which have flat structure are produced. For a double bottom block, flat panel assembly and major sub-assembly are fabricated in the panel line. In this study, a major sub-assembly was considered as a product.

In ship production some codes, each representing a production stage of blocks, are used. Such coding system is very useful to seperate and check the production stages orderly. Tab. 2 shows the production stages and their definition.

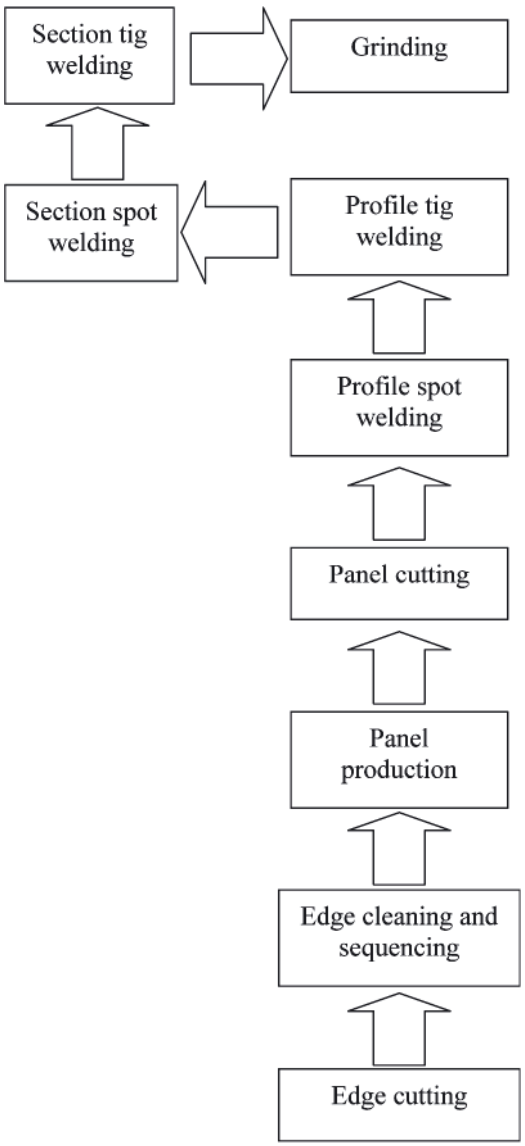


***Fig. 2.*** *Work flow through the panel line*

The major sub-assembly (Stage G) is regarded as a throughput of the panel line in question and it includes structures of various types, such as single section parts (Stage A), single plate parts (Stage B), minor assemblies (Stage C), sub-assemblies (Stage D), flat plate assembly (Stage E), and flat panel assembly (Stage F), as defined in Tab. 2.

The single section parts and single plate parts which have specified dimensions are described as a and B production stages, respectively. a single profile is defined as a production stage and a single plate is defined as B production stage.

If one single section part and one single plate part are assembled together, the minor assembly (C) is manufactured. If two or more minor assemblies are fitted together the sub-assembly (D) is built.

The flat plates constitute flat panel structures. If two or more flat plates are fitted together they form the flat plate assembly (E). If single section parts (A) are fitted onto the panel, the panel with profiles, called the flat plane assembly (F), is formed.

Minor and sub-assemblies (C and D production stages) are fitted onto the flat panel assembly (F) to form finally the major sub-assembly (G).

As above mentioned, the major sub-assembly includes various types of production stages. Fig. 3 shows the product breakdown structure of the major sub-assembly considered in this study.

***Tab. 2.*** *Production stages and definitions*

| Production Stage | Definitions of production stages | Structures representing production stage |
|---|---|---|
| A | Single section part |  |
| B | Single plate part |  |
| C | Minor assembly |  |
| D | Sub assembly | 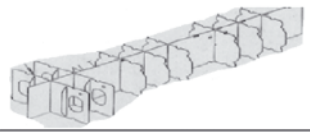 |
| E | Flat plate assembly | 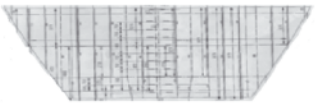 |
| F | Flat panel assembly | 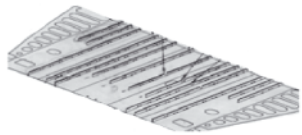 |
| G | Major sub assembly | 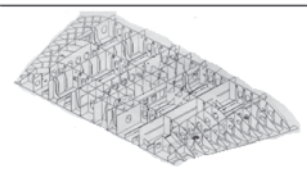 |

In the major sub-assembly production process some mounting operations take place. In the first stage a set of single section parts of 7 in number are welded together and the flat plate assembly is formed. In the second stage the flat plate assembly and a set of single section parts of 18 in number are welded together and the flat panel assembly is produced. In the third stage, the flat plate assembly, a set of minor assemblies of 14 in number and a set of sub- assemblies of 9 in number are mounted together to form the major sub-assembly being a throughput of the panel line.

## *Process analysis of panel line workstations (Step 3)*

So far, the panel line and the structure of major sub-assembly as an output are briefly discussed. In this section a detailed process analysis of the panel line production system has been performed. During the process analysis each of work stations in the panel line has been considered in detail.

The main point of the process analysis is to determine the work activities. After determining work activities their operation times are calculated. Then, by considering the parallel and serial work activities, the completion times of work stations are determined. It is impossible to present here all the work activites in panel line. For this reason the process analyses of the profile spot welding (I5) and profile tig welding (I6) stations, are only exemplified in Tab. 3 and 4.

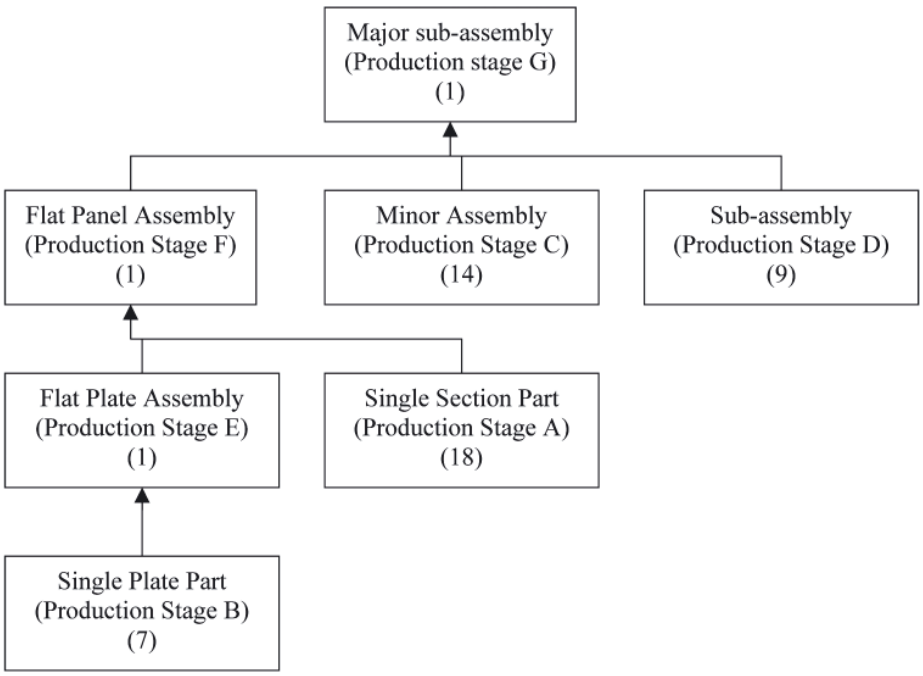


***Fig. 3.*** *Product breakdown structure of major sub-assembly*

***Tab. 3.*** *The process analysis of the profile spot welding station (I5)*

| No. of activity | Activity description | Activity duration time [min] |
|---|---|---|
| 1 | The operator walks to the crane | 0.146 |
| 2 | The operator runs the crane | 0.166 |
| 3 | The crane goes to profile stock area | 8.178 |
| 4 | The operator assistants go to profile stock area | 3.493 |
| 5 | The crane comes down the profile | 18.051 |
| 6 | The crane holds the profile | 15.2 |
| 7 | The crane lifts the profile | 18.037 |
| 8 | The crane transports the profile from profile stock area to the porter system | 8.473 |
| 9 | The workers walk to the porter system | 3.609 |
| 10 | The crane puts down the profile onto the porter system | 12.274 |
| 11 | The crane leaves the profile operation area | 4.428 |
| 12 | The workers settle the profile on the porter system | 3.8 |
| 13 | The operator walks to the proter system | 0.118 |
| 14 | The workers walk to the profile welding area | 0.404 |
| 15 | The operator runs the porter system | 0.166 |
| 16 | The operator drives the porter system to the welding area | 2.926 |
| 17 | The operator walks to profile spot welding machine | 0.042 |
| 18 | The operator cleans the welding torch | 1.5 |
| 19 | The operator runs the profile spot welding machine | 0.5 |
| 20 | The profile spot welding machine goes to the porter system | 44.755 |
| 21 | The profile spot welding machine comes down the profiles | 3.8 |
| 22 | The profile spot welding machine transports the profile from the porter system to the flat plate assembly | 46.486 |
| 23 | The profile spot welding machine comes down the profile onto the flat plate assembly and alignment is performed | 111.394 |
| 24 | The profile spot welding is prepared for welding operation. | 6.328 |
| 25 | The process of spot welding | 63.82 |
| 26 | The conveyor system transports the flat plane assembly | 1.9 |
| | Total activity duration time | 380 |

*Tab. 4. The process analysis of the profile tig welding station (I6)*

| No. of activity | Activity description | Activity duration time [min] |
|---|---|---|
| 1 | The conveyor transports the flat panel assembly to the tig welding station | 0.574 |
| 2 | The operator removes the slag from the welding torch | 38 |
| 3 | The operator checks out the welding system and its connections | 38 |
| 4 | The operator drives the tig welding machine to the starting point of welding | 11.577 |
| 5 | The operator takes down the welding torches on the welding area | 17.1 |
| 6 | The process of tig welding | 301.071 |
| 7 | The operator takes up the welding torches | 3.154 |
| 8 | The conveyor transports the flat panel assembly to the buffer area | 4.134 |
| | Total activity duration time | 413.61 |

*Tab. 5. Completion times of the workstations of the panel line (Model 1)*

| No. of station | Station name | Number of work activities | Station completion time [min] |
|---|---|---|---|
| 1 | Edge cutting station | 218 | TRIA(111.5,144.9,200.8) |
| 2 | Edge cleaning and sequencing | 167 | TRIA(119.2,154.9,214.6) |
| 3 | Panel production | 327 | TRIA(368.2,478.6,491.5) |
| 4 | Panel cutting | 15 | TRIA(226.1,295.5,409.1) |
| 5 | Profile spot welding | 298 | TRIA(174.05,227.5,233.3) |
| 6 | Profile tig welding | 110 | TRIA(212.7,279.3,386.7) |
| 7 | Section spot welding | 781 | TRIA(501,656.3,911.8) |
| 8 | Section tig welding | 160 | TRIA(278,361.4,506) |
| 9 | Grinding | 148 | TRIA(85,111.3,154.7) |

Tab. 3 illustrates the work activities of the profile spot welding station. As can be seen from Tab. 3, there are 298 work activities to be perform in the profile spot welding station and its total activity time amounts to 380 min; whereas the station completion time is only 227.5 min because some of the activities are parallel. That is why the total activity time and the station completion time are not same. Tab. 4 represents the work activities of the profile tig welding station. In this case 110 work activities are performed during the total activity time of 413.61 min; whereas the station completion time amounts to 279.3 min.

In the same way the process analysis of other workstations of the panel line are performed and the station completion times are achieved, as shown in Tab. 5.

It should be noted that the station completion times calculated from a comprehensive process analysis are regarded as optimistic ones. Because their distribution is assumed triangular, expected and pessimistic times are also needed to be assigned. In this study the optimistic and pessimistic times are assigned from gained experience.

## *Modeling panel line by using simulation (Model 1) (Step 4)*

In this step the ARENA 11.0 software has been used for modeling the panel line. The required data have been achieved from the process analysis (Step 3); on this basis, apart from station completion times, transportation duration times are achived. The duration times are calculated by considering the production system and they are thought to have triangular distribution. Tab. 6 shows the duration times of transportation between workstations.

*Tab. 6. Duration times of transportation between workstations*

| Between workstations | Transportation times [min ] |
|---|---|
| Arrival to I1 | TRIA(1.7,2.2,3) |
| I1→I2 | TRIA(1.4,1.8,2.5) |
| I2→I3 | TRIA(2.6,3.3,4.6) |
| I3→I4 | TRIA(0.7,0.9,1.2) |
| I4→I5 | TRIA(0.5,0.6,0.9) |
| I5→I6 | TRIA(1.2,1.5,2.1) |
| I6→I7 | TRIA(2.1,2.7,3.7) |
| I7→I8 | TRIA(1.2,1.5,2.1) |
| I8→I9 | TRIA(1.1,1.4,1.9) |

In the simulation model in question, machine failures are also taken into considerations to reflect the real environment, as shown in Tab. 7. These values are not calculated but estimated. Failure times are thought to have exponential distribution.

*Tab. 7. Failure times of workstations*

| Station name | Up time [min] | Down time [min] |
|---|---|---|
| Edge cutting station | EXPO(120) | EXPO(10) |
| Edge cleaning and sequencing | EXPO(140) | EXPO(4) |
| Panel production | EXPO(180) | EXPO(15) |
| Panel cutting | EXPO(160) | EXPO(20) |
| Profile spot welding | EXPO(130) | EXPO(12) |
| Profile tig welding | EXPO(155) | EXPO(18) |
| Section spot welding | EXPO(165) | EXPO(5) |
| Section tig welding | EXPO(200) | EXPO(25) |
| Grinding | EXPO(160) | EXPO(8) |

In Figure 4, the simulation model of the panel line in question is presented.

Table 8 shows the module definitions of simulation model in Fig. 4.

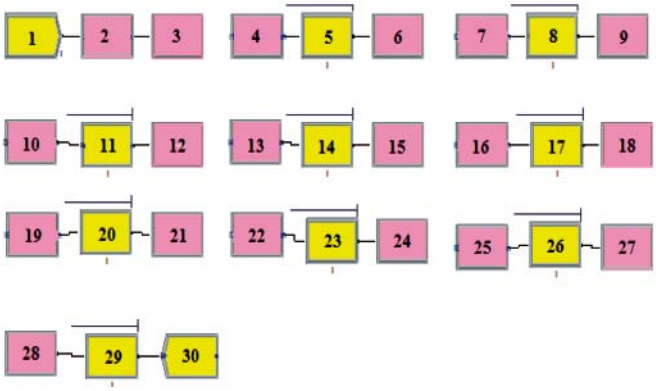


***Fig. 4.*** *Simulation model of the panel line*

***Tab. 8.*** *Module definitions*

| Module no | Module name | Module no | Module name |
|---|---|---|---|
| 1 | Part Arrival | 16 | I5 Arrival Station |
| 2 | Arrival Station | 17 | Profile Spot Welding |
| 3 | Route to I1 Station | 18 | Route to I6 Station |
| 4 | I1 Arrival Station | 19 | I6 Arrival Station |
| 5 | Edge Cutting | 20 | Profile Tig Welding |
| 6 | Route to I2 Station | 21 | Route to I7 Station |
| 7 | I2 Arrival Station | 22 | I7 Arrival Station |
| 8 | Edge Cleaning | 23 | Section Spot Welding |
| 9 | Route to I3 Station | 24 | Route to I8 Station |
| 10 | I3 Arrival Station | 25 | I8 Arrival Station |
| 11 | Panel Production | 26 | Section Tig Welding |
| 12 | Route to I4 Station | 27 | Route to I9 Station |
| 13 | I4 Arrival Station | 28 | I9 Arrival Station |
| 14 | Panel Cutting | 29 | Grinding |
| 15 | Route to I5 Station | 30 | End of Panel Line |

***Tab. 9.*** *The process analysis of the section spot welding station (I7) (Model 2)*

| No. of activity | Activity description | Activity duration time [min] |
|---|---|---|
| 1 | Transportation of matrix module structure to flat panel assembly | 15 |
| 2 | Alignment of matrix module structure on flat panel assembly | 45 |
| 3 | Horizontal spot welding and grinding operation after spot welding | 50.285 |
| 4 | Workers go to pick up single plate parts | 0.2 |
| 5 | Workers put down single plate parts | 0.2 |
| 6 | Workers do alignment of single plate parts | 1.666 |
| 7 | Horizontal spot welding of single plate parts | 2.826 |
| 8 | Vertical fixing of single plate parts | 1.666 |
| 9 | Vertical spot welding of single plate parts | 2.922 |
| 10 | Operating crane | 0.083 |
| 11 | Crane goes to single plate parts stock area | 8.853 |
| 12 | Crane comes down onto single plate part surface area. | 12 |
| 13 | Crane holds single plate parts | 6 |
| 14 | Crane lifts single plate parts | 12 |
| 15 | Crane transports single plate parts to flat panel assembly | 8.83 |
| 16 | Crane puts down the single plate parts for marking | 12 |
| 17 | Horizontal fixing of single plate parts | 4 |
| 18 | Crane leaves the surface area of single plate parts | 6 |
| 19 | Horizontal spot welding of single plate parts | 7.958 |
| 20 | Vertical fixing of single plate parts | 4 |
| 21 | Vertical spot welding of single plate parts | 9.586 |
| 22 | Operating grinding machine | 1 |
| 23 | Vertical and horizontal grinding after spot welding | 14.492 |
| 24 | Crane goes to pick up lifting lug | 1.216 |
| 25 | Crane comes down onto lifting lug's surface area | 2 |
| 26 | Crane holds lifting lug | 1 |
| 27 | Crane picks up lifting lug | 2 |
| 28 | Crane transports lifting lug to flat panel assembly | 1.222 |
| 29 | Crane puts down lifting lug on flat panel assembly | 2 |
| 30 | Fixing lifting lug on panel | 4 |
| 31 | Crane leaves lifting lug's surface area | 0.332 |
| 32 | Spot welding of lifting lugs | 9.332 |
| 33 | Crane departs from lifting lug | 2 |
| 34 | Cleaning | 30 |
| 35 | Transportation of major sub-assembly | 2.528 |
| | Total duration time | 284 |

### *Running simulation for a specified duration time and determination of panel line throughput (Step 5)*

The simulation model has been run for 10-day period under the assumption that the shipyard operates in two shifts. Each shift lasts 8 hours. Number of replication of the model is equal to 5. As a result of the running, the panel line has produced 11 major sub-assemblies.

### *Process analysis of section spot welding with application of module mounting (Step 6)*

When the matrix module structure is assembled on flat panel assembly, the completion time of the section spot welding station will obviously change by nature of the things. To see the effect of the changing on throughput, the new completion time of the section spot welding station should be put in the simulation model shown in Fig. 4. In the current panel line system in question the completion time of the section spot welding station is determined as shown in Tab. 5. Tab. 9 presents the work flow of the matrix module structure. When the matrix module structure is assembled on the flat panel assembly the completion time of the section spot welding station reaches 284 min.

### *Modeling panel line by using simulation (Model 2) and determination of panel line throughput (Step 7)*

In this step the simulation model shown in Fig. 4 is applied. All the completion duration times of the workstations remain constant except for the section spot welding station. By changing the completion time of the section spot welding station, Model 2 was obtained. The completion times of the work stations for Model 2 are shown in Tab. 10.

***Tab. 10.*** *Completion times of the workstations on the panel line (Model 2)*

| No. of station | Station name | Station completion time [ min ] |
|---|---|---|
| 1 | Edge cutting station | TRIA(111.5,144.9,200.8) |
| 2 | Edge cleaning and sequencing | TRIA(119.2,154.9,214.6) |
| 3 | Panel production | TRIA(368.2,478.6,491.5) |
| 4 | Panel cutting | TRIA(226.1,295.5,409.1) |
| 5 | Profile spot welding | TRIA(174.05,227.5,233.3) |
| 6 | Profile tig welding | TRIA(212.7,279.3,386.7) |
| 7 | Section spot welding | TRIA(284,367.4,516.9) |
| 8 | Section tig welding | TRIA(278,361.4,506) |
| 9 | Grinding | TRIA(85,111.3,154.7) |

The transportation and failure times given in Tab. 6 and 7 are also valid for Model 2. When the simulation model is run for 10- day period under the assumption of two shifts, the panel line has produced 16 major sub-assemblies.

### *Comparison of Model 1 with Model 2 (Step 9)*

Tab. 11 shows the comparison of Model 1 with Model 2. In both the models numbers of replication, replication lengths and working hours per day are the same, whereas the numbers of major sub-assemblies are different. This difference demonstrates the effect of the module mounting on the panel line throughput.

***Tab. 11.*** *Comparison of the two applied models*

| | Model 1 | Model 2 |
|---|---|---|
| **Number of replication** | 5 | 5 |
| **Replication length [days ]** | 10 | 10 |
| **Hour per day [ hours ]** | 16 | 16 |
| **Number of major sub- assemblies** | 11 | 16 |

## CONCLUSION

- In this study the simulation model has been created by determining the processes performed on the panel line. The required data achieved from the process analysis have been put in the model. The simulation model has been run for 10-day period and as a result the panel line has produced 11 major sub-assemblies. In the next step, it was assumed that the matrix module structure is assembled on flat panel assembly. In this case, the completion time of section spot welding has changed from 501 min to 281 min. When the simulation model has been run in this case, the panel line has produced 16 major sub assemblies. This way the panel line produces 5 blocks more during 10 days, that means that its productivity increased by 45%.
- Therefore the application of assembling matrix module structure increases the panel line productivity by 45%. This is a good result in terms of shortening the ship production cycle.

**BIBILOGRAPHY**


1. Rashwan, A.M., and Naguib, A.:*Toward improving the cost competitive position for shipbuilding yards, Part I: Impact of technology changes*. Alexandria Engineering Journal, Vol.45 (2006), No.5, pp.537-543.
2. Lamb, T.: *Simulation-based performance improvement for shipbuilding processes*. Journal of Ship Production, Vol. 22 (2006), No. 2, pp.49-65.
3. Okumoto, Y., Hiyoku, K., and Uesug, N.: *Simulation-based ship production using three-dimensional CAD*. Journal of Ship Production, Vol.22 (2006), No.3, pp.155-159.
4. Shin, J.G. : *a modeling and simulation of production process in subassembly lines at a shipyard.* Journal of Ship Production, vol.20 (2004), No.2, pp. 79-83.
5. Shin, J.G.: *a concept and framework for a shipyard layout design based on simulation.* Journal of Ship Production, Vol.25 (2009), No.3, pp.126-135.
6. Alfeld, L.E., Pilliod, C.S., and Wilkins, J.R.: *The virtual shipyard: a simulation model of the shipbuilding process.* Journal of Ship Production, Vol.14 (1998), No.1, pp.33-40.
7. Alkaner, S. : *The modeling and analysis of ship production with simulation: Case Study*. PhD Thesis, ITU Institute of Science, Istanbul, 1998
8. Greenwood A.G., Hill, H.W.: *Simulation optimization decision support system for ship panel shop operations*. Proceedings of the 2005 Winter Simulation Conference, pp. 2078-2086.
9. Lee,D. *et al.* : *Development and application of an intelligent welding robot system for shipbuilding.* Robotics & Computer-Integrated Manufacturing, vol. 27 (2011)., No. 2, pp. 377-388.
10. Cha, J.H., and Roh, M.I.: *Combined discrete event and discrete time simulation framework and its application to the block erection process in shipbuilding.* Advances in Engineering Software, vol. 41(2010), No. 4, pp. 656-665.


**CONTACT WITH THE AUTHOR**


Murat Ozkok, Ph.D.
Department of Naval Architecture and Marine Engineering,
Karadeniz Technical University,
61530 Camburnu/Trabzon, TURKEY,
e-mail: muratozkok@ktu.edu.tr
phone: +90 462 752 2805, fax: +90 462 752 2158


The Ship Handling Research and Training Centre at Ilawa is owned by the Foundation for Safety of Navigation and Environment Protection, which is a joint venture between the Gdynia Maritime University, the Gdansk University of Technology and the City of Ilawa.

**Two main fields of activity of the Foundation are:**

- Training on ship handling. Since 1980 more than 2500 ship masters and pilots from 35 countries were trained at Iława Centre. The Foundation for Safety of Navigation and Environment Protection, being non-profit organisation is reinvesting all spare funds in new facilities and each year to the existing facilities new models and new training areas were added. Existing training models each year are also modernised, that's why at present the Centre represents a modern facility perfectly capable to perform training on ship handling of shipmasters, pilots and tug masters.

- Research on ship's manoeuvrability. Many experimental and theoretical research programmes covering different problems of manoeuvrability (including human effect, harbour and waterway design) are successfully realised at the Centre.

The Foundation possesses ISO 9001 quality certificate.

**Why training on ship handling?**

The safe handling of ships depends on many factors - on ship's manoeuvring characteristics, human factor (operator experience and skill, his behaviour in stressed situation, etc.), actual environmental conditions, and degree of water area restriction.

Results of analysis of CRG (collisions, rammings and groundings) casualties show that in one third of all the human error is involved, and the same amount of CRG casualties is attributed to the poor controllability of ships. Training on ship handling is largely recommended by IMO as one of the most effective method for improving the safety at sea. The goal of the above training is to gain theoretical and practical knowledge on ship handling in a wide number of different situations met in practice at sea.

For further information please contact:
**The Foundation for Safety of Navigation and Environment Protection**

Head office:
36, Chrzanowskiego Street
80-278 GDAŃSK, POLAND
tel./fax: +48 (0) 58 341 59 19

Ship Handling Centre:
14-200 IŁAWA-KAMIONKA, POLAND
tel./fax: +48 (0) 89 648 74 90
e-mail: office@ilawashiphandling.com.pl
e-mail: office@portilawa.com